ADVERTIMENT. La consulta d’aquesta tesi queda condicionada a l’acceptació de les següents condicions d'ús: La difusió d’aquesta tesi per mitjà del servei TDX (www.tesisenxarxa.net) ha estat autoritzada pels titulars dels drets de propietat intel·lectual únicament per a usos privats emmarcats en activitats d’investigació i docència. No s’autoritza la seva reproducció amb finalitats de lucre ni la seva difusió i posada a disposició des d’un lloc aliè al servei TDX. No s’autoritza la presentació del seu contingut en una finestra o marc aliè a TDX (framing). Aquesta reserva de drets afecta tant al resum de presentació de la tesi com als seus continguts. En la utilització o cita de parts de la tesi és obligat indicar el nom de la persona autora.

ADVERTENCIA. La consulta de esta tesis queda condicionada a la aceptación de las siguientes condiciones de uso: La difusión de esta tesis por medio del servicio TDR (www.tesisenred.net) ha sido autorizada por los titulares de los derechos de propiedad intelectual únicamente para usos privados enmarcados en actividades de investigación y docencia. No se autoriza su reproducción con finalidades de lucro ni su difusión y puesta a disposición desde un sitio ajeno al servicio TDR. No se autoriza la presentación de su contenido en una ventana o marco ajeno a TDR (framing). Esta reserva de derechos afecta tanto al resumen de presentación de la tesis como a sus contenidos. En la utilización o cita de partes de la tesis es obligado indicar el nombre de la persona autora.

WARNING. On having consulted this thesis you’re accepting the following use conditions: Spreading this thesis by the TDX (www.tesisenxarxa.net) service has been authorized by the titular of the intellectual property rights only for private uses placed in investigation and teaching activities. Reproduction with lucrative aims is not authorized neither its spreading and availability from a site foreign to the TDX service. Introducing its content in a window or frame foreign to the TDX service is not authorized (framing). This rights affect to the presentation summary of the thesis as well as to its contents. In the using or citation of parts of the thesis it’s obliged to indicate the name of the author

Bubble and droplet flow phenomena at different gravity levels

by

FRANCESC SUÑOL

ACTA DE QUALIFICAIÓ DE LA TESI DOCTORAL

Reunit el tribunal integrat pels sota signants per jutjar la tesi doctoral:

Títol de la tesi: ....

Autor de la tesi: ....

Acorda atorgar la qualificació de:

☐ No apte
☐ Aprovat
☐ Notable
☐ Excel·lent
☐ Excel·lent Cum Laude

Barcelona, ... de/d' .... de ....

El President

....
(nom i cognoms)

El Sectretari

....
(nom i cognoms)

El Vocal

....
(nom i cognoms)

El Vocal

....
(nom i cognoms)

El Vocal

....
(nom i cognoms)

Bubble and droplet flow phenomena at different gravity levels

by

FRANCESC SUÑOL

A Thesis Submitted to
UNIVERSITAT POLITÈCNICA DE CATALUNYA
in Partial Fulfillment of the
Requirements for the Degree of
Doctor of Philosophy
in Physics

Thesis Supervisor:
RICARD GONZÁLEZ-CINCA

Computational and Applied Physics Program
DEPARTAMENT DE FÍSICA APLICADA

Barcelona, 2011

Copyright © 2011 by F. Suñol.
All Rights Reserved.

To my family

Abstract

Two-phase flows are encountered in a wide range of applications both on-ground and in space. The dynamics of such flows in the absence of gravity is completely different from that in normal gravity due to the absence of buoyancy forces. A deeper understanding of the behavior of multiphase flows is essential in order to improve the operation of devices which require the use of two-phase systems. Analytical and experimental work is still needed for enhancing the control of two-phase flows, due to the theoretical complexity and the lack of experimental data for certain configurations.

In this work, the behavior of two-phase flows has been studied experimentally in normal gravity and in microgravity conditions. In particular, the single-jet configuration has been investigated for bubbly jets and droplet jets. Dynamics of individual bubbles and droplets as well as the global structure of the jets has been considered. The opposed-jet configuration has been investigated for bubbly flows. Different separation between jets and orientation angles have been studied in normal gravity, and the obtained results have been compared to the microgravity case. A numerical model has been implemented to study single-phase jet impingement and opposed bubbly jets at different gravity levels. Good qualitative agreement between the simulations and the experiments has been obtained. The bubble bouncing process, prior to coalescence, after collision with a flat free surface has been also studied experimentally in normal gravity conditions.

The results presented in this work will help to improve the general understanding of two-phase flows in normal gravity and in microgravity conditions, with general applications on mixing devices, environmental and propulsion systems.

Acknowledgements

I am deeply grateful to my supervisor, Dr. Ricard González-Cinca, whose kind assistance and encouragement have guided me throughout the duration of this research. He has shown a huge interest in this work, being his patience and perseverance essential to push me forward whenever needed.

I would like to thank all of my committee members, Dr. Thodoris Karapantsios, Dr. Dominique Legendre, Dr. Mauricio Hoyos, Dr. Laureano Ramírez and Dra. Ana Lacasta for their useful suggestions and feedback.

I wish to express my sincerest gratitude to Dr. Jaume Casademunt for introducing me to the microgravity research group at UPC, and for sharing his knowledge and motivation.

My appreciation is extended to the people at ICMCB in Bordeaux. Special thanks go to Dr. Yves Garrabos and Carole Lecoutre for letting me participate to the 52nd ESA's Parabolic Flight Campaign, to Dr. Jalil Ouazzani for his kind help with the Phoenics™ software and all the people from the supercritical fluids group at ICMCB for their warm welcome and for making my short-term visit at ICMCB a great experience.

I would like to thank the ESA Education office for giving me the opportunity to participate to the 9th Student Parabolic Flight Campaign, to the 2nd Drop Your Thesis Campaign, and many international conferences. Thanks to Ángel Carretero from INTA and Jordi Carrera for the shared experiences in the INTA Drop Tower. I want to express my gratitude to the people from the ZARM Drop Tower in Bremen, specially to Dr. Thorben Könemann, Dieter Bischoff and Simon Mawn for their helpful assistance with the experimental setup assembly.

I am exceptionally grateful to the people at the Microgravity Laboratory at UPC, Santiago Arias and Oscar Maldonado, for their unconditional help in the experimental setup design, and for all the unforgettable moments we have lived throughout these years. I also would like to thank all the people who have shared office with me: Araceli, Estel, Isa, Jazmin, Juan Carlos, Marc, Milad, Roger and Victor, for their kind company in the everyday life.

Special thanks go to my friend Jaume Roqueta. Without his personal influence, this thesis would have never been written.

All my thanks to those who helped, encouraged and supported me during these past years and whose names are not mentioned here, to all my friends and relatives.

I cannot finish without expressing my deep gratitude to my family. I am forever indebted to my father Jaume, my mother Eva and my brother Jaume for their endless patience, continuous support and for encouraging me to do my best in all matters of life. This thesis is dedicated to them.

Financial support from *Comissionat per a Universitats i Recerca del Departament d'Innovació, Universitats i Empresa de la Generalitat de Catalunya i del Fons Social Europeu* under a predoctoral FI grant is gratefully acknowledged.

Francesc Suñol
Barcelona, February 2011

Contents

List of Figures

List of Tables

List of Symbols

Greek Symbols

δ	Perturbation amplitude
ℓ	Injection direction
ϵ	Aspect ratio
Γ	Phase diffusion coefficient
γ	Surface tension
μ	Dynamic viscosity
ν	Kinematic viscosity
ω	Oscillation frequency
ϕ	Dummy variable
Ψ	Conical angle of the jet
ψ	Stream function
ρ	Density
σ	Source
ε	Turbulent dissipation per unit mass
φ	Injection angle
ϑ	Delimitation angle
ζ	Radial distance from injection axis

Roman Symbols

A	Area
b	Impact parameter
d	Diameter
f	Force (Appendix B)
f	Frequency (Chapters 3 and 5)
f	Volume fraction (Chapter 4)

g	Gravity acceleration
i, j, k	Indices
J	Momentum flux
k	Turbulent kinetic energy per unit mass (Chapter 4)
k	Wavenumber (Chapter 3)
L	Length
m	Mass
p	Pressure
Q	Flow rate
q	Modal frequency
s	Separation between jets
S_{ij}	Rate-of-strain tensor
t	Time
V	Volume
v	Velocity
x, y, z	Cartesian coordinates

Subscripts

0	Initial
a	Air
add	Added mass
B	Bubble
b	Bouncing (Chapter 5)
b	Breakup (Chapter 3)
C	Capillary
c	Critical
col	Collision
D	Drag
d	Destabilization
e	Equivalent
ext	External
G	Gas
g	Generation
h	Horizontal direction
L	Laminar (Chapters 4.2 and 4.3)
L	Liquid

m	Measured
max	Maximum
R	Rise
r	Radial direction
s	Steady
T	Turbulent
v	Vertical direction
x	Coordinate direction (horizontal)
y	Coordinate direction (vertical, gravity direction)

Dimensionless numbers

Bo	Bond number	$\mathrm{Bo} = \dfrac{\Delta \rho g d^2}{\gamma}$
Ca	Capillary number	$\mathrm{Ca} = \dfrac{\mu v}{\gamma}$
Fr	Froude number	$\mathrm{Fr} = \dfrac{v}{\sqrt{gd}}$
Oh	Ohnesorge number	$\mathrm{Oh} = \dfrac{\mu}{\sqrt{\rho \gamma d}}$
Re	Reynolds number	$\mathrm{Re} = \dfrac{vd}{\nu}$
We	Weber number	$\mathrm{We} = \dfrac{\rho v^2 d}{\gamma}$

List of Acronyms

ECLSS Environmental Control and Life Support Systems

ESA European Space Agency

ESTEC European Space Research and Technology Center

EVA Ethilen-Vinil Acetate

ICMCB *Institut de Chimie de la matière condensée de Bordeaux*

INTA *Instituto Nacional de Técnica Aeroespacial*

IPSA Inter-Phase Slip Algorithm

ISS International Space Station

LDC Large Diameter Centrifuge

UPC *Universitat Politècnica de Catalunya*

ZARM *Zentrum für Angewandte Raumfahrttechnologie und Mikrogravitation*

CHAPTER 1

Introduction

Jets are collimated streams of matter adopting approximately a conical shape. Jets occur in an extremely large variety of situations, spanning a broad range of physical length scales, from the microscale up to the large-scale structure of the universe.

The term “two-phase flow” is used to refer to any fluid flow consisting of two phases or components. In this work, the term two-phase flow refers to gas-liquid flows solely, covering the topics addressed in this thesis such as slug flow (Chapter 2), droplet flow (Chapter 3) or bubbly flow (Chapters 3 and 4). A slug flow is an intermittent flow of gas bubbles which occupy most of the pipe cross-sectional area, separated by slugs of continuous liquid-phase. Bubbly flows refer to the situation in which the gas-phase is somewhat uniformly distributed in the form of bubbles in a carrier liquid-phase. In a complementary fashion, a droplet flow corresponds to uniformly distributed liquid droplets in a continuous gas-phase.

Two-phase flows can be divided into two general categories, determined by their topology [Bre05, bCTC05]: “Dispersed flows” and “Separated flows”. Dispersed flows consist of a number of finite-sized drops or bubbles distributed in a connected volume of continuous phase (bubbly flows, droplet flows). Separated flows are identified by two or more continuous streams of different fluids separated by interfaces (slug flows).

Numerous industrial and energy conversion processes rely on the flow of two-phase mixtures. For this reason, the number of technological applications using two-phase flows is extremely large. In the next sections, only a few of them will be pointed out.

1.1 Motivation

1.1.1 Two-phase flows

Two-phase flows are encountered in numerous situations. They are present in our everyday environment (cosmetics, food, medical diagnosis, etc.) and they also occur in various exciting natural phenomena (rainstorms, volcano lava, cavitation, etc.). Numerous applications make the use of gas-liquid systems a crucial point for their proper operation. For example, some industries that currently require the use of two-phase flows are: the aerospace industry, process industry, nuclear industry, oil industry, metallurgical industry, biological, pharmaceutical and medical industry. More explicit applications are the heat-exchangers, cleaning devices, propulsion systems, energy transport and conversion systems, oxygenation, diesel engines, refrigeration, mixing devices and environmental systems [Kle03, Bre05, bCTC05, CGW05, IH06].

In all the cited technologies, the ability to predict the fluid flow of these systems is essential in order to improve the control and efficiency of those applications. However, the complete understanding of the two-phase flow phenomena is still far from complete. On one hand, this is due to the lack of valuable experimental data that needs to be collected for different flow orientations and geometries. Much experimental data has been collected on-ground, but in the absence of gravity, only certain specific problems have been addressed. One other hand, from an analytical perspective, several theories and correlations were developed to predict the engineering parameters of two-phase systems for certain flow geometries, phase transitions, etc. [Gab07, SB05]. Nevertheless, due to the complexity of two-phase flows, such predictions were largely in terms of empirical correlations, which were for the most part based on specific test conditions. Extrapolation of these correlations to other conditions may not be valid, particularly when gravity is significantly reduced [Gab07].

1.1.2 Two-phase flows in microgravity

Under normal gravity conditions, when there is a big density difference between the two phases, the buoyancy force usually governs the dynamics and the behavior of the two-phase system. Secondary forces which can be usually very small in terrestrial conditions, are expected to play an important role in microgravity. Thus, a reduced gravity environment provides excellent conditions to study the behavior of two-phase flows without the masking effects of gravity.

Most of the research on gas-liquid flows in microgravity have been focused on the study of flow patterns inside pipes and the transition between those patterns [CF95, LS99]. When gas and liquid are flowing through a pipe in reduced gravity conditions, three main patterns are observed [MCF98]: bubbly flow, slug flow and annular flow. The transition between the bubbly and the slug flow appears to result from a progressive increase in the bubble size leading to bubble coalescences, identified as the mechanism responsible for the transition. A mechanistic model for turbulence-induced coalescence of bubbles inside tubes is presented in Kamp et al. [KCCF01]. The transition between slug flow and annular flow is probably due to a liquid film instability, a very complex phenomenon difficult to implement in the models.

In addition, numerous boiling experiments have been performed [Mar03, ZMH05], and the subsequent bubble dynamics have been investigated [Str01]. Moreover, many attempts to study the complex process of bubble formation in microgravity conditions have been carried out [KKO94, MGM+03, CPG06].

A reduced gravity environment can only be achieved in orbiting spacecrafts or free-falling objects. In the next section, a short review of the current microgravity platforms available is presented.

1.1.2.1 Microgravity platforms

Probably the best place to conduct microgravity research is in an orbiting spacecraft, due to the long duration of reduced gravity (from days to months) and the quality of the gravity level (10^{-2} to 10^{-5} g_0 ($g_0 = 9.81$ m/s^2 is the acceleration due to gravity at the Earth's surface) for the Space Shuttle and 10^{-3} to 10^{-6} g_0 for the ISS[1]). Nevertheless, conducting research in space tends to be time consuming, complex, and expensive. Whenever possible, it is desirable to use ground-based facilities, which can provide good quality of reduced gravity during a reasonable amount of time. The available ground-based platforms are described in the next paragraphs.

Drop towers and Drop tubes can provide 10^{-2} to 10^{-6} g_0 from 2 up to 10 seconds approximately. Those facilities consist in high towers or tubes, which either are evacuated[2] ($p \approx 10$ Pa inside the tower/tube) or use some way of reducing the drag exerted by the surrounding gas on the experimental capsule by using a double capsule system[3]. In these platforms, the experimental capsule is dropped from the top, being therefore at free-fall conditions for some seconds. When the experiment capsule reaches the bottom of the tower/tube, the deceleration levels can reach up to $g \approx 50$ g_0. Drop towers differ from drop tubes in their ability to accommodate larger experimental setups and provide longer durations of microgravity (1.5 to 5 seconds for drop tubes, 2 to 10 seconds for drop towers).

Another alternative to obtain reduced gravity conditions is to use an aircraft following parabolic trajectories. The typical parabolic maneuver consists in pulling up the airplane at an angle of 45°. At this moment, the engine slows down until the airplane is descending at an angle of 45°. Then, the engine pulls up the airplane with the aim to reach a horizontal trajectory. The parabolic flights provide approximately

---

[1] International Space Station

[2] Solution adopted at the ZARM Drop Tower.

[3] Solution adopted at the INTA Drop Tower.

10^{-2} g_0 during 20 seconds for each parabola. However, 20 seconds of 1.8 g_0 are reached before and after each parabola. Usually, a parabolic flight consist in a series of 30 parabolas, summing up 600 seconds of reduced gravity.

Finally, the sounding Rockets are promising alternatives to orbital flights which provide 10^{-4} to 10^{-6} g_0 for a time interval of 4 to 15 min. The payload can be launched to altitudes ranging approximately 80 to 300 km.

Recently, numerous enterprises (Virgin Galactic, XCor, Armadillo Aerospace, RocketPlane) are offering the possibility to carry out microgravity experiments in commercial suborbital flights. These flights can reach altitudes of 100 km approximately with a microgravity duration of 3-4 minutes and a microgravity level of $g \approx 10^{-3} g_0$.

The experimental results presented in this work in reduced gravity conditions, were obtained in drop tower facilities. In particular, the droplet jets were investigated at the INTA[4] Drop Tower and the bubbly jets were studied at the ZARM[5] Drop Tower. The reason for choosing drop towers instead of any other ground-based platforms are based on the necessity of a good gravity level ($g < 10^{-3}$ g_0) for a reasonable amount of time, and the restrictions on the experimental setup size and power consumption.

Previous experiments carried out by our research group in parabolic flights with bubbly flows revealed the necessity of a higher quality of the gravity level. Since bubbles are highly sensitive to the gravity level and a quiescent environment is required, the level of gravity should be lower than 10^{-3} g_0. Additionally, the size of the tank in which the bubbles are investigated should be large enough to neglect the wall effects, and the power and data telemetry requirements offered by the sounding rockets were not appropriate for our experiments. In the experiments presented herein, the timescale needed for the jets in order to grow and collide with the opposed jet, is around 0.5 to 1 second depending on the flow rates used. Hence, the drop towers were definitely chosen as the most appropriate candidates for accommodating our experimental setup.

1.1.2.2 Two-phase flow applications in microgravity

Two-phase flow research at reduced gravity has increased considerably in the last decades, due to the emerging applications requiring the use of two-phase systems. Some of the most noticeable applications concern the design of launch propulsion systems [MFK+10], in-space propulsion technologies [MJP+10], space power and energy storage [LGH+10], or the design and maintenance of active thermal control systems [HKM+10]. There are several characteristics that make two-phase flow more desirable than single-phase flow for heat transfer purposes[Gab07]. First, the heat transfer coefficient using two-phase flows with phase change can be several

---

[4] *Instituto Nacional de Técnica Aeroespacial*

[5] *Zentrum für Angewandte Raumfahrttechnologie und Mikrogravitation*

orders of magnitude higher than that in single-phase flow. Secondly, a physically smaller system with lower weight can carry as much heat as a single-phase system with much larger size and weight. Thirdly, heat can be transferred to the fluid while maintaining a constant surface temperature. This is a highly desirable feature for some applications requiring the use of an isothermal environment.

Another important application of two-phase flows is in the design of Environmental Control and Life Support Systems (ECLSS) [HBC+10, KAL+10]: the environmental conditions inside a spacecraft have to be maintained at comfortable levels. The management of two-phase systems is imperative to have a better control of humidity, level of O_2, etc., given that biological activity increases the water vapor content within the atmosphere.

Cryogenic liquids are typically required for use as propellants and to cool certain types of equipments and sensors. However, when the liquid is in contact with a warm surface, a certain amount of vapor is generated. The prediction of vapor generation under those conditions is crucial for the proper operation of refrigeration processes.

Numerous advances in medical, biological and chemical research have been carried out in a microgravity environment using bio- and chemical reactors. In particular, cellular behavior [LMC93, FVN95, YDS+99, KEEE08], tumor interactions [MJG93, ITS+97], bone tissues [KS93, FVN97, HCT+09] and a large variety of chemical processes have been investigated.

Studies of two-phase systems in space are also of great interest to better understand the behavior of terrestrial flows, due to the possibility of investigating the dynamics of the flow with the presence of various forces, but without the masking effects of gravity.

Designers of spacecraft gas-liquid systems attempt to address two key issues: Will the system work? How reliable is the system? As such, they focus on theoretical predictions. However, additional measurements are required in order to develop fundamental models.

1.2 Background

1.2.1 Bubbly jets

The motion and interaction of gas bubbles in liquid flows have been extensively studied over many years, due to their fundamental importance in many multiphase systems [Moo65, PB90, Che91, Orm97, Dui98, MCF98, KCCF01, CGW05, bCTC05]. In the last decades, bubble jets have been the subject of theoretical and experimental studies since many applications such as aeration control or mixing devices require the use of small bubbles with high area-volume ratio. Bubble plumes are produced by injecting gas in a liquid tank, while bubbly jets are produced by injecting gas-liquid mixtures in liquids. This has additional advantages over the single phase injection, such as the production of bubbles with a controlled size without the need of porous diffusers, low maintenance, and higher efficiency for gas transfer to the liquid phase [NZR08b].

The studies on bubbly jets aim to answer the natural questions: Which structure will the jet adopt? How the opening angle will behave? Which bubble size distribution will be present? Will the bubbles coalesce? If so, How frequently?

Schlichting [Sch79] studied the velocity field of single-phase laminar and turbulent jets, and the results obtained from these studies can be used as a basis for further investigations on bubbly jets, provided that the gas bubbles move passively following the liquid flow (as confirmed by Carrera et al. [CRRP+08]). The sizes of the bubbles present in bubbly jets depend on the fluid properties, gas and liquid flow rates, and the geometry of the injection system. Varely [Var95] investigated the bubble sizes in bubbly jets and found that bubble diameters decreases as the superficial liquid velocity increases, and the measured bubble size distributions were compared to normal, log-normal and gamma distributions. However, only size measurements were provided and no additional information such as bubble velocities or a study of the jet structure was described. An interesting investigation on the properties of bubbly jets injected in the vertical and horizontal directions has been carried out recently by Lima Neto et al. [NZR08a, NZR08b]. In their work, the bubble properties and the liquid flow structure have been detailed for a single bubbly jet injected in a stagnant water tank, but the size of the bubbles is much higher than those reported in the present work. Moreover, only on-ground results were presented, and no comparison with microgravity results was pointed out.

Knowledge of jet dynamics through geometries other than cylindrical tubes [MM01] or of the dynamics of a jet obtained after the interaction of two jets emerging from different angles, can give insight into the behavior of two-phase flows meeting at pipe junctions of space devices.

1.2.2 Droplet jets

Liquid jets are encountered in an extremely large variety of situations, from our everyday environment to highly sophisticated technological applications such as propulsion systems, manufacturing and agriculture, medical diagnosis or nuclear fission. The motivation for studying liquid jets is not only on the technological or industrial applications itself, but on the understanding of the complex physical properties that the jets may exhibit. For these applications or academic situations, the recurrent questions are: will the jet break? If so, how disperse in size will the fragments be? Will they collide? How frequently? Will the collision result in a bounce or in a coalescence event?

In the last decades, the evolution of high-speed photography and various laboratory techniques, as well as the evolution of computing processing power, have revived the subject both experimentally and theoretically.

From an experimental point of view, the recent innovations have made possible the detailed study of the breakup process and the structure of the resulting fragments. Hence, a rich source of information can be provided for comparison with theory.

On the analytical side, studies have been conducted to describe the transitions between the breakup mechanisms for liquid jets, dating back to the work of Lord Rayleigh [Ray78]. The most basic tool is the linear stability analysis around the cylindrical base state, although numerous researchers refined the linear analysis to include the effects of viscosity, outside fluid effects, nozzle geometry, etc. [OS06, EV08]. However, many non-linear effects are dominant in the breakup process and are extremely difficult to implement numerically.

The reader may refer to the work by Lin and Reitz [LR98] for a discussion of the various breakup regimes of liquid jets injected vertically on stagnant and co-flowing gases in normal gravity conditions.

On-ground, if the jet is not injected in the direction of gravity, it becomes distorted by the influence of gravity with the result being a liquid jet with a curved centerline. Thus, the axisymmetry is broken and the problem becomes complex to solve analytically. In this case, the interplay between the centerline of the jet and dynamics within the jet can affect the resulting instability and droplet formation. Recently, Uddin and Decent [UD10] performed a theoretical study on the instability of liquid jets curved by gravity, but no experimental data for comparison was reported.

In microgravity, Umemura et al. [UW02] and Tsukiji et al. [TUH04] studied the atomization regimes of a liquid jet emerging into a gas whose temperature and pressure exceeded the critical values of the injected liquid, identifying a new hydrodynamic-assisted capillary instability. However, the parameter range in their investigation is much different from that in the present work.

1.2.3 Impinging jets

The opposed-jet configuration has been used extensively for studying both laminar [VA92, AVP95, VAKF03] and turbulent properties of fluids [CL93, ECCJ00, AMS02, CCJM04, LSL+08]. The basis of this configuration is to bring two jets flowing along the same axis in opposite direction into a collision. As a result, a narrow zone (the impingement zone of high turbulence intensity) in which heat- and mass-transfer rates can be highly intensified, is created.

The enhancement of jet flow control is frequently desirable in many engineering systems, such as cleaning, aeration, mixing devices [WHY+91, YKB04] and liquid-liquid extraction processes [SZD06]. Many industrial applications require an improvement of fluid mixing efficiency, and some of them have to deal with a flexible control, according to operational conditions. As investigated by [TSSA06], such flexibility in the mixing process can be achieved by changing the impact angle between jets. A frontal collision between jets results in a high mixing efficiency, while increasing the impact angle, such efficiency becomes significantly diminished. The opposed-jet configuration with changeable orientation, using impinging bubble jets, becomes an attractive method for enhancing the mixing and aeration processes. An important advantage of this configuration is the direct control of operation, which maintains high efficiency and low cost of such systems.

The investigations on impinging jets usually aim to answer the following questions: What will the structure of the jets after collision be? What will the velocity field be? Will the configuration be stable? Where, and how frequently will the bubble coalescence events take place?

1.2.4 Bubble coalescence with a free surface

The collision between rising bubbles and a free surface is a common phenomenon in bubbly flows. Due to the extensive range of technological applications involving bubbly flows, there is a great demand from industries regarding the modeling of bubble physics. Bibliography on this subject has increased considerably in the last decades, but there are still some phenomena related to bubble dynamics, coalescence and interaction that are still poorly understood.

When a bubble rises in a liquid, the drag force compensates buoyancy resulting in a constant rise terminal velocity. If the bubble approaches the free surface with a velocity higher than a certain critical value, it bounces a few times before the coalescence occurs. At every bounce, a certain amount of energy of the bubble is lost in the interaction with the free surface, and the approach velocity of the bubble iwith respect to the free surface decreases to a critical value, at which coalescence occurs. In contrast, if the bubble is small enough to have a terminal velocity lower than a certain threshold, it coalesces with the free surface as soon as it touches the interface, and no bouncing takes place [SWF05].

Therefore, two main processes can be distinguished in the phenomenon of study. On one hand, there is a steady rise in which the bubble shape and dynamics do not change in time. On the other hand, there is a bouncing process in which the parameters characterizing the bubble dynamics change in time until the bubble coalesces with the free interface.

Within this context, the recurrent questions are: What are the parameters that dictate the bouncing, or direct coalescence regimes? What is the effect of bubble radius and velocity on this process?

Concerning the steady rise in a viscous liquid, most of the studies have been focused on the characterization of the bubble terminal rise velocity [Moo65, BD01, Rod01, dVBvW02, dVLL02, Tal07, SSSW08, Lot08] and the shape deformation caused by the motion of the bubbles [Lot08, WG02].

Regarding the dynamics of the bouncing process, the collision of bubbles and drops with solid walls has been extensively studied [TK97, KCM+01, KKM03, MKK05, LDG05, LZDG06, ZL09]. However, the collision of a bubble with a free surface is significantly different from that with a solid wall. The bouncing and coalescence processes of a bubble interacting with a free surface have also been studied by many authors [MKK05, KLM03, Gho04, ZKDM07]; however, no evidence of a bouncing threshold was reported. Recently, Sanada et al. [SWF05] studied the effects of viscosity on the coalescence of a bubble upon impact with a free surface, reporting that a critical threshold exists which separates the bouncing and non-bouncing processes of the interaction.

The coalescence of a bubble with a free surface is closely related to the coalescence of two bubbles or drops (for example, assuming that one of the bubbles/drops has an infinite radius), which has been studied by many authors over the years [KK93, Dui98, TETO05, RJM06, YBCL07, DL08]. However, this is a very complex phenomenon which has not yet been fully explained.

Motivated by the interesting phenomena which may occur when a bubble collides with a free surface, an on-ground experimental study has been carried out. Moreover, additional experiments are planned to be carried out in the near future at different gravity levels (hypergravity range, from 1 g_0 up to 20 g_0, where $g_0 = 9.81$ m/s^2) at the LDC[6] in ESTEC[7].

1.3 Objectives

The main general objective of this work is to gain more fundamental knowledge on two-phase flow dynamics, by obtaining experimental and numerical data in normal gravity and in microgravity conditions. In particular, this thesis aims to:

- Obtain experimental measurements on the structure of a bubbly jet in normal gravity and in microgravity conditions.
- Measure experimentally the global structure of a droplet jet, identify the transition between the dripping regime and the jetting regime, and analyze the size distribution and behavior of the individual droplets.
- Get experimental data on bubbly jet impingement on-ground and in reduced gravity conditions, studying the global structure of the jet and the properties of individual bubbles.
- Obtain numerical results on impinging jets and compare it qualitatively to the experimental results.

---

[6] Large Diameter Centrifuge

[7] European Space Research and Technology Center

- Get experimental measurements on-ground on the behavior of a bubble bouncing with a free surface, prior to coalescence.

1.4 Outline-organization

This thesis is organized in the following way:

The designs of the setups used in the ZARM's and INTA's drop towers, as well as the design for studying bubble coalescences with a free surface on-ground are described in Chapter 2.

In Chapter 3, the experimental results on single two-phase jets are presented. The results obtained in normal gravity and in microgravity conditions for bubbly jets and droplet jets are presented in Sections 3.1 and 3.2 respectively.

Chapter 4 concerns the impinging jets problem. It is divided in two main parts: The experimental results on bubbly jets on-ground and in reduced gravity conditions are presented in Section 4.1. Section 4.2 presents the numerical model used to study single-phase jet impingment, and the numerical results on bubbly jet impingement are presented in Section 4.3.

The experimental results on bubble coalescence upon impact with a free surface are presented in Chapter 5.

Finally, in Chapter 6, a summary of the main conclusions of this work is presented, the future work is explained and a number of recommendations are given.

In Appendix A, the analytical solutions for single-phase incompressible jet flows used in the present work are detailed.

In Appendix B, the governing equations and algorithms used for the numerical simulations are presented.

CHAPTER 2

Experimental setup

With the exception of the setup to study the bubble coalescence with a free surface[1], the rest of the experimental setups (both for droplets and bubbly jets) have been designed to be used in a drop tower, with the mass, power consumptions and volume restrictions that this implies. The main differences between the setups in normal gravity and in microgravity are the acquisition and control systems, which are operated by a wired computer in the first case, and a National Instruments' PXI via wireless in the second case. Additionally, the high-speed camera trigger is controlled manually in the first case, and is fully automatized in the second case. Moreover, different types of test tanks and injectors have been used in normal gravity and in microgravity. Each setup have been designed in a way that all of its components must resist high gravity levels, up to 50 g_0 (where $g_0 = 9.81$ m/s^2), which could be reached when the drop tower capsule is decelerating.

When designing the experimental setup for the study of two-phase flows in microgravity, numerous problems have been encountered. In particular, the bubble generation system and the method to avoid any overpressure without the use of any phase separator were challenging tasks. Although most of the problems have been solved, there are still some unexpected effects which should be improved in future experiments. For example, the presence of big bubbles in the collision zone of impinging bubbly jets in microgravity, or the division of a main liquid line into two sub-lines with equal flow rate are problems that still need improvement.

In this Chapter, a description of the used experimental setups is given and the solutions taken to avoid the possible problems are presented.

---

[1] The setup for study the bubble bouncing and coalescence with a free surface is designed to be used uniquely in normal gravity conditions, and is presented in Section 2.3.

Experiment	Bo	Fr	Oh
Bubbly jets 1g	$4.4 \cdot 10^{-3} - 1.4 \cdot 10^{-2}$	3.2 – 10.0	$3.7 \cdot 10^{-3}$
Bubbly jets 0g	$4.4 \cdot 10^{-3} - 4.1 \cdot 10^{-2}$	–	$3.7 \cdot 10^{-3}$
Droplet jets 1g	$1.5 \cdot 10^{-3} - 4.4 \cdot 10^{-3}$	2.6 – 7.8	$4.4 \cdot 10^{-3}$
Droplet jets 0g	$1.5 \cdot 10^{-3} - 4.4 \cdot 10^{-3}$	–	$4.4 \cdot 10^{-3}$
Impinging jets 1g	$2.1 \cdot 10^{-3} - 1.3 \cdot 10^{-2}$	3.6 – 24.1	$4.4 \cdot 10^{-3}$
Impinging jets 0g	$4.4 \cdot 10^{-3} - 4.1 \cdot 10^{-2}$	–	$3.7 \cdot 10^{-3}$
Bubble coalescence	$4.5 \cdot 10^{-5} - 2.7 \cdot 10^{-2}$	0.7 – 1.8	$6.7 \cdot 10^{-3} - 2.0 \cdot 10^{-2}$

Experiment	Re	We	Ca
Bubbly jets 1g	320 – 1000	1.4 – 13.7	$1.4 \cdot 10^{-3} - 4.3 \cdot 10^{-2}$
Bubbly jets 0g	320 – 3000	1.4 – 123.4	$4.7 \cdot 10^{-4} - 3.9 \cdot 10^{-1}$
Droplet jets 1g	154 – 455	0.46 – 4.05	$1.0 \cdot 10^{-3} - 2.6 \cdot 10^{-2}$
Droplet jets 0g	154 – 455	0.46 – 4.05	$1.0 \cdot 10^{-3} - 2.6 \cdot 10^{-2}$
Impinging jets 1g	210 – 1400	0.9 – 38.4	$6.4 \cdot 10^{-4} - 1.8 \cdot 10^{-1}$
Impinging jets 0g	320 – 3000	1.4 – 123.4	$4.7 \cdot 10^{-4} - 3.9 \cdot 10^{-1}$
Bubble coalescence	5 – 300	0.01 – 4	$3.3 \cdot 10^{-5} - 0.8$

Table 2.1: Ranges of dimensionless numbers studied in the different experiments.

Liquid	ρ (kg/m^3)	ν (m^2/s)	γ (N/m)
Distilled water	998	$1 \cdot 10^{-6}$	$7.28 \cdot 10^{-2}$
Ethanol	789	$1.52 \cdot 10^{-6}$	$2.24 \cdot 10^{-2}$

Table 2.2: Physical properties of the liquids used, at 20° C and at ambient pressure. ρ is the density, ν is the kinematic viscosity and γ is the surface tension with respect to air.

Gas	ρ (kg/m^3)	ν (m^2/s)
Filtered air	1.21	$15.11 \cdot 10^{-6}$
Carbon dioxide	1.87	$13.70 \cdot 10^{-6}$

Table 2.3: Physical properties of the gases used, at 20° C and at ambient pressure. ρ is the density and ν is the kinematic viscosity.

The ranges of dimensionless numbers studied in the different experiments are presented in Table 2.1. Definitions of dimensionless numbers (Bond, Froude, Ohnesorge, Reynolds and Weber) are presented in the List of Symbols.

The physical properties of the materials used are presented in Tables 2.2 and 2.3 for liquids and gases respectively.

2.1 Bubbly jets

2.1.1 Bubble generation method

The generation of bubbles of controlled size in a low gravity environment is not trivial: if air is injected through a capillary tube into a tank full of liquid, a bubble is created, increasing its size while the gas flow rate is different from zero. However, this increasing bubble can be detached from the nozzle in a highly uncontrollable way, as can be seen in Figure 2.1(a). Consecutive detachments result in the creation of numerous bubbles with uncontrolled sizes. Thus, at any perturbation of the fluid motion, a bubble can be detached from the nozzle, allowing another bubble to be created and subsequently detached, and so forth.

In order to generate numerous millimetric bubbles in a microgravity environment (see Figure 2.1(b)), the solution that we have adopted is to use the “bubble injectors” method[2], which create the bubbles at the desired size, prior to injection into the tank full of liquid. To achieve this, a crossflow configuration is created inside a 0.7 mm (in normal gravity) or 1 mm (in microgravity) capillary T-junction. From one branch of the T-junction (the so-called “straight branch”), a constant liquid flow is introduced,

---

[2] Proposed in Carrera et al. [CRRP$^+$08]

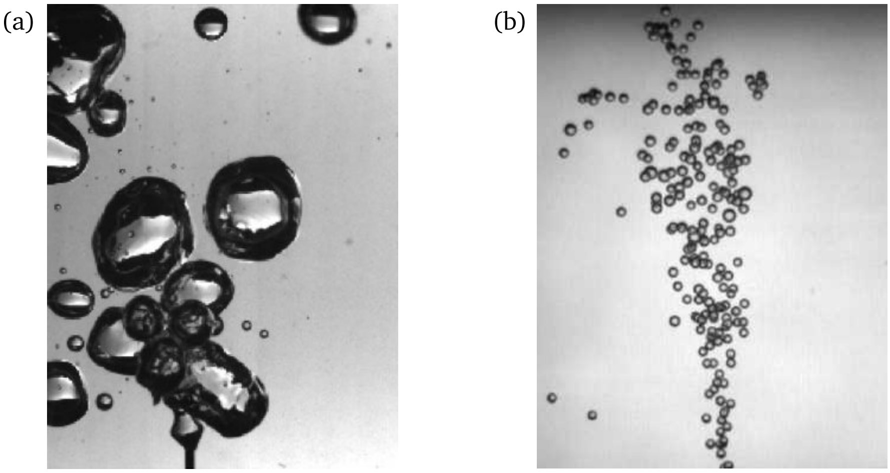

Figure 2.1: Snapshots of bubbles generated in microgravity. (a) Generation by air injection through a capillary tube (From Carrera et al. [CPG06]). (b) Generation by bubble injectors (From Carrera et al. [CRRP+08]).

while a constant gas flow is injected from the other branch (the "crossed branch")[3]. This method can generate a regular slug flow, in which the final bubble size and generation frequency is governed by the gas and liquid flow rates. A capillary tube with the same diameter of each injector branches and length larger than 70 mm carries the bubbles from the injector outlet to the test tank, ensuring stationary slug flow conditions.

In Figure 2.2, a snapshot of the bubble generation method and the created slug flow is presented.

This method is insensitive to gravity force and is mainly dominated by capillary forces, since Bond number is very low,

$$\mathrm{Bo} = \frac{\Delta\rho g d_C^2}{\gamma} < 1, \tag{2.1}$$

where $\Delta\rho$ is the density difference between the two phases, g is the acceleration of gravity, d_C is the capillary diameter and γ is the surface tension. Hence, the behavior of the injection device in low gravity is the same as on-ground and we can fully characterize the operation of the injectors in normal gravity. An extensive range of bubble generation frequencies (up to 1000 bubbles per second in the present study) can be achieved. Bubble sizes and velocities at the outlet of the injector

---

[3] Additional experiments have been carried out injecting the liquid through the crossed branch and the gas through the straight branch, but the injector operation is not so effective creating a regular slug flow, with uniform bubble diameters and a constant generation frequency.

Figure 2.2: Illustration of the bubble generation method.

are controlled by gas and liquid flow rates. The reader may refer to Carrera et al. [CRRP+08] and Arias et al. [ARC+09] for a detailed study of this bubble generation method.

2.1.2 Normal gravity setup

On-ground tests were conducted in a stainless steel rectangular tank with a length of 160 mm, width of 200 mm, and height of 250 mm, equipped with two methacrylate windows which allow the visualization of the bubble jets. The size of the test tank is large enough (compared to bubble diameter which is of order of 1 mm) to minimize any possible wall effects on the motion of the bubbles and the resulting jet structure. The test tank is initially filled with distilled and filtered water[4] (or ethanol[5]) by a high-accuracy pump (Ismatec MCP-Z Standard) which takes the liquid from the liquid tank. A T-junction bifurcation is used to divide the liquid flow in two sub-lines that transfer the liquid to the bubble injectors, ensuring an equal and constant flow rate for each sub-line. Liquid flow rates Q_L range from 15 ml/min to 30 ml/min for each injector, and are measured by a liquid flow meter (Bronkhorst L30). Gas (CO_2) is injected from a pressure bottle through a pressure controller (Bronkhorst P-702CV) and a choked orifice, setting the air flow rate Q_G from 1 ml/min to 20 ml/min for each injector. Gas flow rate is measured by an air flow meter (Bronkhorst F-201CV). Another T-junction bifurcation is used in the gas line to provide the air to each bubble injector. A residual tank is used to empty the excess of gas and liquid from the test tank, avoiding any risk of overpressure. The liquid and residual tanks are flexible high-resistance bags EVA[6] Nutribag (500 ml), protected by rigid plastic boxes. Initially, the bag corresponding to the liquid tank is completely filled with distilled water while the bag corresponding to the residual tank is in vacuum.

In Figure 2.3, a sketch of the experimental apparatus is presented.

The experiments were conducted at 20° C and at ambient pressure. A high-speed video camera (RedLake MotionXtra HG-SE) is necessary to catch all bubble coalescence events and the individual bubble motions. Lighting was provided by a

---

[4] Results using ethanol with a single jet and impinging jets are presented in Section 3.1.1 and 4.1.1 respectively.

[5] Results using distilled water are presented in Section 4.1.1.4.

[6] Ethilen-Vinil Acetate

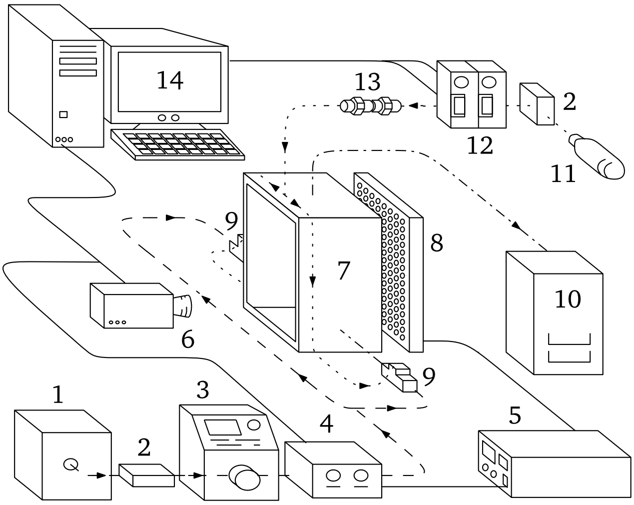

Figure 2.3: Experimental setup. Solid lines: electric connections, dotted lines: Gas tubes, dashed lines: liquid tubes, dash-dotted lines: gas-liquid tubes. 1: Liquid tank, 2: Filter, 3: Pump, 4: Flow meter, 5: Power supply, 6: HS Camera, 7: Test tank, 8: LEDs, 9: Injectors, 10: Residual tank, 11: Gas bottle, 12: Pressure controller and flow meter, 13: Choked orifice, 14: PC.

matrix of 280 ultra-bright LEDs and homogenized by a diffuser sheet. All the movies were recorded at 1000 fps with a resolution of 640x512 pixels (7 pixels correspond to 1 millimeter approximately), and post-processed by an image processing software. The basic experiment operations (full control of the gas and liquid lines, lighting and camera) can be controlled from a wired computer, but the change of the impact angle and separation distances between injectors has to be manipulated manually between two consecutive experiments.

2.1.3 Microgravity setup

The experimental setup has been designed to study the structure of bubbly jet impingement[7] in the ZARM Drop Tower facility (Bremen, Germany), which allows 4.7 seconds of 10^{-5}-10^{-6} g_0.

This setup is very similar to that presented in Section 2.1.2, with some differences as the integration within the drop capsule (arrangement of the setup is divided in 5 platforms), the size of the test tank, control of the setup via wireless and automatized camera trigger.

The experimental setup has been embedded in a rack to be used inside the capsule of a drop tower. A simplified sketch of the experimental setup and rack is shown

---

[7] Results are presented in Section 4.1.2.

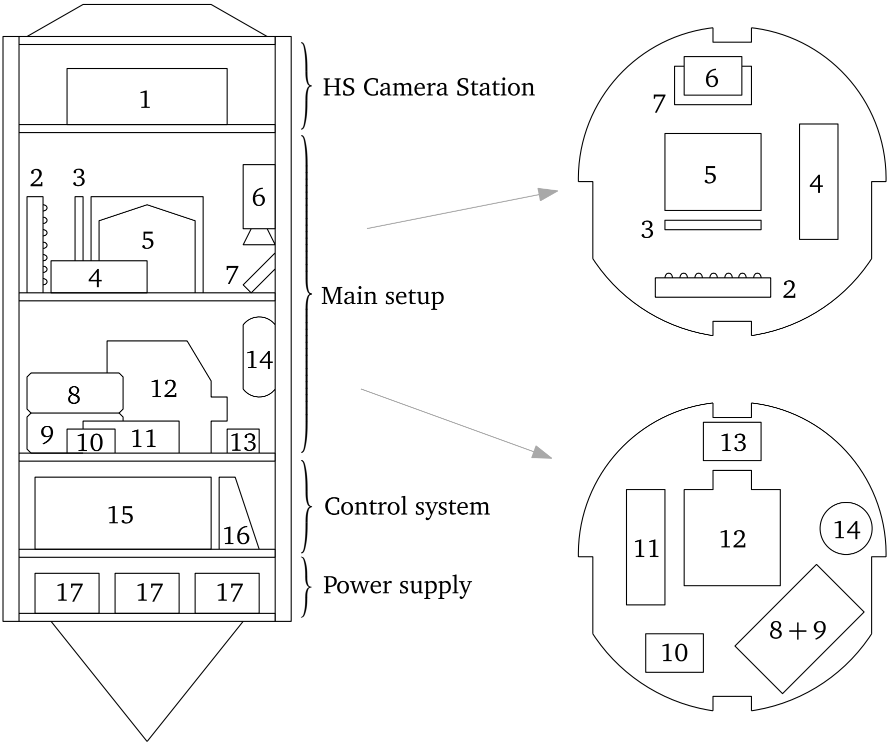

Figure 2.4: Sketch of the rack and the main setup (not to scale). 1: HS Camera control station, 2: Illumination system, 3: Diffuser sheet, 4: Pressure controller, 5: Test tank and injectors, 6: HS Camera, 7: Mirror, 8: Residual tank, 9: Liquid tank, 10: DC/AC Inverter, 11: Gas flow meter, 12: Liquid pump, 13: Choked orifice, 14: Gas tank and filter, 15: NI's PXI, 16: Acquisition connection device, 17: Batteries.

in Figure 2.4.

The main body of the setup is the test section, which consists of a $160 \times 100 \times 100$ mm^3 stainless steel tank initially filled of liquid. The size of the tank is large enough (compared to the bubble mean diameter which is of order of 1 mm) to avoid any possible wall effects. The tank is provided with two methacrylate windows, which allow the illumination of its interior (using a matrix of 140 ultra-bright LEDs and a diffuser sheet) when the recording by the high-speed camera takes place. A high-speed camera (Photron Fastcam MC2) is used to capture the motion of individual bubbles and the whole jet structure. The high-speed camera is operated at 1000 frames per second and a resolution of 512×512 pixels in order to catch the coalescence phenomena between bubbles. The trigger is automatized to catch 0.5 s before the drop and 2.8 s after the drop, with a total time of 8 s for each movie.

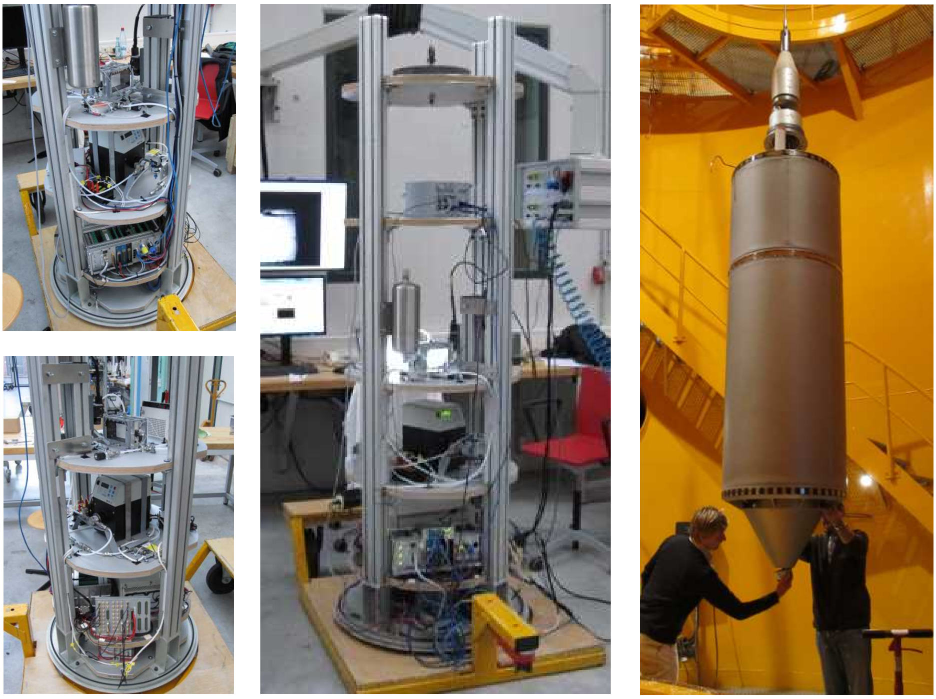

Figure 2.5: Pictures of the rack and the capsule used at ZARM Drop Tower.

Two bubble injectors, whose operation is described in Section 2.1.1, are placed inside the test tank one in front of each other. The impact angle between bubble injectors can be changed from 0°, which corresponds to a frontal collision between jets, up to 90°, corresponding to a perpendicular collision[8]. The distance between injectors can also be changed from 0 mm up to 100 mm. Bubble sizes and velocities can be controlled by changing the gas and liquid flow rates, Q_G and Q_L respectively.

Gas used is filtered air. Gas reservoir consists of a Festo's 2 L alluminum tank with a pressure of 6 bars. Gas flow meter and pressure controller, as well as the whole liquid line are the same as in Section 2.1.2. Experiments were carried out at ambient pressure and at 20° C.

The basic experimental operations, such as full control of the gas and liquid flow rates, lighting and camera, are governed remotely from a computer via wireless using LabView software. The change of the distance and the impact angle between jets are the only operations to be performed manually between two consecutive drops.

---

[8] Only 5 drops have been carried out at the moment of writing this thesis. Distance between injectors and flow rates have been changed in those drops, but the injection angle have been kept constant at 0° (frontal collision).

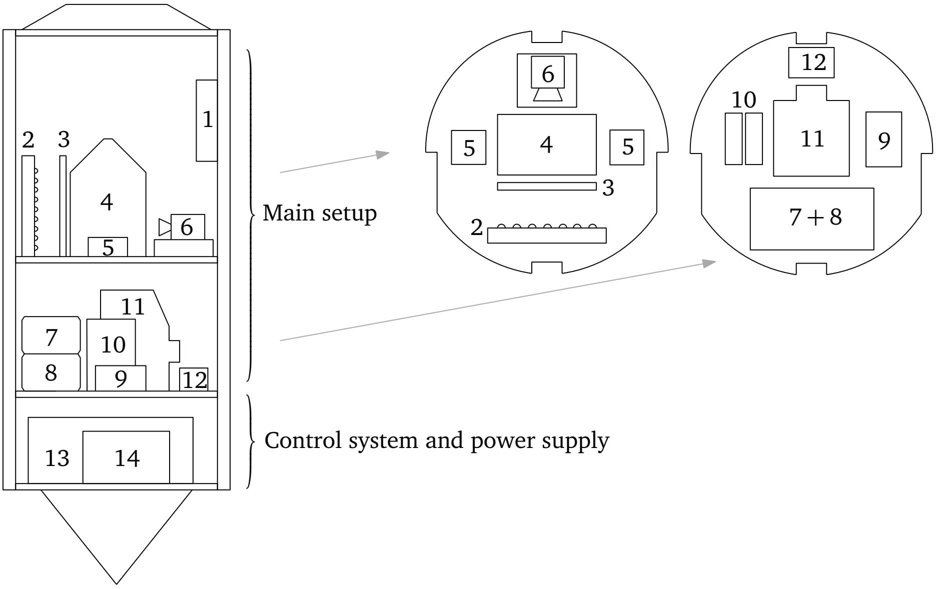

Figure 2.6: Sketch of the experimental setup for the study of droplet jets. 1: Acquisition connection device, 2: LEDs, 3: Diffuser sheet, 4: Test tank, 5: Injectors, 6: HS Camera, 7: Residual tank, 8: Liquid reservoir, 9: DC/AC Inverter, 10: Liquid flow meter, 11: Liquid pump, 12: Filter, 13: NI's PXI, 14: Batteries.

In Figure 2.5, pictures of the rack and the capsule are presented.

2.2 Droplet jets

Unlike with bubbly jets, the experimental results on liquid jets in normal gravity and in microgravity were obtained using exactly the same setup[9]. In order to study the breakup of a liquid jet and droplet dynamics in a microgravity environment, the setup was designed to be used in the INTA's Drop Tower (Torrejón de Ardoz, Spain), which allows of 2.1 s of 10^{-4}-10^{-5} g_0.

Liquid jets are injected into a stainless steel rectangular tank (with a length of 160 mm, width of 200 mm and height of 250 mm) provided with two methacrylate windows which allow the visualization of the interior of the tank.

The liquid used is distilled water, which is directed to the test tank from a flexible bag (EVA Nutribag 500 ml, initially filled with distilled water) through a liquid pump (Ismatec MCP-Z Standard), and the liquid flow rate Q_L is measured using a liquid flow meter (Bronkhosrt L30). Liquid flow rates are increased from 5 ml/min

---

[9] Results in normal gravity and in microgravity are presented in Section 3.2.1 and 3.2.2 respectively.

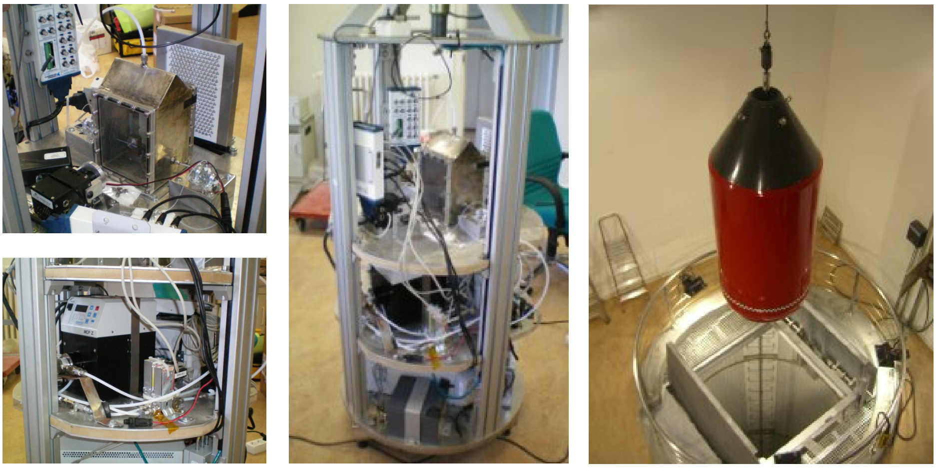

Figure 2.7: Pictures of the rack and the capsule used at INTA's Drop Tower.

up to 15 ml/min. The nozzle internal diameter is $d_C = 0.7$ mm and the external diameter is $d_{ext} = 1.8$ mm. The experiments were conducted at room temperature (around 20° C) and at ambient pressure. An initially empty flexible bag (EVA Nutribag 500 ml) is connected to the test tank, avoiding any risk of overpressure. A high-speed camera (RedLake MotionXtra HG-SE) records the jets at framerates between 500 and 1000 frames per second (recording images at 640×512 and 640×256 pixels respectively), depending on the experiment run. The high-speed camera has a builtin battery and internal memory, and is activated when a trigger signal is received. The spatial resolution of the aquired images is 0.15 mm per pixel.

The illumination system consists of a matrix of 280 ultrabright LEDs which lighting is homogenized by a diffuser sheet. The flow rate of the liquid pump as well as the aqcuisition system are controlled via wireless by LabView software. In Figures 2.6 and 2.7, a sketch and pictures of the experimental setup are presented respectively.

2.3 Bubble bouncing and coalescence

The experimental setup for the observation of bubbles impacting at a free surface[10] is illustrated in Fig. 2.8.

A cubic methacrylate tank of $250 \times 250 \times 250$ mm^3 is filled with ethanol at a height of 20 cm. The upper part of the cubic tank is opened, keeping the pressure at atmospheric pressure. Air bubbles with equivalent radius between 0.1 and 2 mm

---

[10] Results are presented in Chapter 5.

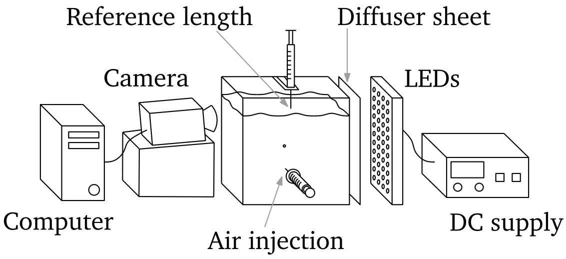

Figure 2.8: Experimental setup for the observation of bubbles impacting at a free surface.

approximately are released from a syringe placed at the bottom of the tank, and rise to the free surface under the action of the buoyancy force. Bubbles with diameters higher than 2 mm rise following an helical path, not an straight line, hence the collision with the free surface is no longer axisymmetric. For this reason, the results presented herein have a diameter range between 0.2 mm and 2 mm.

The model of the syringes used is Icopiuma Self 0.5 ml, which has a stainless steel tip of 0.3 mm external diameter and 0.1 mm internal diameter. Another syringe tip of 0.3 mm external diameter is placed crossing vertically the free surface, at approximately 1 cm from the impact point in order to give a reference length for the measurement of the bubble size. The distance between the reference syringe tip and the impact point is large enough to ensure no considerable perturbations at the free surface.

The motion of the bubbles is recorded by means of a high-speed camera RedLake MotionXtra HG-SE with a framing rate of 2000 s^{-1}, and an image resolution of 640x512 pixels each frame. The camera is placed slightly below the free surface level with an inclination angle of 5°. This is necessary to avoid blurred captures of the free surface due to the depth of field effect, and leads to the recording of both real and mirror images of the bubble. Backlight is provided by a matrix of 15×10 ultrabright LEDs (10000 mcd each), placed at 15 cm from the test tank, and homogenized by a diffuser sheet. The LEDs are chosen as lighting candidates with the aim to avoid temperature changes between series of experiments, which were all conducted at 20° C and at ambient pressure.

CHAPTER 3

Two-phase jets

The structure of single jets (no impingement nor any other opposed-jet configuration considered, just one jet) is studied in this chapter. The jets analyzed in this chapter are two-phase (gas-liquid) jets. In particular, bubbly jets and droplet jets will be studied. In Section 3.1.1, the behavior of bubbly jets in normal gravity is considered. The results of bubbly jets obtained in microgravity are presented in Section 3.1.2. Regarding droplet jets, they are studied in Section 3.2.1 and 3.2.2 for the normal gravity and microgravity conditions, respectively.

3.1 Bubbly jets

3.1.1 Bubbly jets in normal gravity

With the aim of carrying out a fundamental analysis of the behavior of bubbles and jets after injection in normal gravity, we have used the described experimental setup with one injector. Different gas and liquid flow rates, and variations of the orientation angles of the injector with respect to the gravity field have been considered.

According to Schlichting [Sch79], the momentum flux J can be considered as the main parameter that characterizes the structure of a single-phase jet,

$$J = 2\pi\rho \int_0^\infty r v_\ell^2 dr \tag{3.1}$$

where ρ is the density of the fluid, v_ℓ is the velocity in the direction of injection, and cylindrical coordinates (r, θ, ℓ) are used. Taking into account the effect of both gas

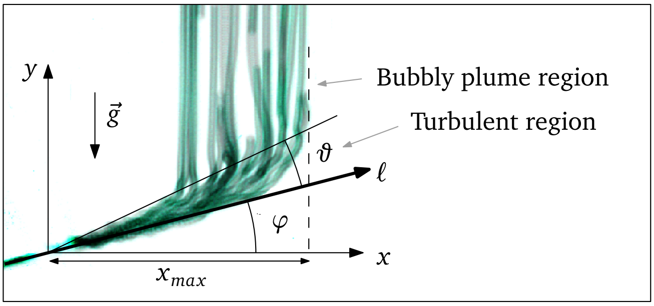

Figure 3.1: Schematic definition of the delimitation angle ϑ and the injection angle φ.

and liquid phases, the momentum flux can be computed as

$$J = J_L + J_G = 2\pi\rho_L \int_0^\infty r\left(\frac{Q_L}{A}\right)^2 dr + 2\pi\rho_G \int_0^\infty r\left(\frac{Q_G}{A}\right)^2 dr, \tag{3.2}$$

where the liquid velocity is approximated by $v_\ell^{(L)} \approx Q_L/A$, and the gas velocity is approximated by $v_\ell^{(G)} \approx Q_G/A$, being $A = \pi d_C^2/4$ the area of the capillary. Q_L and Q_G correspond to the liquid and gas flow rates, respectively. Hence,

$$J = \frac{4}{\pi d_C^2}\left(\rho_L Q_L^2 + \rho_G Q_G^2\right). \tag{3.3}$$

The momentum flux J is indicative of the jet strength, and most of the results presented in this section are based on this parameter. It is important to note that high values of J are necessarily due to high values of the liquid flow rate Q_L: increasing the gas flow rate Q_G results in a very small change in J since the parameter ρ_G is multiplying the gas flow rate, and $\rho_G \ll \rho_L$. This leads to the physical result that smaller bubbles are created at higher momentum fluxes, while at lower values of J both the gas and liquid flow rates can contribute substantially to modify the momentum flux, and small and large bubbles can still be found.

In Figure 3.1, a schematic definition of the delimitation angles and the axis used is presented. The angle between the direction of injection and the horizontal is denoted by φ, while ϑ represents the delimitation angle between the inertial zone and the bubbly plume zone.

3.1.1.1 Individual trajectories and maximum distance

In order to study the dynamics of bubbles after injection, the trajectories of individual bubbles have been tracked. The time evolution of both x (horizontal direction)

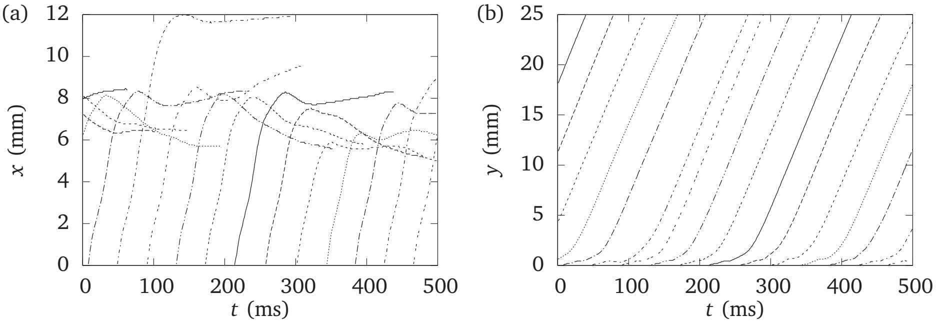

Figure 3.2: Time evolution of bubble center positions for several bubbles. (a) x coordinate (injection direction) as a function of time. (b) y coordinate (direction of gravity) as a function of time.

and y (direction of gravity) coordinates of the center position of several injected bubbles is shown in Figure 3.2(a) and 3.2(b) respectively. These data have been obtained with $Q_G = 1$ ml/min and $Q_L = 16.7$ ml/min, and the injector oriented perpendicular to the gravity direction ($\varphi = 0$), thus in this particular case, the injection direction ℓ coincides with the horizontal direction x.

In Figure 3.2(a), it can be observed that at the exit of the injector, bubbles follow a rectilinear trajectory at uniform velocity until a position at approximately 8 mm away from the injector. At this position, velocity suddenly decreases and bubbles suffer a backward movement that varies their x coordinate between 0.5 and 2.5 mm approximately. Taking the slope of the linear region in $x(t)$, the speed of bubbles at the exit of the injector is obtained, $v_x = 0.171 \pm 0.002$ m/s. It can also be observed in Figure 3.2(a) that bubble generation frequency is very uniform. At these low values of the flow rates, the generation frequency is very low[1], $f_g \approx 26$ bubbles/s.

In Figure 3.2(b), the plot of $y(t)$ for different bubbles shows a common tendency to a linear behavior just 70 ms after bubbles leave the injector, which gives a rise velocity of $v_R = 0.1740 \pm 0,0002$ m/s. This value is the same for each bubble, which demonstrates that all the injected bubbles have approximately the same size.

The maximum distance reached by bubbles in the direction of injection gives information about the jet geometry since is an indication of the resulting force acting on bubbles. Figure 3.4 shows the dependence of x_{max} on the momentum flux J for different gas flow rates. x_{max} is defined as the maximum distance reached by bubbles in the direction of injection in a range $\Delta y = 1d_C$, d_C being the capillary tube diameter.

A schematic definition of x_{max} is presented in Figure 3.3.

---

[1] The generation frequency is low compared with generation frequencies of the order of 1000 bubbles per second which are obtained in other tests using the same injector.

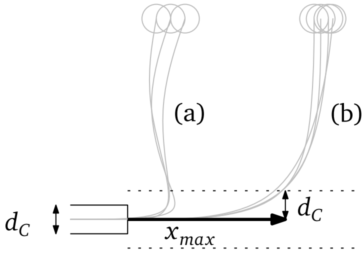

Figure 3.3: Schematic definition of the maximum distance reached x_{max}. (a) and (b) correspond to the dripping and jetting regimes respectively.

The behavior of x_{max} as a function of the momentum flux J is observed to be approximately linear in a wide region of the considered parameter ranges, with higher slopes when lower gas flow rates are injected. For any studied values of Q_G and $J < 10$ g cm/s^2, bubbles are injected with a low speed and quickly start to rise at only 2 mm away from the injector (region (a) in Figures 3.4 and 3.3). However, for $10 < J < 15$ g cm/s^2, there is a sudden increase in the maximum distance reached, especially the cases with $Q_G = 0.5$ ml/min and $Q_G = 1$ ml/min. This is due to a nozzle effect, which is also present in the case of water droplets in air[2]. This sudden increase in the maximum distance reached determines two kind of regimes when using water droplets in air: the dripping regime, and the jetting regime. Increasing the liquid flow rate gradually, droplets are created at the nozzle tip, dripping for low flow rates. Increasing a little bit more the liquid flow rate, a sudden transition to the jetting regime is observed: suddenly, a jet is created and the droplets detach from the nozzle. A similar effect occurs with air bubbles in water. As soon as the bubble comes out from the nozzle, there is an adhesion force between the bubble and the nozzle. When the inertia forces are greater than the surface forces, the behavior undergoes a jetting regime ($J > 15$ g cm/s^2, region (b) in Figures 3.4 and 3.3). It can also be observed that for a fixed value of J, the maximum distance is higher for low values of gas flow rate, although the exit speed is lower at small Q_G. In this case, bubbles are smaller and they are carried by the liquid jet for a longer distance in x since the buoyancy force is weaker.

3.1.1.2 Turbulence and buoyancy regions

Since the velocity of the bubbles inside the jets is very high (unless very low values of the flow rates are used), the human eye is not able to see the individual motion of those bubbles. Visually, two distinct regions are clearly observed (also observed by Lima Neto et al. [NZR08b] in their work of horizontal injection of gas-liquid mixtures in water): a bubbly cone emerging from the outlet of the capillary tube in

---

[2] The case of water droplets in air is discussed in Section 3.2.1.

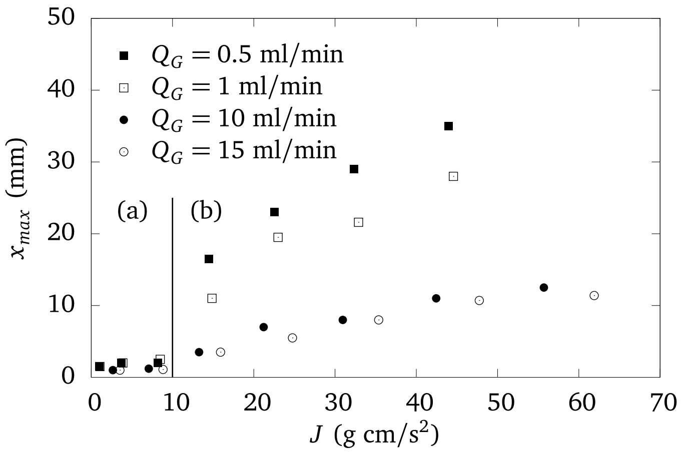

Figure 3.4: Maximum distance reached x_{max} as a function of the momentum flux J for different gas flow rates Q_G. (a) dripping regime, (b) jetting regime.

the direction of injection, and a vertical bubbly plume in which the bubbles follow an approximately rectilinear path (see Figure 3.1). In the first region, the jet strength is very high and is characterized by violent motion. Bubble dynamics are mainly dominated by inertial forces. Recorded movies show the paths of individual bubbles presenting some random oscillations typical of turbulent flows, and the shape of this zone is very similar to the conical shape of the single phase jet, but slightly deviated upwards in the vertical direction. On the contrary, the second region is formed by bubbles rising vertically at a constant and much slower velocity, the buoyancy is compensated by the drag force and no significant occurrence of coalescence events is observed. This bubbly plume is formed by bubbles that escaped from the bubbly jet zone, either by turbulent diffusion or by previously coalesced bubbles submitted to a strong buoyant force due to their larger size.

In order to delimit the two regions described, we averaged all the frames in a movie, and it was observed that the transition zone could be approximated by a straight line[3] tilted an angle[4] ϑ with respect to the injection direction ℓ.

The dependence of ϑ with respect to the momentum flux J is shown in Figure 3.5. This plot was obtained with a fixed injection angle $\varphi = 0°$, corresponding to horizontal injection. The delimitation angle ϑ decreases as the momentum flux J is increased, due to the fact that, larger momentum fluxes correspond to smaller bubbles, which have a relatively large velocity at the nozzle, and are carried away

---

[3] The delimitation between the bubbly plume zone and the turbulent region can be approximated by a straight line when using one single injector. However, when using multiple jets interacting with each other (as we shall see with impinging jets in Chapter 4), this approximation is not valid anymore.

[4] In Figure 3.1, a schematic definition of ϑ is shown.

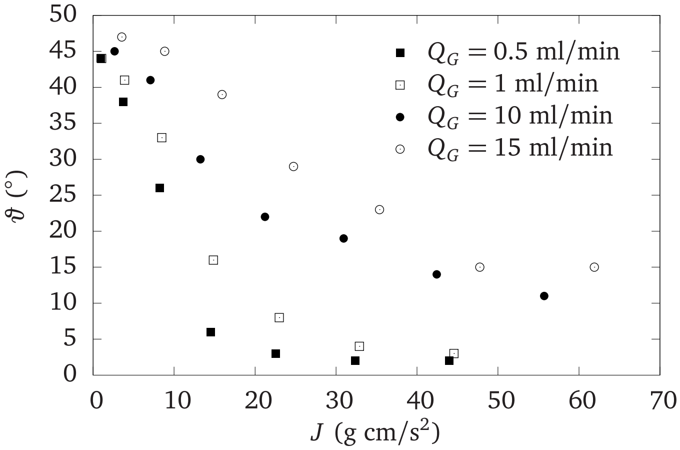

Figure 3.5: Angle ϑ as a function of momentum flux J.

from the nozzle exit by the liquid jet. On the contrary, at low values of J, bubble diameters are higher, and the buoyancy force is much stronger, hence the bubble trajectory is deviated upwards as soon as the gravity force becomes predominant over the inertia forces. In addition, at a fixed J value, ϑ is higher at larger values of the gas flow rate Q_G which is related to the fact that, being buoyancy force proportional to bubble size, larger bubbles begin to ascend at smaller distances with respect to the exit of the injector.

3.1.1.3 Variation of injection angle with respect to gravity

The dependence of the maximum distance reached x_{max} and the delimitation angle ϑ on the momentum flux has also been studied for different values of the orientation angle φ.

It can be observed in Figure 3.6(a) that for a fixed value of the momentum flux J, x_{max} is higher at higher values of φ. The plot have been obtained by maintaining a fixed gas flow rate $Q_G = 30$ ml/min, with different values of liquid flow rate Q_L to obtain the present range of the momentum flux J. Injection angles have been increased from $\varphi = 0°$ to $\varphi = 30°$. The component of the buoyancy force in the direction of injection increases at larger φ, being therefore a greater maximum distance reached.

Figure 3.6(b) shows the dependence of ϑ with the momentum flux J for three injection angles. It can be observed that for a fixed J value, ϑ diminishes as φ is increased. This can be explained in the same way as done for Figure 3.6(a), since if increasing φ the maximum distance increases, it is natural to deduce that the angle ϑ diminish in a similar fashion.

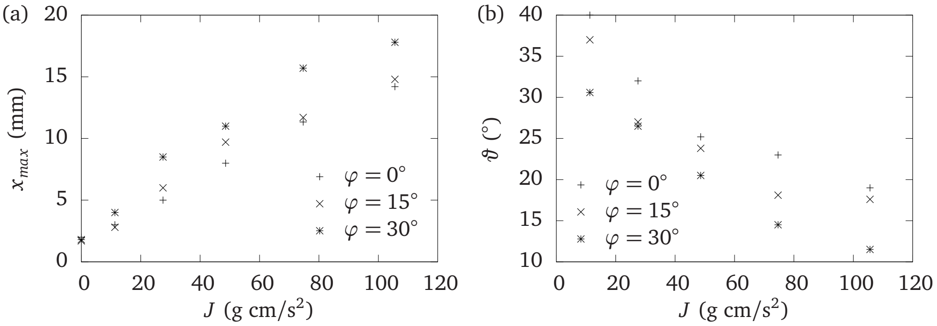

Figure 3.6: (a) Maximum distance reached x_{max} as a function of momentum flux J for different injection angles φ. (b) Delimitation angle ϑ as a function of the momentum flux J, for different injection angles φ.

3.1.2 Bubbly jets in microgravity

In order to study the behavior of bubbly jets in microgravity, the experimental setup described in Section 2.1.3 have been used at the ZARM Drop Tower in Bremen.

The procedure to study the bubbly jets is the following: when the capsule is in the top of the Drop Tower, ready to be dropped, the liquid pump is activated and after 10 seconds the air valve is opened. After a few seconds[5], the air enters the test tank forming the bubbly jet. Once the bubbly jet is stabilized[6], the capsule is dropped.

In the initial instants of the zero gravity phase, the fluid flow field is still perturbed by the bubbles which rose to the top of the test tank when the gravity force was non-zero. This perturbation is the responsible of some presence of small bubbles in the upper part of the jet, which is not perfectly axisymmetric in the first few milliseconds of zero gravity.

A possible way to avoid this fluid flow field perturbation, would be to generate the bubbly jets once in microgravity, but the time interval between the aperture of the air valve and the instant at which the air enters the test tank is highly unpredictable and can reach up to 5 s. Since the available microgravity time in the ZARM Drop Tower is 4.74 seconds, there is the risk of opening the gas valve with no air entering the test tank in the whole drop, which would be a too risky procedure.

In Figure 3.7(a), the normalized gravity level as a function of time for a whole drop is presented. After the capsule is dropped, the gravity level undergoes high-frequency damped oscillations, reaching negative values of g up to $g = -0.7g_0$. After 0.7 s approximately, these oscillations can be neglected and the gravity level

---

[5] Depending on the gas and liquid flow rates used, the time interval between the aperture of the air valve and the entrance of the air into the test tank varies from 1 to 5 seconds.

[6] The stabilization time varies from 20 to 40 seconds approximately.

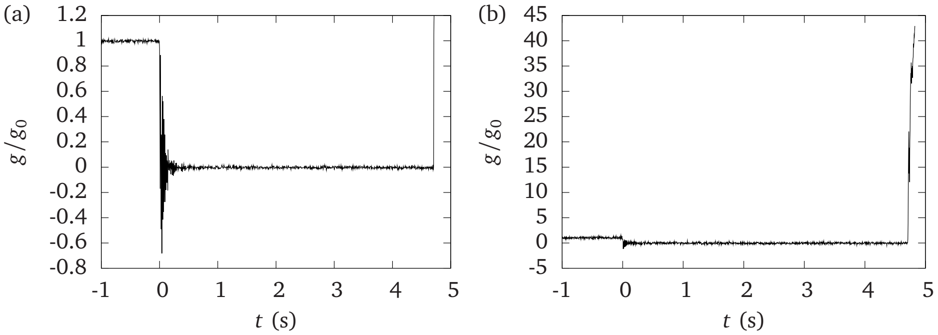

Figure 3.7: Normalized gravity level as a function of time. (a) Oscillation of gravity level (with negative values of gravity) after capsule release. (b) Up to $g/g_0 \approx 40$ when the capsule is decelerating.

stabilizes with some significant g-jitter.

Figure 3.7(b), is the same as Figure 3.7(a) with a different scaling factor. The reason for including Figure 3.7(b) is the fact that during the capsule deceleration, high gravity levels are reached, up to $g = 40g_0$ approximately, and using this scale factor the decelerating gravity level can be appreciated in more detail.

In Figure 3.8, snapshots of growing bubbly jets are presented for different values of the momentum flux J. For a given gas flow rate, using high values of the liquid flow rate results in high values of J. In this case, small bubbles are generated, as can be seen in Figure 3.8(a). On the other hand, using low values of the liquid flow rate, bigger bubbles are generated as can be seen in Figure 3.8(c). The effects of the flow field perturbation by the residual fluid flow can be appreciated in Figures 3.8(b) and 3.8(c), since some bubbles are in the upper part of the jet breaking the axisymmetry. This effect is higher for larger bubbles due to the fact that the buoyancy force is proportional to the bubble volume.

3.1.2.1 Individual trajectories

Individual trajectories of 10 bubbles have been obtained in the earlier times of a growing jet, with $J = 16\,\mathrm{g\,cm/s^2}$.

In Figure 3.9(a), the x-coordinate of the center of the bubbles is plotted as a function of time. The bubble center average velocity in the injection direction just after detachment is approximately $v_x = 1$ m/s, being slightly reduced as the jet grows. The slopes of the lines decrease as the bubble reach higher distances from the jet nozzle.

The y-coordinate of the center of the bubbles is plotted as a function of time in Figure 3.9(b). The bubble vertical positions follow a random diffusive movement

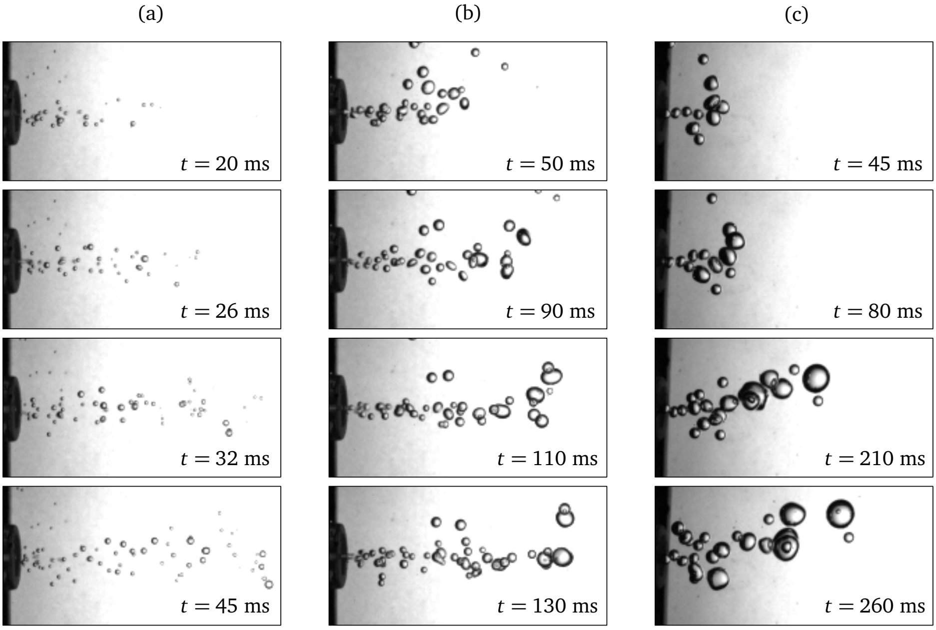

Figure 3.8: Snapshots of single bubbly jets in microgravity, for (a) $J = 176$ $\mathrm{g\,cm/s^2}$, (b) $J = 64$ $\mathrm{g\,cm/s^2}$ and (c) $J = 1.8$ $\mathrm{g\,cm/s^2}$.

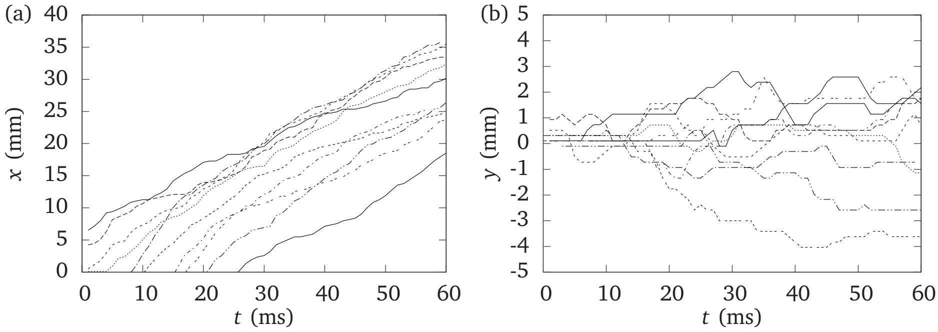

Figure 3.9: Time evolution of bubble center positions for several bubbles in microgravity. (a) x-coordinate (injection direction) as a function of time. (b) y-coordinate (perpendicular direction to injection direction) as a function of time.

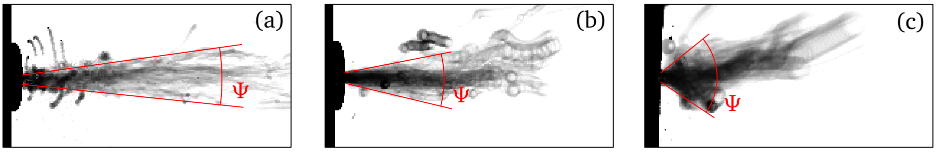

Figure 3.10: Averages of 200 frames of single bubbly jets in microgravity, for different values of the momentum flux J.

which is the responsible of the conical shape of the jet. It can be noted that one bubble is at $y \approx 1$ mm at $t = 0$. This is due to the fact that this bubble was already inside the test tank when the bubble tracking started.

Comparing the microgravity case with the normal gravity case (Figures 3.9 and 3.2 respectively), one notes that in microgravity the bubble velocity in the injection direction is approximately constant (although a slight decrease in velocity is observed far from the nozzle), while in the normal gravity case (Figure 3.2(a)), the bubbles suffer a high deceleration after 50 ms, in some cases resulting in a negative velocity in the injection direction. The $y-$coordinate, reaches a steady state (constant slope) in the normal gravity case, while in microgravity, a diffusive movement is the predominant behavior.

3.1.2.2 Opening angle

The global structure of the bubbly jets in microgravity can be approximated by a conical shape. The parameter that characterizes this conical shape is the opening angle of the cone, Ψ. In Figure 3.10, the definition of the conical opening angle Ψ is presented. The images are obtained by averaging 200 frames of the movies obtained at a) $J = 176\ g\,\text{cm}/\text{s}^2$, b) $J = 64\ g\,\text{cm}/\text{s}^2$ and c) $J = 1.8\ g\,\text{cm}/\text{s}^2$.

A plot of the opening angle Ψ as a function of the momentum flux J is presented in Figure 3.11. Only 5 values of J are presented due to the fact that only 5 drops with bubbly jets were carried out. The opening angle decreases as the momentum flux in increased, due to the fact that larger momentum fluxes correspond to smaller bubbles, which are dragged out of the nozzle by the liquid jet. The smaller a bubble is, its movement can be considered passive, following the liquid flow field. However, larger bubbles are much more sensitive to the g-jitter and they become dispersed closer to the nozzle. For this reason, smaller bubbles are more collimated in the direction of injection.

Although the natural definition of the angles ϑ (normal gravity case) and Ψ (microgravity case) is different, both angles describe the visual opening of the jet, and is reasonable to make a qualitative comparison between them. Figures 3.5 and 3.11 present the variation of ϑ and Ψ as a function of the momentum flux J, respectively. Both angles decrease smoothly, in a similar fashion, as the momentum flux J is in-

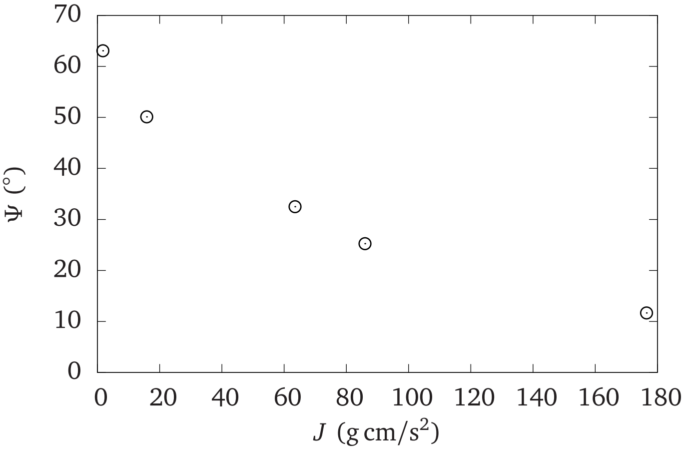

Figure 3.11: Conical opening angle Ψ for different values of the momentum flux J.

creased. This similar behavior reports that the inertial forces inside the turbulent zone are higher than the gravity forces, being the behavior of bubbles inside the turbulent zone very similar in both normal gravity case and microgravity case.

3.2 Droplet jets

Unlike with bubbly jets, concerning droplet jets the aerodynamic drag does not play any fundamental role in the dynamics of the droplets. Hence, the droplets do not follow the carrier fluid flow passively, as in the case of bubbly jets.

3.2.1 Droplet jets in normal gravity

3.2.1.1 Jet breakup

In the present study, a liquid jet is created by injecting a fixed liquid flow rate Q_L through a capillary tube (inner diameter $d_C = 0.7$ mm) oriented perpendicularly to the gravity direction. With this arrangement, two different regimes have been observed, by variating the liquid flow rate.

On one hand, when inertial forces are negligible compared to surface forces, a drop is formed at the nozzle outlet, growing with time without detaching from the nozzle. In this situation, the nozzle is leaking continuously: the dripping regime (see Figures 3.12(a) and 3.12(b)).

On the other hand, when inertial forces are predominant in front of surface forces, a jet is formed and the atomization occurs: the jetting regime. In this case,

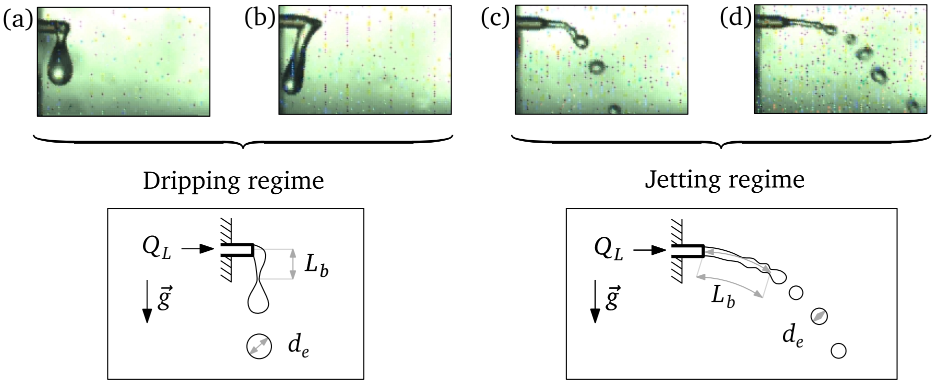

Figure 3.12: Snapshots of droplet jets at different flow rates. (a) $Q_L = 5$ ml/min. (b) $Q_L = 10$ ml/min. (c) $Q_L = 13.5$ ml/min. (d) $Q_L = 15$ ml/min.

the jet emerges from the nozzle and becomes curved downwards due to the action of the gravity force (as shown in Figures 3.12(c) and 3.12(d)). It is appropriate to introduce the Weber dimensionless number, which is a direct measure of the relative importance between the fluid's inertia compared to its surface tension

$$\mathrm{We} = \frac{\rho v^2 d_C}{\gamma} \tag{3.4}$$

where $v = 4Q_L/\pi d_C^2$ is the fluid velocity and d_C is the capillary diameter.

In order to know in which position the jet breaks, forming droplets, the average breakup length $\langle L_b \rangle$ have been measured for different values of the liquid flow rate. The breakup length have been measured over an average of 500 frames, and the value have been obtained by measuring the length of a circular arc from the center of the nozzle to the average breakup position.

The obtained experimental results of the average breakup length are presented in Figure 3.13, as a function of the square root of the Weber number[7]. However, since the liquid properties remain constant and the nozzle do not change its diameter with time, the square root of the Weber number is proportional to the liquid flow rate

$$\sqrt{\mathrm{We}} \approx \sqrt{\frac{\rho}{\gamma d_C^3}} Q_L . \tag{3.5}$$

---

[7] The reason for choosing $\sqrt{\mathrm{We}}$ as the abscissa axis is for comparison with the microgravity case (Section 3.2.2). In zero gravity, the problem is axisymmetric and there is an analytical relation between $\langle L_b \rangle$ and $\sqrt{\mathrm{We}}$.

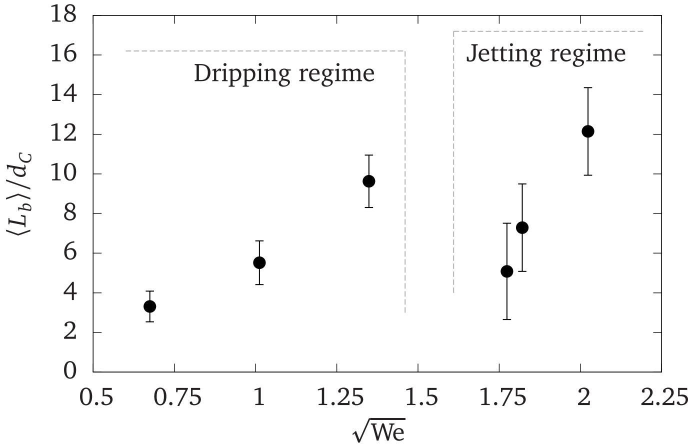

Figure 3.13: Average breakup length as a function of the square root of the Weber number.

Starting from low Weber numbers, as the liquid flow rate is increased, the breakup length increases until at $\sqrt{\mathrm{We}} \approx 1.5$ an abrupt reduction of the breakup length is found. The region $\sqrt{\mathrm{We}} \approx 1.5$ is the transition zone between the dripping regime and the jetting regime. Once in the jetting regime, the average breakup length also increases with the liquid flow rate, at the range studied.

Before reaching the breakup point, the liquid is contained in a curved cylinder with growing amplitude perturbations at its surface. Once the amplitude of these perturbations are equal to the cylinder radius, the liquid bulk breaks forming droplets of certain sizes. After the breakup point, intermittent droplets are generated. The sizes and trajectories of the generated droplets are examined in the following paragraphs.

3.2.1.2 Droplet sizes

Teng et al. [TKM95] studied the sizes of droplets after jet breakup for Newtonian and non-Newtonian fluids, obtaining the following equation for the droplet mean diameter

$$\frac{d_e}{d_C} = \left(\frac{3\pi}{\sqrt{2}}\right)^{\frac{1}{3}} (1 + 3\mathrm{Oh})^{\frac{1}{6}}, \tag{3.6}$$

where $\mathrm{Oh} = \frac{\mu}{\sqrt{\rho \gamma d_C}}$ is the Ohnesorge number. At the studied range of parameters, $\mathrm{Oh} \ll 1$ and $d_e \approx 1.88 d_C$.

Equation 3.6 can be modified in order to take into account the orifice effects,

$$\frac{d_e}{d_C} = 1.88\alpha (1 + 3\mathrm{Oh})^{\frac{1}{6}}, \tag{3.7}$$

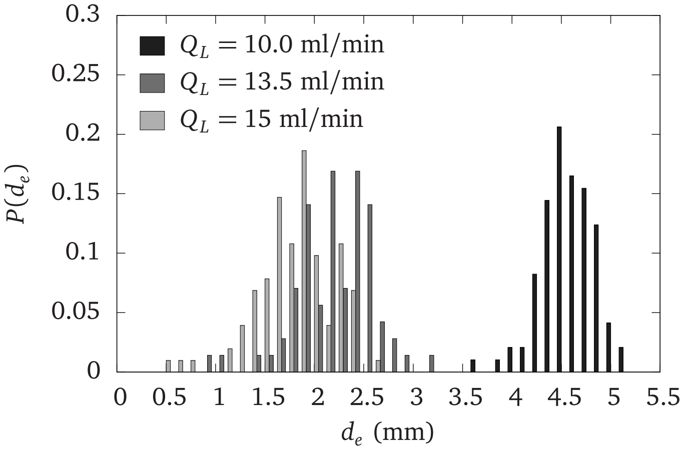

Figure 3.14: Droplet size distributions in normal gravity for different liquid flow rates Q_L.

where α in an empirical orifice parameter which has to be determined experimentally. Teng et al. [TKM95] obtained an empirical expression for the parameter α, which can be written as

$$\alpha = 1.13 + 0.02 \ln(3\mathrm{Oh}), \tag{3.8}$$

which leads to a droplet mean diameter of $d_e = 2.12 d_C$.

The sizes of the droplets created by jet atomization have been measured from the images recorded. Since the droplets are oscillating after jet breakup, an equivalent diameter d_e is defined as the diameter of the droplet containing the same volume of fluid as the oscillating drops. The measurements are taken from two-dimensional images, so the actual equivalent diameter d_e is such that

$$d_e = 2\sqrt{\frac{A_m}{\pi}} \tag{3.9}$$

where A_m is the measured area of the oscillating drops.

In Figure 3.14, the droplet size distribution is presented for three values of the liquid flow rate. The case $Q_L = 10$ ml/min, correspond to the dripping regime. In this situation, big droplets are leaking from the nozzle in a regular way. The mean equivalent diameter of these dripping droplets is $d_e \approx 4.5$ mm, and this size should be independent of the nozzle diameter d_C. The size distribution for the dripping droplets is narrow, indicating that all the droplets have approximately the same size.

As the liquid flow rate Q_L is increased, there is an abrupt reduction in the droplet mean size, corresponding to the transition into the jetting regime. In this regime, the generated droplets are much smaller ($d_e \approx 2$ mm) and the diameter distribution is

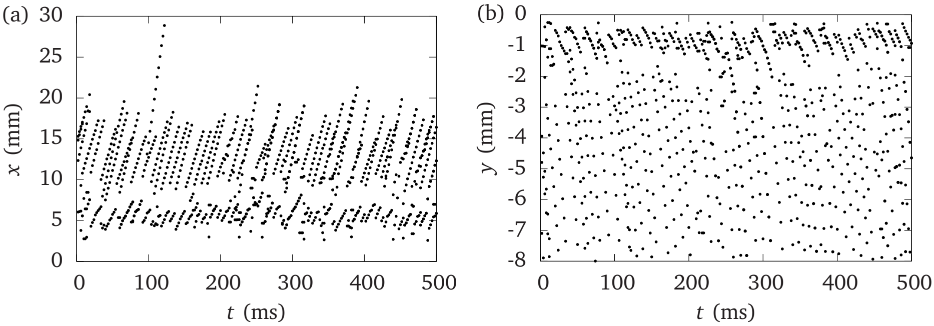

Figure 3.15: (a) x-coordinate (injection direction) of droplet centers as a function of time. (b) y-coordinate (gravity direction) of droplet centers as a function of time.

much wider, reflecting that the droplets are much more dispersed in size. This is mainly due to the droplet formation process itself, but also to some coalescence between droplets after generation. In fact, in the jetting regime, the collision between droplets after generation (resulting in bouncing or coalescence) is a phenomenon that occurs frequently. In this regime, within the range of flow rates studied, the droplet mean diameter decreases gradually as the liquid flow rate is increased. In all the cases, the droplet mean diameter obtained experimentally is higher than the theoretical prediction of Equations 3.6, 3.7 and 3.8. This is due to the coalescence between droplets after the droplet generation process, in the jetting regime. From the movies, numerous collisions between droplets are observed near the jet breakup zone, resulting in coalescence or bouncing. The bouncing does not change the size distribution. However, the coalescence events wider the tail in the droplet size distribution, and increase the droplet mean diameter.

3.2.1.3 Droplet trajectories

After atomization, the generated droplets follow a parabolic trajectory due to the action of the gravity force. An automatized method for tracking the droplet centers have been used for $Q_L = 15$ ml/min, which correspond to the jetting regime. In Figures 3.15(a) and 3.15(b), the x-coordinate and y-coordinate (gravity direction) of droplet centers are plotted as a function of time.

A region (between 5 and 10 mm in the x-coordiante, and -1 and -2 mm in the y-coordinate) in which the automatized tracking method crashes can be observed. This region corresponds to the breakup point. After this point, the droplets follow a parabolic trajectory: linear path in the x-coordinate and quadratic path in the y-coordinate.

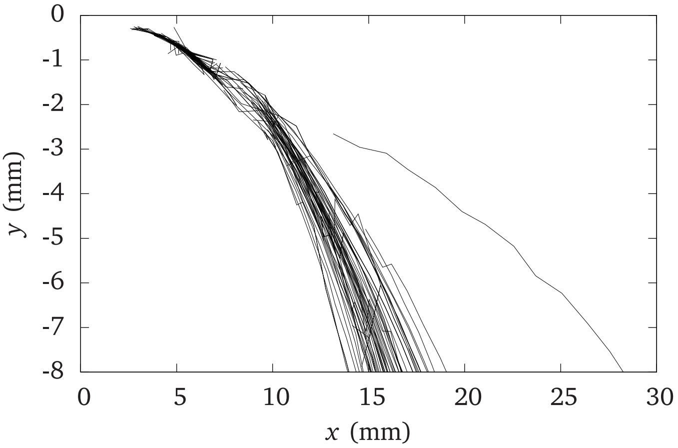

Figure 3.16: Map of droplet trajectories for $Q_L = 15$ ml/min.

In Figure 3.16, a map of the droplet trajectories is presented. From this map, a singular path that reaches x positions up to 28 mm (which corresponds to a satellite droplet), can be observed. The origin of this path does not correspond to the breakup point, indicating that the satellite droplet have been generated by the breakup mechanism of a larger droplet, or by an irregular breakup of the liquid jet, colliding and bouncing with other droplets. After examination of the recorded movies, we have seen that the satellite droplet is a small droplet generated by some irregularity in the jet breakup mechanism. After generation, the droplet collides with another bigger droplet and bounces, reaching larger distances in the injection direction than the average trajectories. Errors in the tracking process can be observed, both near the breakup point and also in the parabolic trajectories after atomization.

3.2.2 Droplet jets in microgravity

3.2.2.1 Jet breakup

When a liquid jet emerges from a nozzle in microgravity conditions, it quickly loses is cylindrical shape due to the action of inertial forces and surface tension forces. The cylindrical jet is perturbed by the competition between cohesive and disruptive forces giving rise to oscillations and perturbations. Under certain conditions, the oscillations can be amplified and the liquid body disintegrates into drops (primary atomization) at a distance L_b from the nozzle outlet. This jet breakup mechanism is the Rayleigh-Plateau instability, name due to the experimental work by Plateau [Pla73] and the theoretical analysis by Rayleigh [Ray78].

As in normal gravity, two different cases are examined. On one hand, when

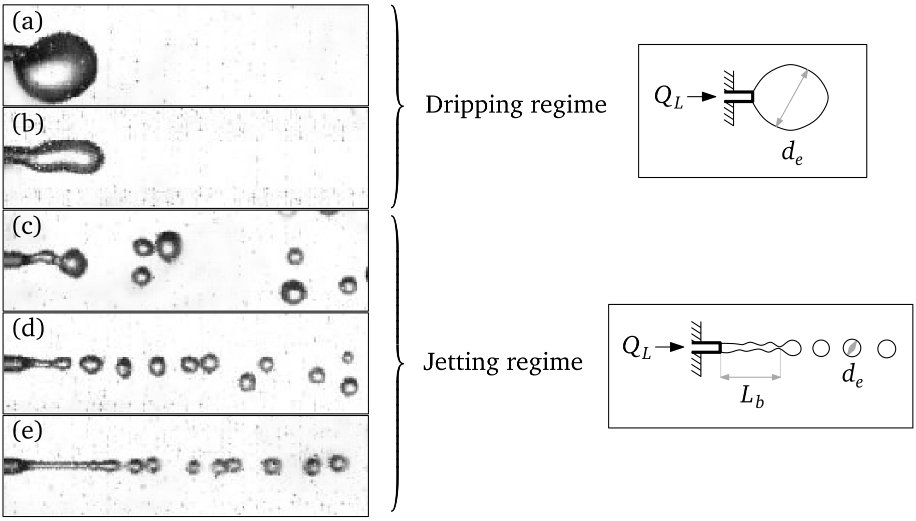

Figure 3.17: Snapshots of droplet jets at different flow rates. (a) $Q_L = 5$ ml/min. (b) $Q_L = 10$ ml/min. (c) $Q_L = 13.15$ ml/min. (d) $Q_L = 13.5$ ml/min. (e) $Q_L = 15$ ml/min.

inertial forces are negligible compared to surface forces, a droplet is formed at the nozzle outlet, growing with time without detaching from the nozzle. On the other hand, when inertial forces are predominant in front of surface forces, a jet is formed and the atomization occurs quickly. If the values of the parameters characterizing the jet correspond to the dripping regime in normal gravity, in microgravity a big droplet will be attached to the nozzle. In a similar way, the jetting regime in normal gravity corresponds to the jetting regime in microgravity. The Weber number ($\mathrm{We} = \rho v^2 d/\gamma$) is an appropriate dimensionless number to address this kind of problems, since it relates the fluid's inertia and its surface tension.

In Figure 3.17, sequences of snapshots of increasing liquid flow rate are presented. For low values of the flow rate, $0 < Q_L < 10$ ml/min, a nearly spherical-shaped droplet is formed and grows with time while being attached to the nozzle (Figure 3.17(a)). At $Q_L = 10$ ml/min, the droplet remains attached to the nozzle but loses its spherical shape due to the action of inertial forces (Figure 3.17(b)). For higher liquid flow rates, $10 < Q_L \leq 15$, the primary atomization takes place with a breakup length L_b increasing with the flow rate, while the droplet mean diameters become decreased with increasing flow rate (Figure 3.17(c) to Figure 3.17(e)).

In order to study the effects of the Weber number on the breakup length L_b, we follow the procedure detailed in Bush [Bus04] and Lefebvre [Lef89].

We assume that the disturbances are axisymmetrical in the injection direction (x-direction), so the perturbed liquid surface takes the form

$$r = r_0 + \delta_0 \exp\left(qt + ikx\right) \tag{3.10}$$

where $\delta_0 \ll r_0$ is the initial amplitude of the perturbation, q is the growth rate of the instability and k is the wavenumber of the perturbation in the x-direction. Denoting by $\tilde{Z}$ the perturbed field of Z, being Z any quantity, the perturbed Navier-Stokes equations to order δ_0 and continuity become

$$\frac{\partial \tilde{v}_r}{\partial t} = -\frac{1}{\rho}\frac{\partial \tilde{p}}{\partial r}, \tag{3.11}$$

$$\frac{\partial \tilde{v}_x}{\partial t} = -\frac{1}{\rho}\frac{\partial \tilde{p}}{\partial x}, \tag{3.12}$$

$$\frac{\partial \tilde{v}_r}{\partial r} = -\frac{\tilde{v}_r}{r} - \tilde{v}_x. \tag{3.13}$$

Writing the perturbed velocities and pressure as

$$\tilde{v}_r = R(r)\exp\left(qt + ikx\right), \tag{3.14}$$

$$\tilde{v}_x = X(r)\exp\left(qt + ikx\right), \tag{3.15}$$

$$\tilde{p} = P(r)\exp\left(qt + ikx\right), \tag{3.16}$$

and substituting into Equation (3.11) through Equation (3.13), yields

$$qR = -\frac{1}{\rho}\frac{dP}{dr}, \tag{3.17}$$

$$qX = -\frac{ik}{\rho}\frac{dP}{dr}, \tag{3.18}$$

$$\frac{dX}{dr} = -\frac{X}{r} - ikx. \tag{3.19}$$

If one eliminates $X(r)$ and $P(r)$, a modified Bessel equation of order 1 is obtained for $R(r)$,

$$r^2\frac{d^2R}{dr} + r\frac{dR}{dr} - \left(1 + k^2r^2\right)R = 0. \tag{3.20}$$

Hence, the solutions must take the form

$$R(r) = CI_1(kr), \tag{3.21}$$

where $I_1(kr)$ is the modified Bessel function of the first kind and C is a constant to be determined by boundary conditions. Imposing that $\partial R/\partial t = \tilde{v}_r$, one obtains

$C = \delta_0 q \left(I_1(kr_0)\right)^{-1}$.

The normal stress balance on the free surface can be written as

$$p_0 + \tilde{p} = \gamma \nabla \cdot n, \tag{3.22}$$

where $\nabla \cdot n = \left(1/r_1 + 1/r_2\right)$, with r_1 and r_2 the principal radii of curvature of the fluid surface,

$$\frac{1}{r_1} = \left[r_0 + \delta_0 \exp\left(qt + ikx\right)\right]^{-1} \approx \frac{1}{r_0} - \frac{\delta_0}{r_0^2} \exp\left(qt + ikx\right), \tag{3.23}$$

$$\frac{1}{r_2} = \delta_0 k^2 \exp\left(qt + ikx\right). \tag{3.24}$$

Substituting and using that $p_0 = \gamma/r_0$, an equation for $\tilde{p}$ can be written

$$\tilde{p} = -\frac{\delta_0 \gamma}{r_0^2} \left(1 - k^2 r_0^2\right) \exp\left(qt + ikx\right). \tag{3.25}$$

On one hand, integrating Equation (3.17) and using Equation (3.21) and the identity $I_1(\xi) = I_0'(\xi)$, one obtains

$$P(r) = -\frac{\rho q^2 \delta_0}{k I_1(kr_0)} I_0(kr). \tag{3.26}$$

From Equation (3.16), Equation (3.25) and Equation (3.26), the dispersion relation can be finally obtained,

$$q = \left[\frac{\gamma}{\rho r_0^3} kr_0 \frac{I_1(kr_0)}{I_0(kr_0)} \left(1 - (kr_0)^2\right)\right]^{\frac{1}{2}}. \tag{3.27}$$

with a maximum growth rate of $q_{\max} = 0.34\sqrt{\gamma/\rho r_0^3}$ at $kr_0 = 0.697$. We will use this data later on.

On the other hand, at the precise moment when the perturbation has grown an amplitude equal to r_0,

$$r_0 = \delta_0 \exp(q_{\max} t_b), \tag{3.28}$$

hence

$$t_b = \frac{\ln(r_0/\delta_0)}{q_{\max}}. \tag{3.29}$$

As $t_b = L_b/v$, where v is the jet velocity,

$$L_b = \frac{v}{q_{\max}} \ln\left(\frac{r_0}{\delta_0}\right). \tag{3.30}$$

We have seen that the exponential growth rate of the fastest-growing disturbance is given by

$$q_{\max} = 0.34\sqrt{\frac{\gamma}{\rho r_0^3}} = 0.97\sqrt{\frac{\gamma}{\rho d^3}}, \tag{3.31}$$

where $d = 2r_0$. Substitution of Equation (3.31) into Equation (3.30), gives

$$\frac{L_b}{d} = 1.03\nu\left(\ln\frac{d}{2\delta_0}\right)\sqrt{\frac{\rho d}{\gamma}}. \tag{3.32}$$

Now we can rewrite Equation (3.32) in terms of the Weber number,

$$\frac{L_b}{d} = 1.03\sqrt{\mathrm{We}}\ln(d/2\delta_0). \tag{3.33}$$

Equation (3.33) is a prediction of the breakup length of a liquid jet subjected only to inertial and surface tension forces. Taking into account the effects of viscosity, Weber's analysis yields an expression of the form

$$\frac{L_b}{d} = \nu\left(\ln\frac{d}{2\delta_0}\right)\left[\sqrt{\frac{\rho d}{\gamma}} + \frac{3\mu}{\gamma}\right] \tag{3.34}$$

which may be rewritten as

$$\frac{L_b}{d} = \sqrt{\mathrm{We}}\,(1+3\mathrm{Oh})\ln\left(\frac{d}{2\delta_0}\right), \tag{3.35}$$

where

$$\mathrm{Oh} = \frac{\mu}{\sqrt{\rho\gamma d}} \tag{3.36}$$

is the Ohnesorge number. It is important to note that the breakup length L_b is proportional to $d^{3/2}$ for non-viscous fluids and proportional to d for viscous liquids.

However, the initial disturbance δ_0 cannot be determined a priori. Its value will depend on the particular experimental conditions of nozzle geometry and liquid flow rate. An empirical correlation of data for the laminar region is the following, due to Grant and Middleman [GM66]

$$\frac{L_b}{d} = 19.5\sqrt{\mathrm{We}}\,(1+3\mathrm{Oh})^{0.85}. \tag{3.37}$$

In Figure 3.18, the average breakup length $\langle L_b \rangle$ is plotted as a function of the Weber number. The average have been made over 500 frames, and the points with $\langle L_b \rangle = 0$ correspond to the non-detachment of the drop from the nozzle. An additional independent term have been added to Equation (3.37), which value have

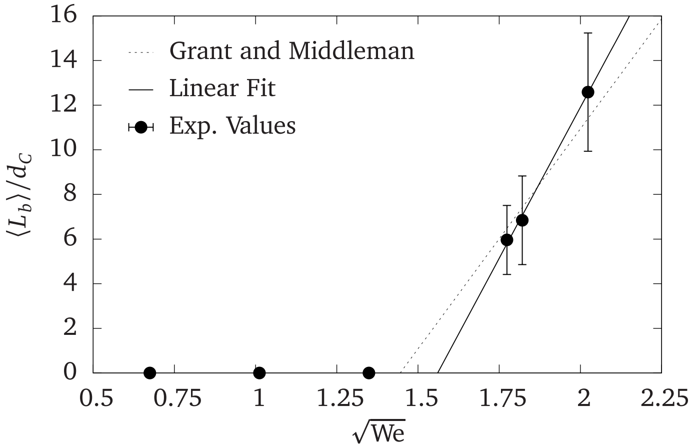

Figure 3.18: Average breakup length as a function of the square root of the Weber number. The linear fit correspond to the cases with $\langle L_b \rangle \neq 0$.

been obtained by fitting the linear relation to the experimental data points for which $L_b \neq 0$.

Comparison between the experimental data and the linear slope relation predicted by Grant and Middleman [GM66] are in acceptable agreement, despite the few experimental data points available.

In order to have an idea of the effects of gravity level on the jet breakup length, a comparison between the normal gravity case (Figure 3.13) and the microgravity case (Figure 3.18) have been carried out. In the dripping regime, the breakup length increase smoothly with the square root of the Weber number in normal gravity, while in zero gravity there is no breakup, but a single bubble growing with time. In the jetting regime, the behavior is similar in both cases (although the breakup length in zero gravity is slightly higher than in normal gravity), which reflects that in the studied range of parameters, the contribution of gravity to the inertial forces is much lower than the contribution of the liquid flow rate (jet breakup is governed by a competition between inertial forces and surface forces). From the data obtained, we conclude that a dripping regime in normal gravity leads to a growing droplet, attached to the nozzle, in microgravity, and jetting regime in normal gravity corresponds to jetting regime in microgravity.

3.2.2.2 Droplet sizes

The sizes of the droplets created by jet atomization have been measured in microgravity conditions. As in normal gravity, most of the generated droplets are oscillating, thus the introduction of the equivalent diameter d_e becomes necessary.

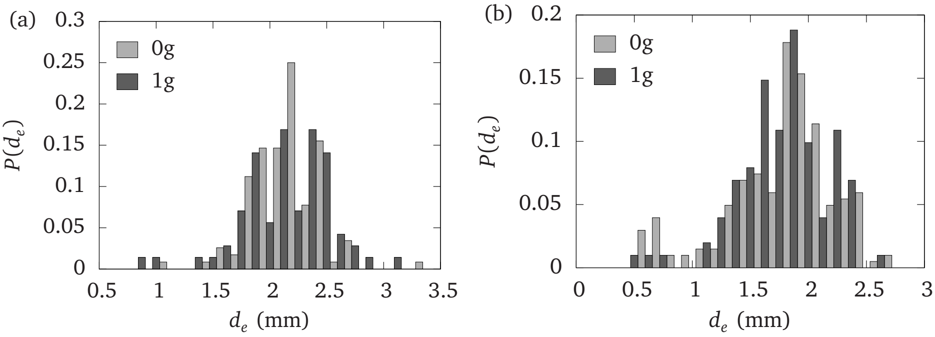

Figure 3.19: Droplet size distribution in 1g and 0g for: (a) $Q_L = 13.5$ ml/min; (b) $Q_L = 15$ ml/min.

In Figure 3.19, the droplet size distributions for $Q_L = 13.5$ ml/min (Figure 3.19(a)) and $Q_L = 15$ ml/min (Figure 3.19(b)) are presented in normal gravity and in microgravity. No significant differences are appreciated between the normal gravity and microgravity cases. This could be expected since the Bond number is low, Bo $\sim 10^{-3}$.

In addition, in the jetting regime, an increase in the liquid flow rate Q_L results in a decrease of the drop main diameter both in normal gravity and in microgravity conditions. In Figure 3.20, the droplet size distribution for different values of the liquid flow rate is presented. For $Q_L = 13.15$ ml/min, the dispersion in size of the droplets is wider than in the cases corresponding to $Q_L = 13.5$ ml/min and $Q_L = 15$ ml/min. This is due to the fact that the case of $Q_L = 13.15$ ml/min is near the transition between the jetting regime and the non-detachment regime, so the generation of droplets becomes much more unpredictable and uncontrollable.

We have seen that the maximum growth rate (Equation (3.31)) corresponds to $kr_0 = 0.697$, so the wavelength of the fastest growing disturbance is

$$\lambda = 4.51 d_C. \tag{3.38}$$

After breakup, a cylinder of length $4.51d$ becomes a spherical drop, thus

$$\frac{\pi d^2}{4} 4.51 d_C = \frac{\pi}{6} d_e^3, \tag{3.39}$$

then, $d_e = 1.89d$. However, the experimental data reveals that $2d \lessapprox d_e \lessapprox 3d$. In all cases, the values of the droplet sizes obtained experimentally are higher than the theoretical prediction (as in the normal gravity case). The disagreement between the theoretical prediction and the experimental data, is mainly due to droplet co-

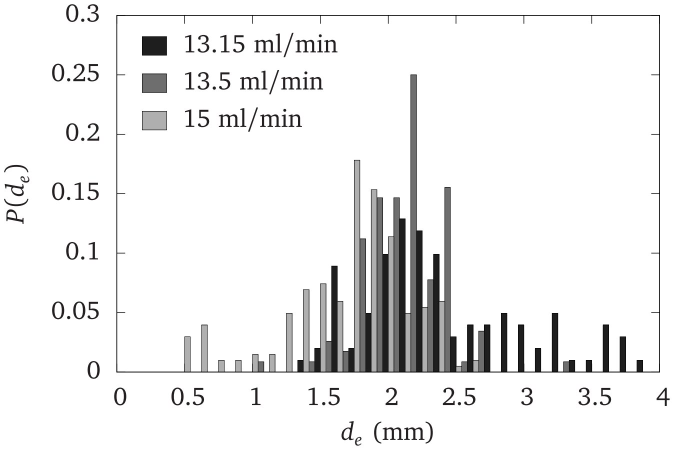

Figure 3.20: Droplet size distributions in microgravity for different liquid flow rates Q_L.

alescence events. By analyzing the videos, a large number of coalescences were observed. We also noted that the velocity of the center of a droplet after detaching from the jet was low enough to let the preceding drop collide with it. However, we must emphasize that this collision takes place due to droplet oscillations: after jet breakup, the droplets oscillate with a high amplitude. The distance between the centers of two consecutive drops may be constant, but if the droplets are oscillating in phase, this consecutive droplets may touch each other due to the high values of oscillation amplitude, giving rise to coalescence or bouncing. For this reason, the presence of the tails in the droplet size distributions in Figure 3.19 and Figure 3.20 is due to coalescence events.

3.2.2.3 Droplet trajectories

An automatized method for tracking the droplet centers evolving in time have been used. In Figure 3.21, the results of this method are presented: the x-coordinate (being x the direction of injection) of the droplet centers are plotted as a function of time, for $Q_L = 15$ ml/min. A first look at the figure shows that many of the data points are not clear or even may be wrong. This is due to the automated tracking process, in which sometimes is difficult to distinguish between surfaces when topological changes (due to ruptures and coalescences) take place. However, some important information can be extracted from this plot. On one hand, one can observe that the points are aligned in lines with a certain slope. This gives us directly a measure of the droplet velocities. On the other hand, by examining the time interval between two consecutive lines of aligned points, one can have an

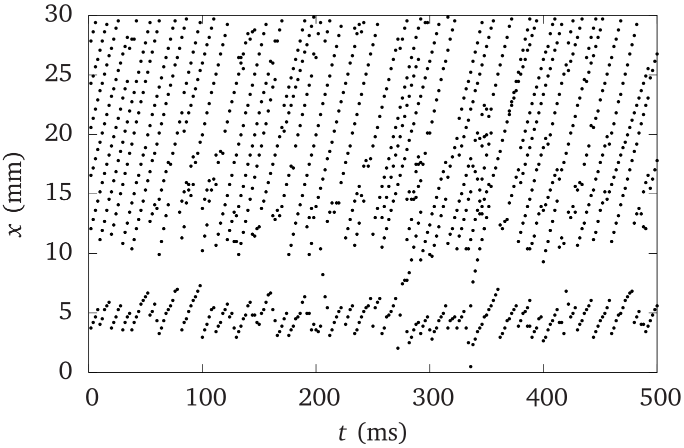

Figure 3.21: x-coordinate of the droplet centers as a function of time, for $Q_L = 15$ ml/min.

idea of the droplet generation frequency f_g, which is $f_g \approx 80$ drops/s. The white band without data points between $x = 5$ mm and $x = 10$ mm correspond to the jet breakup zone.

In Figure 3.22, an x-y map (being x the direction of injection) of the droplet trajectories for the case of $Q_L = 15$ ml/min is presented. It is important to note that the lines with highest slope do not cross the origin. This is a clear indicator that the droplets with more deflected trajectories have suffered a collision in some point after the detachment, instead of having a rectilinear trajectory coming from the nozzle. By analyzing the videos, one notes that all the droplets created after jet breakup, maintain an horizontal trajectory, following the direction of injection. The fact that the outline of all the trajectories is cone-shaped, is due to droplet collisions, most of them occurring near the jet breakup point. The droplet collision process occurs in the following way: a drop is moving horizontally, and is preceded by a slightly fastest drop with a low impact parameter different from zero. After the collision, the trajectories of these drops become deviated from the injection direction. This process is illustrated in Figure 3.23, where two droplets with impact parameter $b \neq 0$ are approaching each other since $|\vec{v}_1| > |\vec{v}_2|$. Although the initial velocities are horizontal (time t_1 in Figure 3.23), after the collision the velocities have a non-zero component perpendicular to the direction of injection (time t_3 in Figure 3.23).

After a collision, droplets can bounce or coalescence. Taking into account the relative velocity $v_{\mathrm{rel}} = v_i - v_j$ between droplets i and j prior to collision, a modified

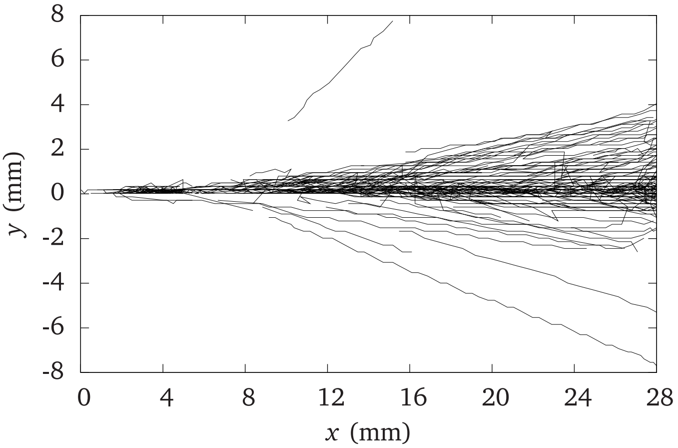

Figure 3.22: Map of droplet trajectories for $Q_L = 15$ ml/min.

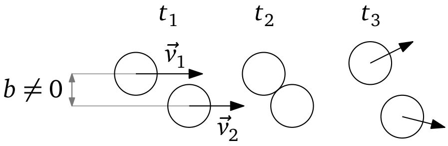

Figure 3.23: Sketch of the collision process between two droplets.

Weber number We* is introduced,

$$\text{We}^* = \frac{\rho v_{\text{rel}}^2 d^*}{\gamma}, \tag{3.40}$$

where $d^* = \sqrt{d_i d_j}$, being d_i the equivalent diameter of droplet i.

In Figure 3.24, a map of the normalized impact parameter and modified Weber number is presented. Only four values of b/d could be taken (which correspond to 0, 1, 2 and 3 pixels), due to the actual spatial resolution of the images. Despite the few data points available, one can observe a tendency of coalescences occurring at low modified Weber numbers (We$^* < 2$), while the bouncing occurring more frequently at high values of We* (We$^* > 2$). This may seem to be in contrast with the results obtained by Gao [GCPL05] and Ko [KR05] using ethanol and water droplet collisions, or the results from Chen [CC06] using diesel oil and water droplet collisions. In their work, increasing the Weber number, bouncing occurred at lower We* and coalescences at higher values (the transition between bouncing and coalescence can be found at We$^* \approx 20$). However, the values of We* that they studied ($7 <$ We$^* < 100$) were larger than in the present study, and no values below We$^* < 7$ were investigated. Furthermore, in Orme, Willis and Passandideh [Orm97, WO03, PFR06], an

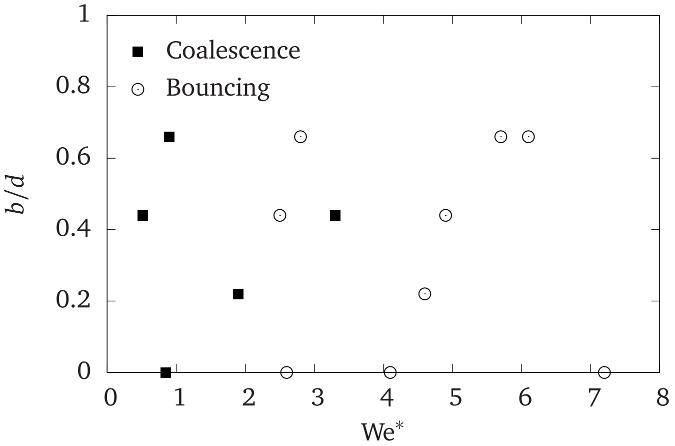

Figure 3.24: Normalized impact parameter b/d as a function of the modified Weber number.

additional regime of coalescences at low values of the modified Weber numbers is presented. For modified Weber numbers $\mathrm{We}^* < 2.9$, a regime of coalescences was also observed. From these facts, increasing the Weber number three regions can be observed: a coalescence region for $\mathrm{We}^* < 2.9$, a bouncing region for $2.9 < \mathrm{We}^* < 20$, and a coalescence region for $\mathrm{We}^* > 20$. An important point to be stated concerning Figure 3.24, is that the droplets were oscillating before the collision[8], fact that cannot be neglected since it can influence significantly the coalescence/bouncing behavior of the droplets.

3.2.2.4 Drop oscillations

Droplets oscillate with a certain frequency after jet breakup, after coalescence, or even after droplet bouncing. In the latter case, however, the amplitude of the oscillations is lower. Hence, after the creation or collision of droplets, there always exist an oscillation pattern, which in turn can lead to further collision between droplets.

The gravity force does not play any role in the droplet oscillations, the governing parameters are the surface tension, the density and the droplet diameter uniquely.

In order to analyze the oscillations of the droplets, the amplitude and frequency have been measured. In addition, the angle ϕ between the major axis of a drop and the y direction have been also measured. This angle gives information about which is the dominant mode of vibration, and the rotation of the droplets respect to its geometrical center.

---

[8] All the droplets were oscillating, however, for some droplets the oscillation amplitude was too low to be measured, due to the spatial resolution of the images.

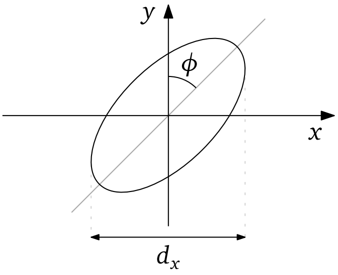

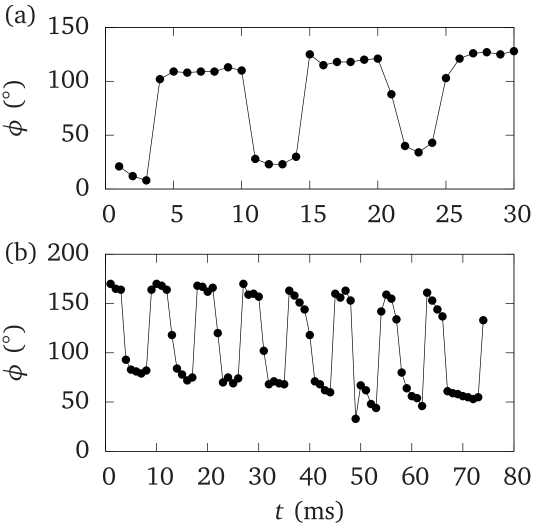

Figure 3.25: Sketch of the angle ϕ and the measured diameter d_x in the direction of injection.

Figure 3.26: Angle between the drop major axis and the y direction as a function of time. a) $d_e = 2.47$ mm, b) $d_e = 2.16$ mm.

In Figure 3.25, a schematic definition of the angle ϕ and the diameter d_x in the direction of injection are presented.

The variation of ϕ as a function of time is shown in Figure 3.26. It can be observed that the "jumps" in the angle ϕ are of 90°, which indicates that the dominant mode of oscillation is the second mode, $n = 2$. The first mode correspond to volume oscillations, while the third and fourth modes would lead to "jumps" in ϕ of 60° and 45° respectively. In addition, there is an offset in the average angle (tendency to increase in Figure 3.26(a), and tendency to decrease in Figure 3.26(b), which indicates that the droplets are rotating with respect to their centers.

The amplitude of the oscillations have been measured in order to obtain the vibration frequency and the damping time of the droplets. The obtained results are presented in Figure 3.27(a) and Figure 3.27(b) for droplet equivalent diameters of $d_e = 2.01$ mm and $d_e = 2.16$ mm respectively. One can observe that the behavior can be approximated as a damped oscillator model, i.e.

$$d_x(t) = d_e + A_2 e^{\frac{-t}{\tau}} \cos\left(\omega_2 t + \varphi\right), \tag{3.41}$$

where τ is the damping time, A_2 is the amplitude of vibration of the second mode $\omega_2 = 2\pi f_2$ is the vibration frequency of the second mode. The experimental data points have been fitted by Equation 3.41, in order to obtain the vibration frequency f_2.

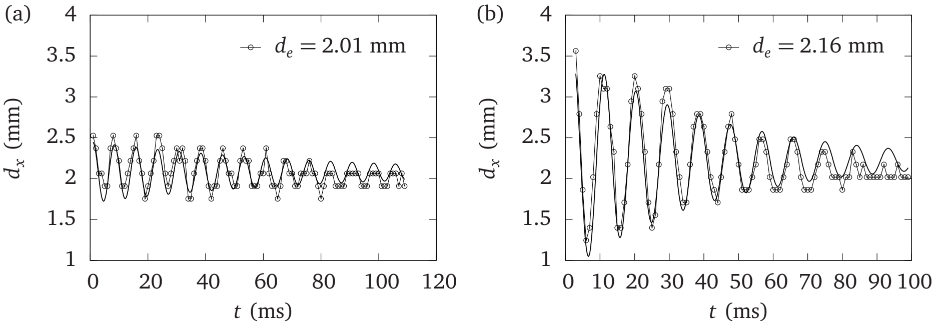

Figure 3.27: Amplitude of droplet oscillations as a function of time. Smooth lines are fits using the damped oscillator model. (a) $d_e = 2.01$ mm. (b) $d_e = 2.16$ mm.

The oscillation frequency is related to the properties of the drop by [Lam32, Lef89]

$$f_n^2 = \frac{2\gamma n(n+1)(n-1)(n+2)}{\pi^2 d_e^3 \left[\rho(n+1)+\rho_a n\right]} \tag{3.42}$$

where n is the vibration mode and ρ_a is the density of the surrounding fluid, with $\rho_a \ll \rho$. Hence, the frequency of the second mode of oscillation is given by

$$f_2 = \sqrt{\frac{48\gamma}{\pi^2 d_e^3 \left[\rho(n+1)+\rho_a n\right]}} \tag{3.43}$$

Neglecting the air density, the frequency of the second mode of oscillation can be approximated as

$$f_2 \approx \frac{4}{\pi d_e}\sqrt{\frac{\gamma}{\rho d_e}} \tag{3.44}$$

In order to obtain the oscillation frequency f_2 experimentally, which is plotted in Figure 3.28, ten oscillation periods were measured for consecutive frames, for different droplet equivalent diameters, in order to minimize the error. Excellent agreement between the theoretical prediction and the experimental values indicates that the damped oscillator model is a good approximation under the present circumstances.

3.3 Conclusions

The structure of two-phase (bubbly- and droplet-) single jets have been studied in this chapter.

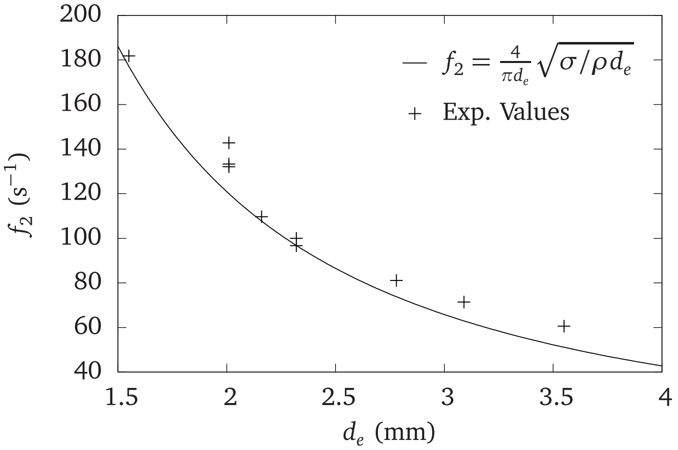

Figure 3.28: Oscillation frequency (second mode, $n = 2$) of the droplets as a function of their equivalent diameter.

For bubbly jets, the main conclusions can be summarized in the following points:

- The maximum distance reached by the bubbles from a single bubbly jet in normal gravity increases as the momentum flux is increased. A sudden increase is observed at $J \approx 10$ g cm/s^2, which reflects the transition from the dripping regime to the jetting regime.

- The bubble trajectories in normal gravity suffer a high deceleration near the nozzles, while in microgravity, the deceleration is much smoother.

- In normal gravity, the delimitation between the bubbly jet zone and the bubbly plume zone can be approximated by a straight line. The slope of this line decreases as the momentum flux increases. In microgravity, no delimitation angle can be measured since there is no bubbly plume zone, but the conical opening angle of a bubbly jet decreases as the momentum flux is increased, in a similar way as the delimitation angle does in normal gravity.

For droplet jets, the most relevant results are pointed out:

- Two different regimes have been observed within the droplet jets: the dripping regime and the jetting regime. The sizes of droplets at the dripping regime is higher than those in the jetting regime.

- The droplet mean size decreases as the liquid flow rate is increased, both in normal gravity and in microgravity.

- In zero gravity conditions, the jet breakup length increases linearly with the square root of the Weber number.
- No significant differences in droplet sizes have been observed between the normal gravity and the microgravity cases.
- The amplitude of droplet oscillations after colliding with other droplets, can be approximated by a damped oscillator model.

CHAPTER 4

Impinging jets

The structure of impinging jets is studied in this chapter. Single-phase and two-phase impinging jets are considered, and the results are presented according to the following organization: in Section 4.1.1, experimental results of impinging bubbly jets in normal gravity are presented. Section 4.1.2 deals with the experimental results of impinging bubbly jets in microgravity. Numerical results of the behavior of single-phase jets (since the jets are one-phase, the gravity level is irrelevant) are presented in Section 4.2. Finally, the numerical results of impinging bubbly jets in normal gravity and in microgravity are presented in Section 4.3.

4.1 Impinging bubbly jets

4.1.1 Impinging bubbly jets in normal gravity

4.1.1.1 Jet structure

As described in Section 3.1.1, the horizontal injection of a bubble jet in a stagnant liquid in normal gravity is characterized by the distinction between two main zones (as observed also by Lima Neto et al. [NZR08b] and Suñol et al. [SnMPGC09]). On one hand, a nearly conical jet near the injector nozzle is distinguished, in which inertial forces are predominant and bubble motion is irregular and unpredictable. On the other hand, a bubbly plume zone is obtained, in which bubbles rise steadily and the bubble paths are straight lines where buoyancy is compensated by the drag force. In this second region, inertial effects are no longer significant and bubble motion becomes predictable.

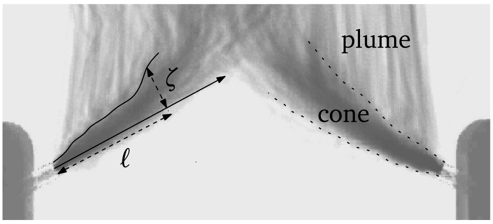

Figure 4.1: Average of 500 frames with schematic definitions of ζ and ℓ.

As a first approximation, the separation between the inertial zone and the bubbly plume zone can be considered a straight line that coincides with the aperture of the conical jet. This approximation can be applied for a single bubbly jet, as done previously by Suñol et al. [SnMPGC09]. However, when using the opposed-jet configuration, the interaction between jets modifies the global jet structure and the approximation is not applicable anymore [SnGC10a]. In this perspective, a parameter ζ is defined as the distance between the injection axis and the point where bubbles start a vertical rise. This parameter gives information about the regions where the inertial force becomes negligible. If a bubble is located above ζ, its motion is deterministic since it is rising steadily. On the contrary, if a bubble is located below ζ, the flow field is turbulent and bubble motion is mainly dominated by inertial forces. The parameter ζ is measured along the distance from the injection axis ℓ. In Figure 4.1, a graphic definition of ζ is shown.

The variation of ζ along the injection axis distance ℓ, for different values of the impact angle φ and the separation s between injectors, is presented in Figure 4.2. The behavior is almost linear in all cases, which reflects that the straight line approximation can be still considered a valid approach, specially if the interaction between the opposed jets is negligible (i.e., the cases of high separation between jets, $s = 45$ mm, and low values of the momentum flux, $J = 22\ \mathrm{g\,cm/s^2}$).

However, there can be observed a slight increase of the slope at high values of ℓ in the case $s = 25$ mm. This is due to the interaction with the incoming jet: since the distance between jets is small, the flow field generated by one of them is significantly disturbed by the other. A certain amount of bubbles coming from the opposed jet entrains to the zone of the outgoing jet, resulting in an increase of the number of bubble collisions and coalescence events in the central zone. This interaction between jets increases as the distance between them decreases, and in the case of $s = 45$ mm no considerable increase in the slope can be observed at the studied range of the momentum flux J, although is expected to occur when using higher values of J. Data corresponding to $s = 45$ mm can be measured at higher values of ℓ than data corresponding to $s = 25$ mm, because when the injectors are far from each other, the interaction zone between the two colliding jets is located far

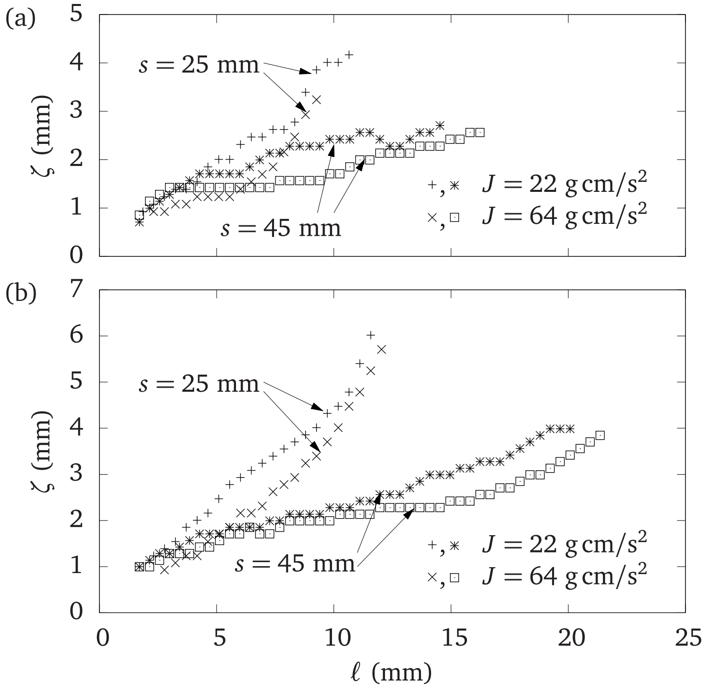

Figure 4.2: Variation of ζ with ℓ for different values of J and s. (a) $\varphi = 0°$; (b) $\varphi = 30°$.

from the outlet of the injector. It is also important to note that as J increases (with fixed values of φ and s), ζ decreases, which is related to the fact that bubbles are smaller and they leave the injector outlet at high velocities, so they can reach higher distances from the nozzle before entering the bubbly plume zone.

For some industrial applications, it can be important to know the bubble spatial distribution in the bubbly plume zone, and how it changes when the jet strength, impact angles or separation are modified. In order to determine the bubble distribution, it is appropriate to measure the horizontal position (from now on, we will call x and y coordinates the horizontal and vertical position of a certain bubble, with respect to the left injector nozzle) of the bubbles when they are rising vertically. This measurements are related to the bubble motions inside the jets, and they can reflect which is the optimal jet configuration to achieve the most uniform bubble spatial distribution.

The method used to measure the probability for a bubble to rise in a determined x coordinate, consists of performing a line profile measure of a time averaged series of consecutive frames (see Figure 4.3). The line profile measurements have been done at a height where almost all the bubbles rise vertically, and no more co-

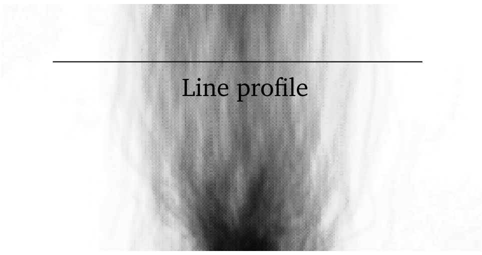

Figure 4.3: Picture illustrating the line profile measurement method.

alescences are expected to occur, so the distribution will not present considerable changes above this height. Following this procedure, a line profile measure has been carried out at a height of $h = 3$ cm from the injector outlets for a series of 1000 consecutive frames (corresponding to $\Delta t = 1$ s). Two different values of the impact angle ($\varphi = 0°$ and $\varphi = 30°$) have been considered in order to see the influence of the opposed jets orientation in the bubble spatial distribution. The data have been normalized to the number of bubbles that crossed that line to obtain the probability P_x that a bubble rise vertically in the coordinate x. The line profile measure has been done for two different values of the momentum flux ($J = 22$ g cm/s^2 and $J = 54$ g cm/s^2) and two values of the separation between injectors ($s = 25$ mm and $s = 45$ mm).

In Figures 4.4(a) and 4.4(b) the probability P_x versus the normalized distance x/s, at $\varphi = 0°$ and $\varphi = 30°$, respectively, are presented.

It can be observed that when using high values of the momentum flux J (this is, small bubbles), the probability for a bubble to rise in the central zone ($x/s \approx 0.5$) increases. In the case $s = 25$ mm and $J = 54$ g cm/s^2 the bubbles are widely dispersed in the range $x \in (0, s)$, in both orientation angles $\varphi = 0°$ and $\varphi = 30°$. At fixed values of the momentum flux J, we observe that the bubbles are more uniformly distributed at $\varphi = 0°$ than in the case $\varphi = 30°$ in both situations $s = 25$ mm and $s = 45$ mm. This fact can be explained since there is a vertical component of the mean flow field when the orientation angle is different from zero. This upwards velocity, with the help of the flow field of the opposed jet, causes the bubbles to rebound and rise in a more enclosed region. This is in agreement with the results of Tsujimoto et al. [TSSA06], who showed that the mixing efficiency of opposed jets increases at low impact angles. If the injectors are separated by $s = 45$ mm, the probability to rise in the central zone is nearly zero, especially in the case of $J = 22$ g cm/s^2, since in this case the jet strength is still not high enough to push the bubbles towards $x \approx s/2$. This is an indication that at low values of J, if the maximum distance that individual bubbles can reach along the jet axis is smaller than $s/2$, then the collisions of bubbles from different jets its not expected to occur, and no

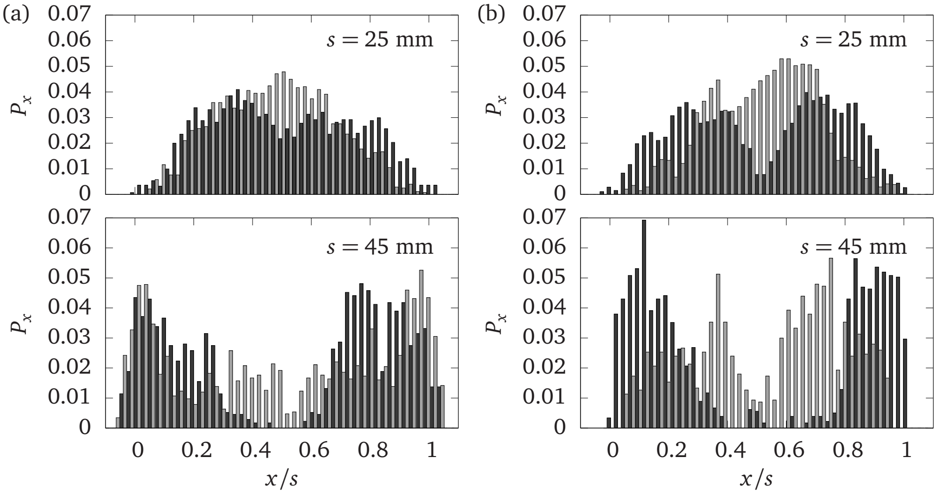

Figure 4.4: P_x versus x/s, for $J = 22\ \mathrm{g\,cm/s^2}$ (dark gray), and $J = 54\ \mathrm{g\,cm/s^2}$ (light gray). (a) $\varphi = 0°$; (b) $\varphi = 30°$.

coalescences events will be encountered in the central zone. On the other hand, when the bubbles can reach distances of the order of $s/2$ or higher, the interaction between jets becomes important and the coalescences of bubbles from different jets can take place. In this situation, the interaction between jets becomes important and the behavior of bubbles differs from that of an individual jet.

4.1.1.2 Bubble velocities

Concerning the velocity field of the bubbly jet, it is necessary to take into account the bubble velocities and the liquid flow structure. As reported by Lima Neto et al. [NZR08b], the liquid velocity field differs from the motion of bubbles at a certain distance from the nozzle. In their work, both liquid velocity field and bubble properties were examined separately. It was observed that the trajectories of the bubbles follow approximately the water jet flow in the bubbly jet region, as inertial forces are much higher than buoyancy, and after some distance from the outlet the water jet partially separates from the bubble core. This leads to the assumption that, near the outlet of the nozzle, one can consider that bubbles are moving passively through the jet without perturbing significantly the flow field, where gravity forces can be neglected. Carrera et al. [CRRP$^+$08] investigated the bubble velocities of bubbly jets in microgravity, and found that the motion of bubbles could be considered as passive tracers with respect to the carrier mean flow. To reinforce the basis of this approximation, the velocities of the bubbles at jet centerline have been measured at

$\varphi = 0°$, with two different values of the momentum flux J and different separations between injectors s. Averaging the velocities of 5 sample bubbles in each case, the variation of the velocity with the distance to the injector outlet has been obtained for $J = 22\ \mathrm{g\,cm/s^2}$ and $J = 54\ \mathrm{g\,cm/s^2}$, and is presented in Figures 4.5(a) and 4.5(b) respectively.

Following the procedure used by Carrera et al. [CRRP+08] to study the velocity of a bubbly jet in microgravity, we consider the Schlichting solution[1] [Sch79] for a single phase turbulent jet, where the x component[2] of the velocity reads

$$v_x = \frac{3}{8\pi\nu_T}\frac{J}{\rho_L}\frac{1}{\left(1+\xi^2/4\right)^2}\frac{1}{x}, \tag{4.1}$$

where ν_T is the turbulent kinematic viscosity, and

$$\xi = \frac{1}{4\nu_T}\sqrt{\frac{3J}{\pi\rho_L}}\frac{y}{x}. \tag{4.2}$$

Although some of the Reynolds numbers used in the experiments (the range of Reynolds numbers is $300 < \mathrm{Re} < 3000$) may correspond to the laminar case, the mathematical expression of the laminar and turbulent solutions for circular jets is identical, provided that the laminar kinematic viscosity ν_L is substituted by the turbulent kinematic viscosity ν_T.

To avoid the divergence at $x = 0$, a parameter x_0 is introduced in order to take into account the finite size of the nozzle. In the jet centerline, $y = 0$, the modified equation becomes:

$$v_x = \frac{3}{8\pi\nu_T}\frac{J}{\rho_L}\left(\frac{1}{x+x_0}\right) \equiv \theta(J)\frac{1}{x+x_0}. \tag{4.3}$$

The solid lines of Figures 4.5(a) and 4.5(b) correspond to a fit of the measured velocities using Equation 4.3. The values of the fitting parameters are shown in Table 4.1.

It can be observed in Figure 4.5(a), 4.5(b) that velocities corresponding to a separation between jets of $s = 25$ mm are lower than those corresponding to $s = 45$ mm. This fact can be due to the interaction with the opposing jet: when s is small the jets are closer to each other and the flow field generated by the opposed jet can decrease the mean velocity in the jet centerline. This decrease in velocity should be larger at higher values of x. In fact we can observe that when $x > 0.3s$ ($x > 14$ mm for $s = 45$ mm, and $x > 8$ mm for $s = 25$ mm), the measured velocity values are lower with respect to the fitting curves. We conclude that the presence of the

---

[1] See Appendix A.1 for a detailed analysis of the Schlichting solution for a circular turbulent jet.

[2] In this particular case, the x coordinate (horizontal direction) coincides with ℓ (injection direction).

J (g cm/s^2)	s (mm)	θ (cm^2/s)	x_0 (cm)
22	45	332 ± 33	3.1 ± 0.4
22	25	194 ± 14	1.9 ± 0.2
54	45	494 ± 29	3.3 ± 2.5
54	25	306 ± 22	1.8 ± 0.2

Table 4.1: Values of the fitting parameters θ and x_0 for opposed bubbly jets in normal gravity.

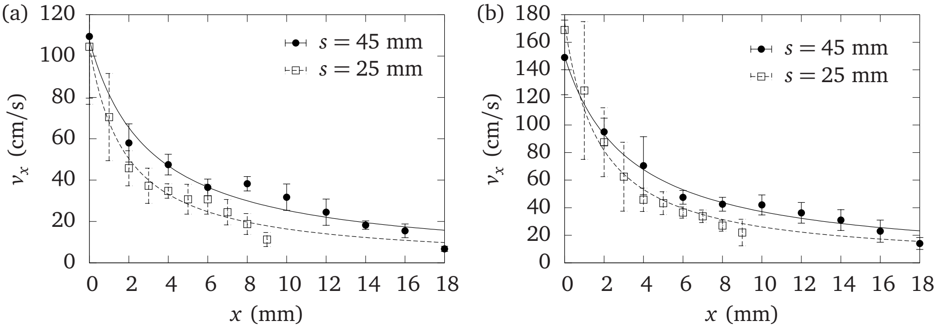

Figure 4.5: Average bubble velocity at visual jet centerline. (a) $J = 22$ g cm/s^2; (b) $J = 54$ g cm/s^2. Fitted solid lines correspond to Equation 4.3.

opposed jet decreases the average jet velocity as bubbles reach the central zone where the two jets are colliding. The interaction between jets is thus not negligible and the velocity field can only be compared with that of a single injector at low values of x.

Except for a velocity scale, the structure of the turbulent liquid jet solution is independent of J. Consequently, all the velocity measurements of Figures 4.5(a) and 4.5(b) should collapse on a single curve. In Figure 4.6, we show a good fit of the measurements to the Schlichting solution, which confirms the validity of considering bubbles as passive tracers near the nozzles.

4.1.1.3 Bubble sizes and coalescence events

In order to predict the bubble size distribution, one could consider the population balance method [Ram00], which writes

$$\frac{\partial}{\partial t} n + \vec{\nabla} \cdot \left(\vec{v}_B n\right) + \frac{\partial}{\partial d_B} \left(n \frac{\partial d_B}{\partial t} \right) = S, \tag{4.4}$$

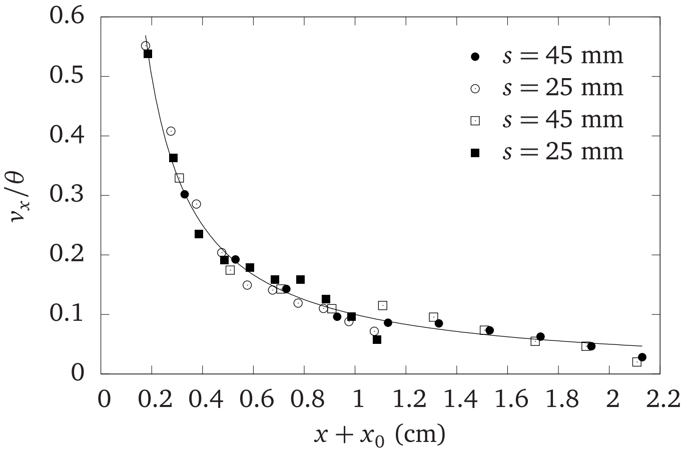

Figure 4.6: Collapse of bubble velocity measurements. Circles and squares correspond to $J = 54\ \mathrm{g\,cm/s^2}$ and $J = 22\ \mathrm{g\,cm/s^2}$, respectively. Solid line correspond to a fit by Equation 4.3.

where $n(\vec{x}, d_B, t)$ is the local number density, d_B is the bubble diameter, $\vec{v}_B(\vec{x}, d_B, t)$ is the bubble velocity and S is the source term, due to coalescence or breakup events.

It is convenient to divide the bubble sizes into N classes, so the population balance equation for the ith bubble class becomes

$$\frac{\partial}{\partial t} n_i + \vec{\nabla} \cdot \left(\vec{v}_B n_i\right) = S_i, \tag{4.5}$$

where the growth term have been neglected. In the above equation, n_i is the ith bubble class local number density and S_i is the source term for the ith bubble class. No bubble breakup has been observed in the recorded videos. Thus, if we only take into account the coalescence events, the source term for the ith bubble class writes [PMBZ01]:

$$S_i = \frac{1}{2} \sum_{k=1}^{N} \sum_{\ell=1}^{N} C_{i,k\ell} - \sum_{j=1}^{N} C_{ij}, \tag{4.6}$$

where $C_{i,k\ell}$ is the creation of a ith class bubble from coalescence between smaller bubbles from classes k and ℓ,

$$C_{i,k\ell} = \begin{cases} C_{kl} & \text{if} \quad V_k + V_\ell = V_i, \\ 0 & \text{if} \quad V_k + V_\ell \neq V_i. \end{cases} \tag{4.7}$$

Here, V_i is the volume of a ith class bubble, and C_{ij} is the coalescence rate, which is usually defined as the product between the collision frequency θ_{ij} and the coalescence efficiency P_{ij},

$$C_{ij} = \theta_{ij} P_{ij}. \tag{4.8}$$

Modelling of θ_{ij} and P_{ij} gives the evolution of the bubble size distribution in terms of the fluid properties, and solving Equation 4.5 one obtains the evolution of the bubble size distribution (see [LEG87, PB90, Che91, LS96, KCCF01, LMM02] for a detailed description of the available models).

When a steady-state region is attained, Equation 4.5 becomes

$$\vec{\nabla} \cdot (\vec{v}_B n_i) = S_i = 0. \tag{4.9}$$

In these conditions, a log-normal distribution can describe the considered bubble size distribution [Var95, KCCF01, PMBZ01, CRF08]

$$P(d_B; \mu, \sigma) = \frac{1}{d_B \sigma \sqrt{2\pi}} \exp\left(-\frac{\left(\ln(d_B/d_C) - \mu\right)^2}{2\sigma^2} \right), \tag{4.10}$$

where μ and σ are fitting parameters.

With the aim to know what is the order of magnitude of the bubble sizes we are dealing with, the diameters d_B of approximately 1000 bubbles have been obtained for two values of the momentum flux J. These diameters have been measured from 10 sample frames, with an automatic count of around 100 bubbles in each frame. Figure 4.7 presents an histogram with the obtained results, where it can be seen that the sizes of the bubbles are in the same order of magnitude as the capillary diameter.

The fitting values for $J = 22$ g cm/s^2 are $\mu = 0.03 \pm 0.04$ and $\sigma = 0.57 \pm 0.03$ and for $J = 64$ g cm/s^2 are $\mu = -0.28 \pm 0.05$ and $\sigma = 0.56 \pm 0.04$.

The dispersion in size of the bubbles is due to two facts: first, and most important, are the coalescence events. With the flow rates that have been used, multiple coalescences were observed in some bubbles, and this is the reason for the presence of this long tail in the diameter distribution. Second, is the fact that the injector has a little dispersion in the sizes of the bubbles generated, and this dispersion increases when high values of J are studied. This phenomenon is the reason why there are bubble diameters smaller than the capillary diameter, since no bubble breakups have been observed. It can be seen in Figure 4.7 that the bubble diameters are smaller when $J = 64$ g cm/s^2, which is due to the higher amount of liquid flow rate used. In the studied range of injector operation, for any value of the liquid flow rate Q_L using low values of the gas flow rate Q_G, an increase of the gas flow rate results in an increase of the bubble generation frequency, and not on the bubble sizes. When the gas flow rate is higher than a certain critical value[3], the generation frequency saturates and increasing Q_G leads to higher bubble diameters, as reported in Arias

---

[3] About 10 ml/min for an injector of 1 mm diameter and $Q_L = 20$ ml/min.

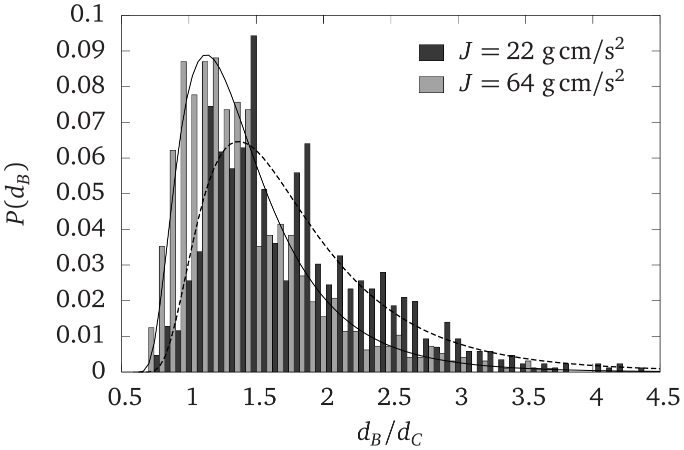

Figure 4.7: Distribution of bubble diameters at $J = 22$ g cm/s^2 and $J = 64$ g cm/s^2. Dashed and solid lines correspond to a fit by a log-normal distribution (Equation 4.10) to the $J = 22$ g cm/s^2 and $J = 64$ g cm/s^2 cases respectively.

et al., [ARC$^+$09]. The measured bubble size distribution is very similar to that obtained photographically by Varely [Var95], although the sizes of the bubbles studied in his work ranged from 0.2 mm to 1 mm. Bubbly jets with mean bubble diameters between 1 mm and 5 mm were studied by Lima Neto et al. [NZR08a, NZR08b] and they also obtained a similar shape of the size distribution. Kamp et al. [KCCF01] investigated the size of bubbles in bubbly flows through pipes (with bubble mean diameters ranging from 2 mm to 20 mm) and found distributions close to the present one, but with no such long tails due to the coalescence events, which occur very frequently after the bubbles have left the pipes creating therefore the bubbly jet.

It is possible that bubbles experience an expansion upon release into the tank due to pressure difference between capillary pressure and the tank pressure, which were not measured. In any case, since all bubbles have similar sizes (for fixed Q_L and Q_G), this expansion would be similar for all of them, and thus the peak in Figure 4.7 would probably be slightly shifted to the right.

The CO$_2$ solubility in water could become an important factor in the bubble diameter determination. However, we have neglected the effects of solubility in the bubble size, since according to Epstein et al. [EP50] and Ljunggren et al. [LE97], the lifetime of a CO$_2$ bubble of 1 mm diameter in water at the present experimental conditions is of the order of several hours. Although the experiment runs for some minutes (between 2 and 5 minutes to ensure a steady state) before recording the high-speed sequence, a negligible amount of CO$_2$ is dissolved in water during this time. Moreover, the bubble diameter does not experience any significant change during the time interval (approximately 50 ms) in which the bubble enters the zone

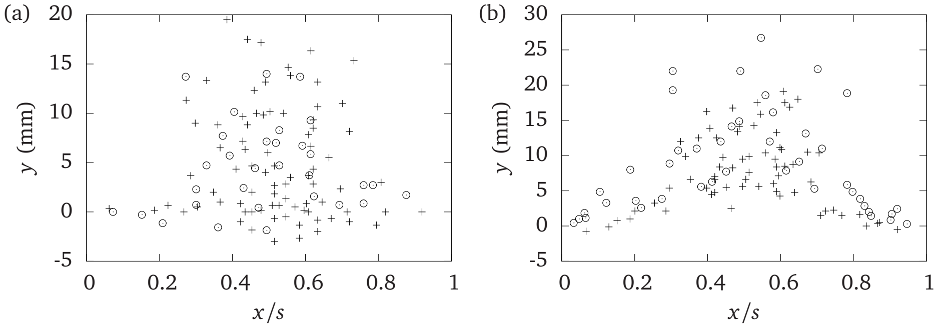

Figure 4.8: Position of coalescence events in $\Delta t = 0.2$ s, for $J = 54$ g cm/s^2. Circles and crosses correspond to $s = 45$ mm and $s = 25$ mm respectively. (a) $\varphi = 0°$; (b) $\varphi = 30°$.

of observation and exits it. Thus, we consider that the concentration of CO_2 in water is steady in a time interval of 50 ms, which does not affect to the bubble diameter.

In order to have an image of the regions in the bubbly jets where the coalescence events take place, we have measured the (x, y) coordinates of such events that took place in $\Delta t = 0.2$ seconds. Figures 4.8(a) and 4.8(b) show the positions of the coalescences that occurred for $J = 54$ g cm/s^2 with two values of the separation s and with $\varphi = 0°$ and $\varphi = 30°$, respectively. When $\varphi = 0°$ (Figure 4.8(a)) and $s = 45$ mm, the coalescence locations are more or less uniformly dispersed, while in the case $s = 25$ mm the coalescence events occur more frequently and appear to be more concentrated in the central zone. This could be expected since the jet strength combined with the incoming flow of the opposed jet is forcing a high number of bubbles to collide.

It is important to note that some of the coalescence events occur near the injector outlet (see, for example, Figure 4.8(b)). This fact, also observed by Carrera et al. [CRRP$^+$08] using a single bubbly jet in microgravity, is due to a sudden decrease of velocity observed in some bubbles: when they have just detached from the nozzle they slow down drastically very quickly. This decrease in velocity facilitates the impact of the following bubble with the slow bubble, creating a larger bubble that, in turn, is more capable to coalesce since its size is larger and presents a higher cross section. From the movies recorded it is easy to see that when using high values of the gas flow rate Q_G and low values of the liquid flow rate Q_L (thus resulting a low value of the momentum flux J), the majority of the coalescence events occur just at the outlet of the nozzle. These coalescences are produced by bubbles from the same jet, since for low momentum fluxes bubbles are much higher in size and consequently slower. Only a small amount of coalescences are produced by bubbles coming from different jets, since bubble approach relative velocity is higher, and they take place

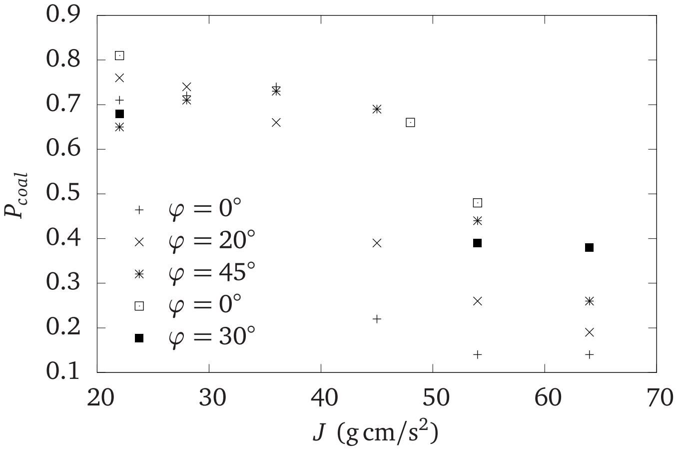

Figure 4.9: Coalescence probability vs. J, at different angles φ and separations s. For the squares, $s = 25$ mm. For the rest, $s = 45$ mm.

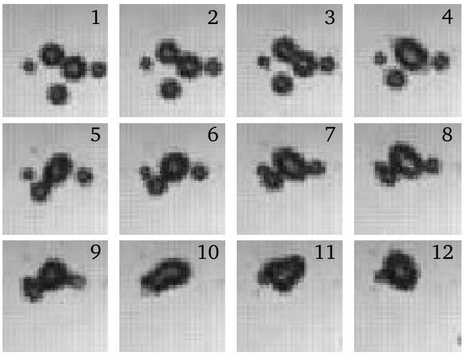

Figure 4.10: Sequence of snapshots showing the coalescence process of four bubbles into a single daughter bubble.

in the central region where the opposed jets are colliding.

Finally, the coalescence probability P_{coal} versus J has been studied at different orientation angles φ and separations s. The measurements have been carried out manually by following the bubbles individually frame by frame, counting the number of bubbles generated by the injectors and the number of coalescence events in a time interval of $\Delta t = 0.2$ s.

It can be observed in Figure 4.9 that at low values of the momentum flux J, the number of coalescences is really high (nearly 70% of bubbles coalesce). This can be explained since the size of the generated bubbles is larger for low values of J, and larger bubbles suffer a decrease in their velocity just when they are in the outlet of the nozzle. A large bubble moving slowly near the injector increases the probability to collide with the following bubble, and when this collision occurs, the size of the daughter bubble is even bigger increasing even more the coalescence probability. On the other hand, using high values of J the bubbles are smaller and they are injected at high velocities (around 100 cm/s), so the probability to collide with the following bubble is reduced drastically. The probability of coalescence at high values of J is still large, due to the fact that high speed bubbles tend to collide with the bubbles of the incoming jet rather than with the preceding bubbles of the same jet. To clarify the ideas considered when creating the plot in Figure 4.9, it should be noted that the coalescence probability has been measured considering that a coalescence is the collision of two bubbles creating a single larger daughter bubble, no matter if the coalescing bubbles have suffered any previous coalescences before. In fact, many bubbles can suffer coalescence more than once. An example of this is presented in Figure 4.10, where a sequence of images with four bubbles coalescing into one large bubble (the smallest bubble do not coalesce) is shown. Four bubbles that coalesce into a single one, means that three coalescence events have been occurred using the definition already explained. The time interval between consecutive snapshots presented in Figure 4.10 is 1 ms, meaning that the whole process takes place in 12 ms. The size of each snapshot is 42x43 pixels, corresponding to 6x6 mm approximately.

4.1.1.4 Comparison between distilled water and ethanol

An additional set of experiments were carried out using ethanol as a carrier liquid with the aim to be aware of possible substantial differences when using different viscosity and surface tension [SnGC11].

Velocity of bubbles has been measured from the movies recorded for different values of the momentum flux and separation distance. Measurements have been done in the jet centerline, near the injector nozzle, using a horizontal injection configuration (0° impact angle) in distilled water and ethanol. In Figure 4.11, the obtained results are presented. It should be emphasized that the velocity field can only be compared to that of a single jet at low values of x, that is, near the nozzle where the interaction with the incoming jet is still negligible, inertia is highly predominant and bubble motion can be considered passive, so the bubbles are carried away by the liquid. However, at high values of x, the measured velocities are slightly lower than the theoretical prediction (Equation 4.3). Such decrease in velocity near the central zone is observed both in distilled water and in ethanol. This can be due to the fact that the opposed jet is perturbing the velocity field far from the injector nozzle, changing bubble velocities to lower values near the impingement zone (high values of x).

In order to obtain the bubble size distribution experimentally, the diameters d_B of approximately 1000 bubbles have been measured for different values of the momen-

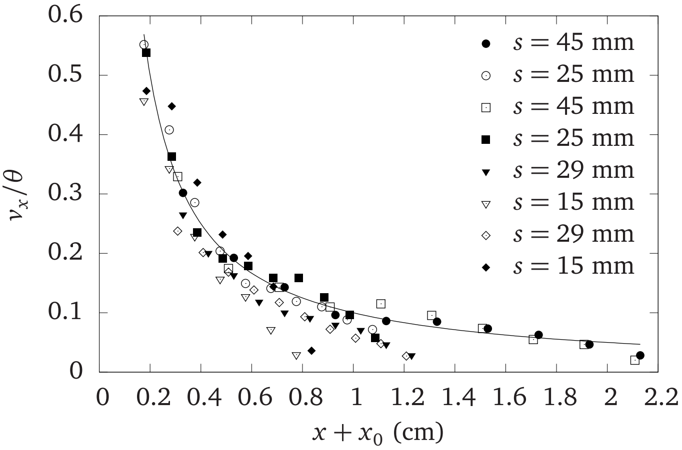

Figure 4.11: v_x/θ as a function of $x + x_0$ for distilled water (circles and squares) and ethanol (triangles and diamonds). Circles, squares, triangles and diamonds correspond to $J = 54$ g cm/s^2, $J = 22$ g cm/s^2, $J = 60$ g cm/s^2 and $J = 20$ g cm/s^2 respectively. Solid line correspond to a fit by Equation 4.3.

tum flux J. Measurements have been carried out using an image processing software from 10 sample frames with an automatic count of around 100 bubbles each frame. The probability of a bubble to have a certain size has been obtained dividing the number of bubbles in a size range, by the total number of bubbles counted. In Figure 4.12, bubble size distributions are presented for two values of the momentum flux in distilled water and ethanol. Log-normal distributions are fitted to the data. The fitting parameters in Figure 4.12(a) are $\mu = 0.18 \pm 0.15$ and $\sigma = 0.42 \pm 0.06$ for ethanol and $\mu = 0.58 \pm 0.02$ and $\sigma = 0.57 \pm 0.03$ for distilled water. In Figure 4.12(b), the fitting parameters are $\mu = 0.35 \pm 0.06$ and $\sigma = 0.47 \pm 0.04$ for ethanol and $\mu = 0.54 \pm 0.04$ and $\sigma = 0.56 \pm 0.04$ for distilled water.

In all cases the majority of the bubbles have a size slightly higher than the capillary diameter. Coalescence events are the main responsible of the dispersion in size, creating a large tail in the bubble size distribution. More coalescence events have been observed in ethanol, and the bubble size distribution is thus slightly wider than in the case of distilled water.

It is important to remind that larger values of the momentum flux correspond to bubbles with smaller diameters. This comes from the difference between gas and liquid densities (Equation 3.3). Variations of Q_L have a much stronger effect on the value of J than same variations of Q_G. Thus, large values of J corresponds to large Q_L, which generate smaller bubbles for a fixed value of Q_G. On the contrary, for the range of flow rates used, increasing Q_G gives rise to a large bubble generation frequency, not inducing any changes in the bubble size (see the linear regime in

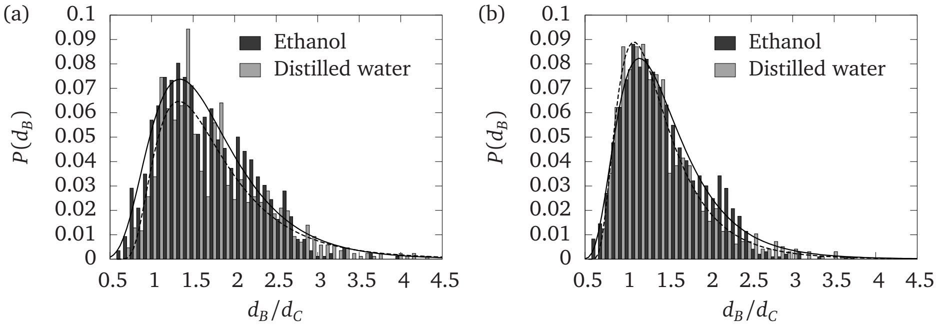

Figure 4.12: (a) Histogram of bubble diameters for $J = 22\ \mathrm{g\,cm/s^2}$ in distilled water, and $J = 20\ \mathrm{g\,cm/s^2}$ in ethanol. (b) Histogram of bubble diameters for $J = 64\ \mathrm{g\,cm/s^2}$ in distilled water, and $J = 60\ \mathrm{g\,cm/s^2}$ in ethanol. Solid and dashed lines correspond to a fit by a log-normal distribution for ethanol and water, respectively.

Figure 2 of Arias et al. [ARC$^+$09], and Figure 3 of Arias et al. [AGCR$^+$10]).

The obtained bubble size distributions are very similar to that obtained by Varely [Var95]. In his work, smaller bubbles (sizes ranging from 0.2 mm up to 1 mm) were created using larger values of the liquid flow rate. Bubbly jets with mean bubble diameters between 1 mm and 5 mm were studied by Lima Neto et al. [NZR08a, NZR08b], obtaining similar size distributions. Kamp et al. [KCCF01] also obtained similar distributions, investigating the size of bubbles in bubbly flows inside pipes (with bubble mean diameter ranging from 2 mm up to 20 mm). However, they did not observe such long tails due to the coalescence events, which occur most frequently after the bubbles have left the pipes creating therefore the bubbly jet.

4.1.2 Impinging bubbly jets in microgravity

Snapshots of impinging bubbly jets in microgravity are presented in Figure 4.13 for a momentum flux of $J = 86\ \mathrm{g\,cm/s^2}$. Pictures were taken at $t = 325$ ms, $t = 700$ ms, $t = 1100$ ms and $t = 1200$ ms after the release of the drop capsule. The first thing that one can observe is the presence of three big bubbles. These bubbles are not created by the bubble generation mechanism described in Section 2.1.1. Instead, these bubbles were present at the capsule release instant. Due to the fact that negative gravity values are reached when dropping the capsule (up to $g = -0.7g_0$, see Figure 3.7(a)), some of the gas that is present in the top of the test tank[4] is directed to the

---

[4] The test tank is designed with its top part forming an angle of 5°, so the bubbles coming from the jets in normal gravity are directed to the residual tank through a capillary tube. However, this system is not efficient enough to remove the gas inside the test tank at the moment of capsule release, and some big bubbles are still present in the top of the test tank.

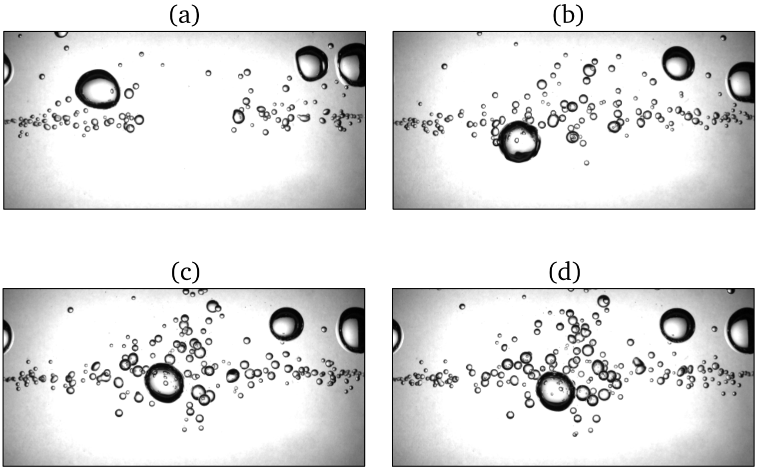

Figure 4.13: Snapshots of impinging bubbly jets in microgravity at different times, for $J = 86$ g cm/s^2. (a) $t = 325$ ms, (b) $t = 700$ ms, (c) $t = 1100$ ms and (d) $t = 1200$ ms after capsule release.

bulk of the test tank, not staying at the top anymore. If a bubble reaches the jet zone (as the bubble on the left), it is pushed by the liquid flow field to the central zone. Once the bubble reaches the central zone of the test tank, it is difficult to escape from this region due to the higher pressure generated by the opposed jets.

The presence of big bubbles coming from the top of the tank occurred in all the 5 drops we had available at the ZARM Drop Tower. These bubbles affect the flow field significantly, and the results reported herein are taken in a way that tries to minimize those perturbations: the measurement of the jet shape or bubble velocities was carried out when the big bubbles were located far from the jet region. In addition, in the measurements of the bubble sizes, the diameters of these big bubbles (and the smaller bubbles surrounding the big ones in some cases) have been neglected.

4.1.2.1 Jet structure

With the absence of buoyancy force, the distinction between the inertial zone and the bubbly plume zone is not valid anymore. However, assuming that in microgravity the bubbles can be considered as passive tracers of the carrier jet, the position of the bubbles inside the jet give valuable information of the global jet structure. By examining visually the recorded movies, one observes that the paths of the bubbles were confined at certain regions (the majority of the bubble positions lie inside a nearly conical shape with its edge located at the nozzle exit), being the velocity of the bubbles higher at the jet centerline. By averaging a certain number of frames of every movie, a delimitation of the conical jet structure was pointed out. The vast

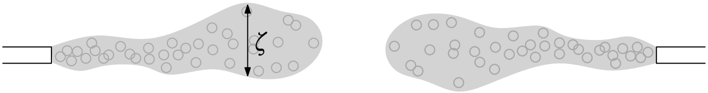

Figure 4.14: Schematic definition of ζ.

majority of the bubble paths are confined in a region which describe the jet conical shape. Only a small number of bubbles are located outside this shape.

With the aim to characterize this shape (which can no longer be described by a cone opening angle –i.e. a straight line– due to the presence of the opposed jet), a parameter ζ is defined[5] as the position of the delimiting zone of the jet shape, measured directly from the averaged images. A schematic definition of ζ is presented in Figure 4.14.

A plot of ζ as a function of the injection axis position is presented in Figure 4.15. In this particular case, the separation between jets is $s = 10$ cm, and the momentum flux is $J = 86\,\mathrm{g\,cm/s^2}$. The values of ζ have been obtained by averaging the first 400 ms (squares), 650 ms (circles) and 1760 ms (triangles) respectively[6] and drawing visually the delimitation zone. In the case of $t = 400$ ms, the bubbles can be located inside two regions with a nearly conical shape emerging from the nozzles. The bubbles coming from the opposed jets are still in its way to the central zone (which correspond to $40 < \ell < 60$ in this case approximately). At $t = 650$ ms, the bubbles coming from one jet are interacting with bubbles coming from the opposed jet in the central zone, reducing its velocity in the jet centerline direction while increasing its velocity in the direction perpendicular to the injection direction. Finally, at $t = 1760$ ms, the interaction between the opposed jets is highly significant in the central zone, fact that is reflected for the bubble paths: near the central zone, the velocity of the bubbles in the direction of injection becomes reduced. However, the velocity in the direction perpendicular to injection increases. This results in a cross-like shape of the interacting jets, demonstrating that the assumption of the straight conical shape (assumption taken with a single jet) is no longer valid, being only applicable in the region close to the nozzle.

4.1.2.2 Bubble velocities

In order to determine the bubble velocity distribution at the jet centerline, velocities of representative bubbles have been measured at different momentum fluxes and separation distances between opposed jets.

---

[5] The symbol ζ was used in Section 4.1.1 as the parameter which describe the delimitation zone between inertial and buoyancy regions in normal gravity. The same symbol ζ is used foreword because it also characterizes the delimitation of the jet, although its natural definition is different from that of Section 4.1.1.

[6] Considering $t = 0$ ms as the time of the capsule release.

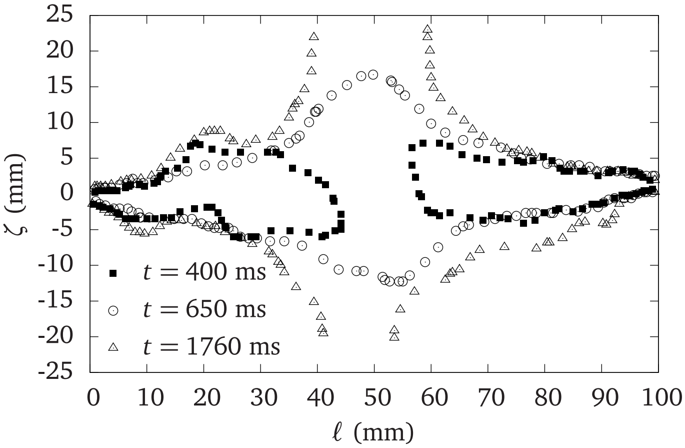

Figure 4.15: Delimitation parameter ζ as a function of the injection axis position, for $J = 86\ \mathrm{g\,cm/s^2}$.

In Figure 4.16(a), the component of the velocity in the direction of injection is plotted as a function of the distance from the nozzle, for a fixed separation between nozzles of $s = 10$ cm. It can be observed that for $x > 30$ mm, the measured velocities are lower than the Sclichting's theoretical prediction, Equations 4.1 and 4.2 (fitted solid lines). This prediction is for a single jet, and the presence of the opposed clearly perturbs the velocity field at the central zone (for $s = 10$ cm, the central zone can be considered $30 < x < 70$ cm approximately). Contrarily to a single jet, the velocity field of opposed jets have a cross-like shape, with a high reduction of v_x in the central zone, and with an increment of v_y in the collision plane (at $x = s/2$). The bubbles enter the collision zone with values of the velocity component in direction of injection (v_x) much higher than the perpendicular component (v_y). After the collision with the incoming jet, a circular "sheet" of bubbles grows radially from the center of the collision zone, being in this region v_y much higher than v_x.

The velocities for different separations between jets are plotted in Figure 4.16(b). In this figure it can be also observed the same behavior: measured velocities are lower in the central zone than the theoretical prediction. Thus we conclude that the prediction of Equation 4.3 can be only applied near the nozzles of the opposed jets, due to the perturbation of the velocity field created by the incoming jet.

The values of the fitting parameters to the Schlichting solution from Figures 4.16(a) and 4.16(b) are presented in Table 4.2.

Comparing the normal gravity (Figure 4.5) with the microgravity case (Figure 4.16), a similar behavior of the bubbles velocities at the jet centerline is observed. However, in the normal gravity case, the bubbles suffer a high deceleration just after leaving the nozzle, while in zero gravity the deceleration is smoother. As a result, the

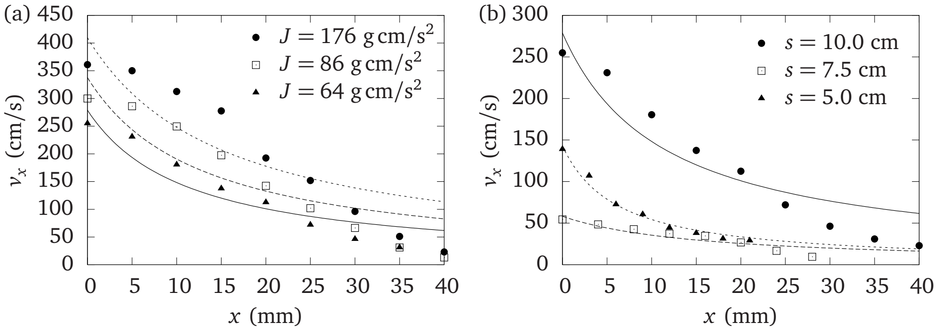

Figure 4.16: Bubble velocities at visual jet centerline. (a) $s = 10$ cm; (b) $J = 64$ g cm/s^2 for $s = 10$ cm, $J = 1.8$ g cm/s^2 for $s = 7.5$ cm and $J = 16$ g cm/s^2 for $s = 5$ cm. Fitted solid lines correspond to Equation 4.3.

J (g cm/s^2)	s (mm)	θ (cm^2/s)	x_0 (cm)
176	10	6285 ± 1780	15 ± 5
86	10	4382 ± 1200	13.0 ± 4.7
64	10	3167 ± 674	11.3 ± 3.2
16	5	911 ± 203	15.6 ± 4.6
1.8	7.5	875 ± 69	6.1 ± 0.6

Table 4.2: Values of the fitting parameters θ and x_0 for opposed bubbly jets in microgravity.

velocities observed experimentally in microgravity are higher than the Sclichting's theoretical prediction in a small region near the nozzle ($5 < x < 15$ mm), and lower than the theoretical prediction at large distances from the nozzle ($x > 25$ mm) due to the presence of the incoming jet.

As mentioned previously in Section 4.1.1, the structure of the turbulent jet solution is independent of the momentum flux J and consequently all the measurements of Figures 4.16(a) and 4.16(b) should collapse on a single curve. In Figure 4.17, a plot of this collapse is presented. Good fit of the Schlichting solution to the measured velocities is obtained near the nozzle. Far from the nozzle, the measured velocities are lower than the prediction due to the presence of the opposed jet. Hence, the affirmation that the Schlichting solution for a single jet can be only applied near the nozzles, where the perturbation of the incoming jet can still be neglected, is confirmed.

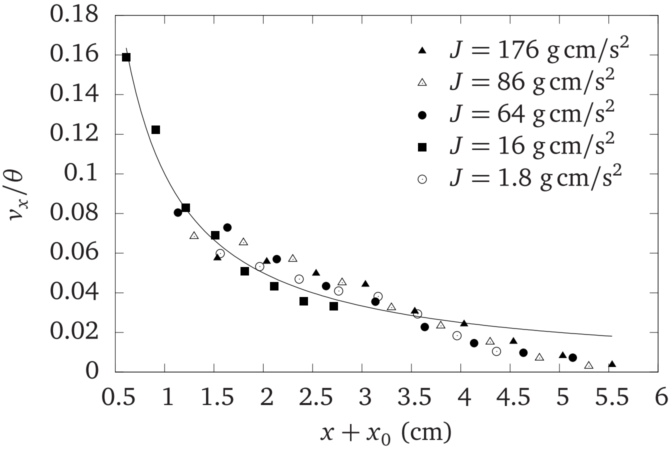

Figure 4.17: Collapse of bubble velocity measurements in microgravity, for different momentum fluxes and separation distances.

4.1.2.3 Bubble sizes and coalescence events

Unlike with bubbly jets in normal gravity, the bubbly jets in microgravity evolve continuously with time and no steady states are reached. In normal gravity, all the bubbles that the injector generate are quickly directed to the top of the tank due to buoyancy forces. However, in microgravity, an injected bubble could stay at the same position inside the tank for an indefinite period of time, being able to collide and coalesce with another bubble. Hence, the number of bubbles of bubbly jets in microgravity grows with time, increasing therefore the number of coalescence events. For this reason, the bubble size distribution of the bubbly jets in microgravity also evolves in time, and can not be considered steady anymore.

The sizes of the bubbles for different momentum fluxes have been measured from a snapshot of the movies at $t = 300$ ms after capsule release, and the obtained bubble size distribution is presented in Figure 4.18(a). The number of measurements is of the order of 100 bubbles for each snapshot. The presence of big bubbles coming from the top of the test tank (see Figure 4.13) have been neglected in the measurement of the bubble size distribution. Since no bubble breakup have been observed, the presence of bubbles with diameters smaller than capillary diameter $d_B < d_C$ is due to the injector performance, and to the depth of field effect. On the other hand, the presence of bubbles with diameters $d_B > d_C$ is due to the injector performance and the coalescence events. First, it is important to point out that the injector generates bubbles with a certain bubble size distribution, being some bubbles slightly smaller than the capillary diameter and some bubbles slightly larger. Secondly, by observing the recorded movies we deduce that the width of the bubble

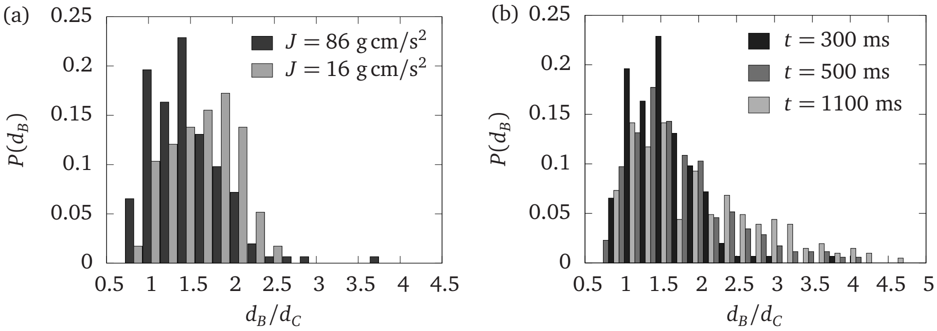

Figure 4.18: Distribution of bubble diameters for: (a) different momentum fluxes at a fixed time; (b) different times at a fixed momentum flux.

size distribution from the injector is small, so the presence of bubbles with diameters $d_B/d_C > 1.5$, is due uniquely to coalescence events. The mean diameter is higher for the lower value of the momentum flux, due to the fact that higher values of the momentum flux are obtained by high values of the liquid flow rate, as explained in Section 4.1.1.

Since the bubble size distribution of bubbly jets in microgravity evolves in time, bubble diameters have been measured for a fixed value of momentum flux and separation distance at three different times. In Figure 4.18(b), the obtained bubble size distribution is presented. The number of measurements is approximately 100 bubbles for $t = 300$ ms and 200 for $t = 1100$ ms. It can be observed that the bubble mean diameter grows in time, since a lot of coalescence events were observed with no bubble breakups. This growth in the bubble diameter is due uniquely to the growth of the tail of the distribution, not in an offset of the whole distribution. This offset could be created by a change in the injector performance, which was observed to be steady, so the evolution in bubbles sizes is due exclusively to coalescence events. In both Figures 4.18(a) and 4.18(b), the tail of the bubble size distribution is a direct measure of the coalescences, since no bubbles with $d_B/d_C > 1.5$ were observed coming out from the nozzle.

With the aim to know in which regions of the opposed jet configuration the coalescence events take place, a manual measurement of the (x, y) coordinates of the coalescences occurring in $\Delta t = 200$ ms have been carried out. The position of coalescence events have been measured manually form the movies recorded by skipping frame by frame and annotating the position where coalescences were observed. The obtained results for $s = 10$ cm and $s = 5$ cm are plotted in Figures 4.19(a) and 4.19(b) respectively. From these plots, we observe that the coalescences can occur in the whole width of the jet, but most of the coalescence events tanking place near the nozzles or in the central zone.

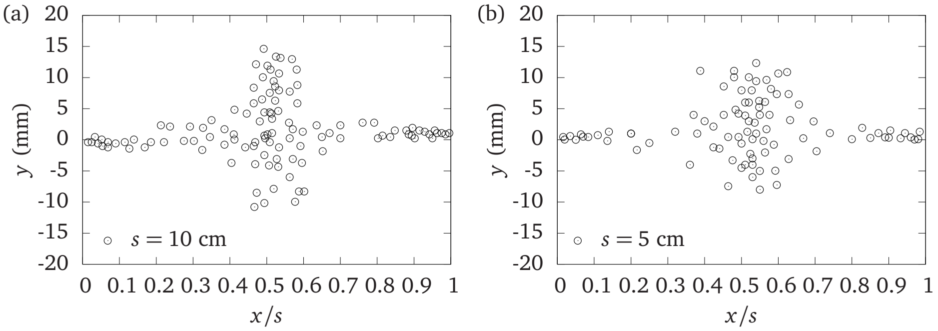

Figure 4.19: Position of coalescence events in $\Delta t = 200$ ms for (a) $s = 10$ cm and (b) $s = 5$ cm.

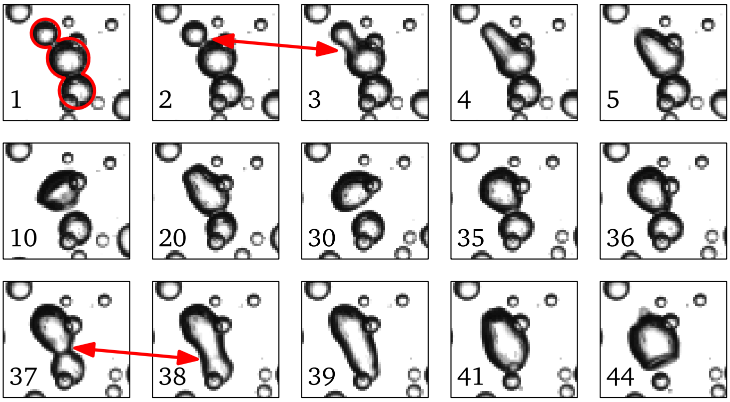

Figure 4.20: Sequence of snapshots showing the coalescence process of three bubbles into a single daughter bubble. The two coalescence events are marked with double-arrows.

Comparing the normal gravity case (Figure 4.8) with the microgravity case (Figure 4.19), two main differences are pointed out: (i) in normal gravity, the coalescence positions are more distributed in space than in microgravity, in the latter case the coalescences occur mainly in two regions: near the nozzles, or in the collision zone. (ii) A higher number of coalescences are observed in microgravity than in normal gravity, for the same amount of observation time.

It should be pointed out that the measurements of Figures 4.19(a) and 4.19(b) have been carried out considering a coalescence a collision of two bubbles creating a single larger daughter bubble, without taking into account the number of coalescences that the colliding bubbles may have suffered before. As an illustrative example, the coalescence of three bubbles into a larger daughter bubble is shown in Figure 4.20. In this process, we have considered two coalescence events (marked with double-arrows) since they occur at different times. No simultaneous coalescence of three or more bubbles into a single daughter bubble have been observed from the movies recorded.

4.2 Numerical simulations of single-phase opposed-jet flow

Opposed jets may exhibit different stable configurations, depending on many parameters such as the jet velocity, inlet geometry, separation between jets and other boundary conditions [PSSM06, LSL^{+}08]. Pawlowski et al. [PSSM06], performed a bifurcation and stability analysis of laminar isothermal counterflowing planar jets, and obtained a complex behavior which was classified in four distinct flow modes:

- A symmetric single steady state.
- Two stable asymmetric states and one unstable symmetric state.
- A “deflecting jet” oscillatory flow.
- A time-dependent chaotic flow with vortex shedding.

However, the results of their study were obtained for wall-bounded opposed jets, with Reynolds number as a continuation parameter. In their investigation, a detailed analysis on the offset of the stagnation point, which appears as a Pitchfork bifurcation [PSSM06], is presented. This situation can be encountered when using two identical opposed jets, injecting the same amount of momentum, at certain aspect ratios and Reynolds numbers. Starting with low Reynolds numbers, there is only one symmetric stable state. As the Reynolds number is increased, this symmetric state becomes no longer stable, giving rise to two stable configurations in which the stagnation point remains in the injection axis but is deviated from the middle-plane between the two nozzles. This configuration remains symmetric with respect to the injection axis. Another type of instability is the so-called deflecting jets instability, which consists of the appearance of periodic oscillations presented by the deflecting jets at a fixed frequency. This instability appears as a Hopf bifurcation [PSSM06].

Another kind of instability, found in the present study, appears with the form of velocity waves in the outflowing jets. This instability can be inhibited by turbulent mechanisms as we shall see in Section 4.2.2.

In Figure 4.21, schematics of different types of bifurcations that may appear in the opposed-jet configuration are presented.

Motivated by the rich behavior of flow patterns that the opposed jets may exhibit, a numerical study of the opposed-jet configuration at different Reynolds numbers and aspect ratios have been performed.

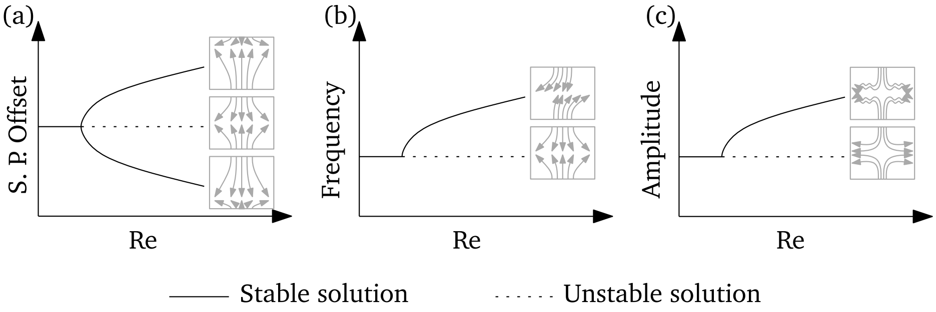

Figure 4.21: Different types of bifurcations encountered in the opposed-jet configuration. (a) Stagnation Point Offset, Pitchfork bifurcation. (b) Deflecting jets instability, Hopf bifurcation. (c) Outflowing waves instability.

4.2.1 Numerical procedure

The governing equations and solver algorithms used for the numerical simulations are described in Appendix B.1.

4.2.1.1 Boundary and initial conditions

The balance equations were solved in a two-dimensional square domain with dimensions of $h \times h$ (in units of d), where h is the separation between nozzles. Hence, for opposed jets separated by $h = 30d$, the domain was a square of 30×30 (d units). Cartesian coordinates (x, y) have been used, being $y = 0$ the direction of injection (axial direction), and $x = 0$ the stagnation line. The inlets are vertically centered and the velocity profile is uniform, acting on $t > 0$. Thus, for the right injector the velocity value is $v = 1$ (in u units), and for the left injector the velocity value is $v = -1$. A fixed constant pressure equal to the atmospheric value $p_0 = 10^5$ Pa was applied to the outlet boundaries. In Figure 4.22, the domain used for the numerical simulations is sketched. The sides of the square (dotted lines) with dimensions $h \times h$ are the outlet boundaries with fixed pressure, and the inlets (solid lines) have a uniform velocity profile and a diameter of $d = 1$. In all the runs we supposed that at $t = 0$ the fluid was at rest. At $t > 0$, the inlets were activated with a uniform velocity profile.

4.2.1.2 Computational grid and time steps

The computational grid consists in 100×100 non-uniform rectangular cells, with refinement in the regions with high gradients, i.e. near the stagnation line and the

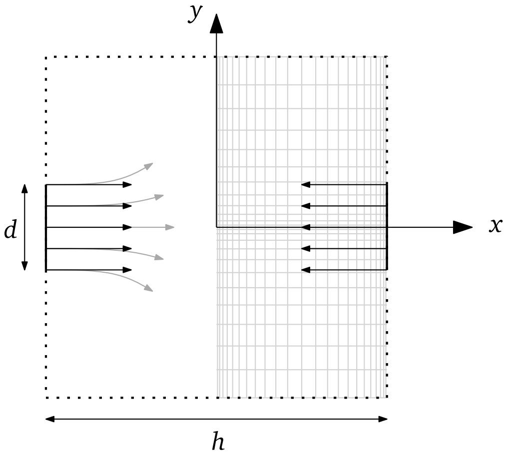

Figure 4.22: Computational domain used for the numerical simulations. Cartesian coordinates (x, y) are used. Dotted lines: outlets at a fixed pressure. Straight solid arrows: inlets with a uniform velocity profile.

injectors. The x (axial) direction is divided in 100 cells, which are distributed as follows:

- For $-h/2 < x < 0$, 50 cells following a symmetric power law with exponent $+1.4$.
- For $0 < x < h/2$, 50 cells following a symmetric power law with exponent $+1.4$.

The y direction is divided in 100 cells, distributed in the following way:

- For $-h/2 < y < -d/2$, 40 cells following a power law with exponent -1.4.
- For $-d/2 < y < d/2$, 20 uniform cells.
- For $d/2 < y < h/2$, 40 cells following a power law with exponent $+1.4$.

The computations were carried out using an Intel® Xeon® X5450 CPU 3.00 GHz with 32 GB RAM. The computational times ranged from 20 minutes up to 12 hours for the most refined grids.

The transient solutions of the pressure and velocity fields have been obtained from $t = 0$ to $t = 1000$ (in time units of d/u), using 500 uniformly distributed time steps. Hence, each time step correspond to 0.002 time units. The solver computes 50 iterations for each time step in order to achieve the convergence of the solution.

With the aim to determine the effects of grid resolution on the solution, tests have been made with increasing number of cells. Four successively refined grids

Grid	ε_p (%)	ε_{v_x} (%)	ε_{v_y} (%)	CPU Time (s)
100×100	1.2	0.80	1.13	1214
200×200	1.2	0.37	0.56	4260
300×300	0.4	0	0	10380
500×500	-	-	-	41220

Table 4.3: Effects of grid resolution on the errors of the solution and computational time.

have been used, with the same grid distribution that the one presented above. The number of cells in the tests were: 100×100, 200×200, 300×300 and 500×500 in order to provide the highest resolution in regions of high velocity gradients. The relative errors in pressure and velocity have been computed, taking as a reference the value computed by the 500×500 mesh. Hence, the relative error ε_p of the pressure for the 100×100 grid has been calculated as follows

$$\varepsilon_p = \frac{p(500 \times 500) - p(100 \times 100)}{p(500 \times 500)} \times 100. \tag{4.11}$$

And the same procedure have been used for the other variables. In Table 4.3, the relative errors and the computational time obtained by the different grid resolutions are presented. In summary, the 100×100 grid produced profiles which agreed with the 500×500 grid profiles with relative errors less than 1.2%, and the convergence was achieved in much less computational time. Therefore, the 100×100 mesh was used throughout the rest of the calculations in this study.

4.2.2 Results and discussion

In the present study, the Reynolds number ranges between $10 \leq \mathrm{Re} \leq 2000$ and the aspect ratio $5 \leq h/d \leq 50$. The transient solutions of unbounded opposed jets in the studied range of parameters, can be divided in four different regimes. In Figure 4.23, these regimes are sketched in the evolution of some property ϕ (i.e., the pressure, the x- or y- components of the velocity field, measured at a certain point inside the domain) as a function of time. Depending on the value of Re and h/d, a single opposed-jet configuration can pass through all the different regimes, as we shall see later. The first regime, correspond to $0 \leq t < t_s$, where t_s is the stabilization time, is the so-called “starting jets”. In this regime the free jets expand and develop until a steady symmetric solution (stable or unstable, depending on Re and h/d) is reached. This regime of starting jets will be discussed in Section 4.2.2.1. The second regime, analyzed in Section 4.2.2.2, correspond to $t_s \leq t < t_d$, where t_d is the destabilization time. Within this interval of time, the solution remains symmetric. For those configurations in which the symmetric solution is stable ($h/d < 10$ for any value of

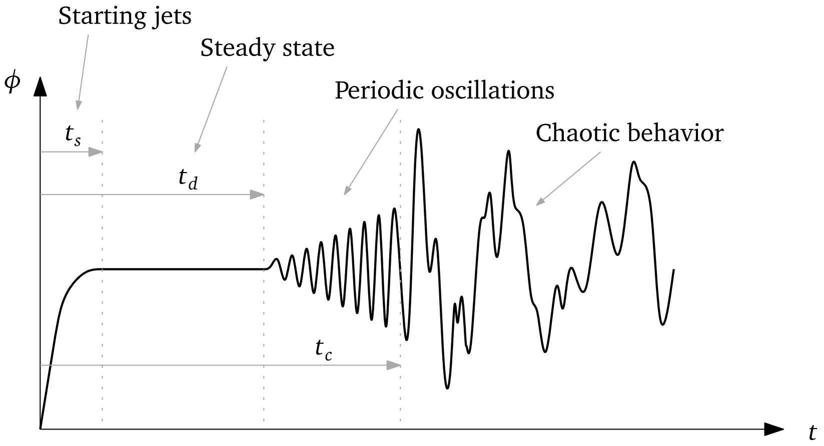

Figure 4.23: Sketch of the time regimes.

Re), the destabilization time tends to infinity, $t_d \to \infty$. Otherwise, the symmetric solution is unstable and t_d has a finite value. At $t = t_d$, the solution becomes destabilized and the symmetry breaks, leading to an antisymmetric solution or a chaotic solution. The antisymmetric solution correspond to deflecting jets which oscillate with a fixed frequency ω, and appears at a critical Reynolds number of $\mathrm{Re}_c = 125$ at $h/d = 10$. For the cases in which the aspect ratio $h/d > 10$, the critical Reynolds number decreases, $\mathrm{Re}_c < 125$. Concerning the amplitude of the oscillations of the deflecting jets instability, an increase of the amplitude is observed until at a time t_c (which stands for "critical time"), the oscillation pattern becomes broken and the solution behaves chaotically. The results obtained at this time interval $t_d \leq t < tc$ in which transition to instability occurs, will be presented in Section 4.2.2.3. For $t_c \leq t < 1$, the solution is fully chaotic. For $\mathrm{Re} \geq 1000$ and $h/d = 10$, another type of instability has been found. In this case, the starting jets do not reach a steady state due to the apparition of some kind of outflowing waves in the outgoing vertical jets. However, the solution with the outflowing waves remains symmetric respect to $x = 0$ and $y = 0$, until at t_d the deflecting jets instability takes place. At this moment, a superposition of the two instabilities is observed in the flow. We have found that turbulence has some efficacious mechanism to inhibit this outflowing waves instability. In Section 4.2.2.4, we present results of the comparison between laminar and turbulent cases, showing that in the turbulent case there is some effective mechanism to suppress the outflowing waves instability.

4.2.2.1 Starting jets

At $t = 0$ all the fluid in the domain is at rest. For $t > 0$, the inlets are activated creating the starting counterflowing jets. The developing jets have initially a mushroom-like shape, until the opposing jets collide with each other. This was observed experimentally by Voropayev et al. [VA92], Afanasyev et al. [AVP95] and Voropayev et al. [VAKF03]. The evolving horizontal jets are symmetric with respect to the stagnation line $x = 0$ and with respect to the injection axis, $y = 0$. When the two opposed jets encounter each other at the center of the domain, the pressure increases locally in the encounter region. After the collision of the horizontal jets, two vertical jets with symmetry respect to the stagnation line and to the injection axis start to evolve. The initial shape of the starting vertical jets is also mushroom-like, until the mushroom heads pass through the outlet. After some time steps, the solution stabilizes and becomes steady. The stability of the solution depends on Re and h/d. For $h/d < 10$, the symmetrix steady solution is stable. However, for $h/d \geq 10$, the symmetric solution is unstable for $\mathrm{Re} \geq 125$.

In Figure 4.24, velocity contours of the starting counterflowing jets for $\mathrm{Re} = 100$, with an aspect ratio ranging from $h/d = 5$ to $h/d = 50$ are presented. The velocity field is symmetric respect to axial direction $y = 0$ and the stagnation line $x = 0$ for the starting jets. In the right part of Figure 4.24, which correspond to the longest times, the velocity field becomes steady and has a cross-like shape. This steady solution for $h/d = 5$ and $\mathrm{Re} = 100$ is stable at $t \to \infty$. However the steady solution for $h/d = 50$ and $\mathrm{Re} = 100$ is unstable.

4.2.2.2 Steady symmetric solution

The pressure and velocity profiles of the symmetric stable solution for an aspect ratio of $h/d = 10$ and $\mathrm{Re} = 50$ are presented in Figure 4.25. Normalized velocities and pressure are plotted as a function of the normalized position for different values of x and y. In the plot $v_x(x)$ (Figure 4.25(a)), the x component of the velocity ranges from $v_x = 1$ (left injector) to $v_x = -1$ (right injector) in the injection axis $y = 0$. As we increase y, the value of v_x near the nozzle jumps from $v_x \approx 1$ to $v_x \approx 0$. Increasing y and looking at v_x along the whole injection axis, one can note that v_x is being decreased and at $y = 5.0$ (and $y = -5.0$ by symmetry) all the fluid has only vertical outgoing velocity.

In the plot $v_x(y)$ (Figure 4.25(b)), we can observe that at $x = 5.0$ the x-velocity is not a perfect step function near the boundaries of the inlet. This can be explained since there are no walls in the domain, and the fluid at the nozzle exit (with $|v_x| = 1$) drags part of the fluid near the nozzles, which was initially at rest. This introduces an additional amount of liquid in the domain. As we approach the stagnation line ($x = 0$), the x-velocity is being diffused. At the stagnation line, $v_x = 0$ by symmetry. In the plot $v_y(x)$ (Figure 4.25(c)), we can observe that as we increase y, the vertical

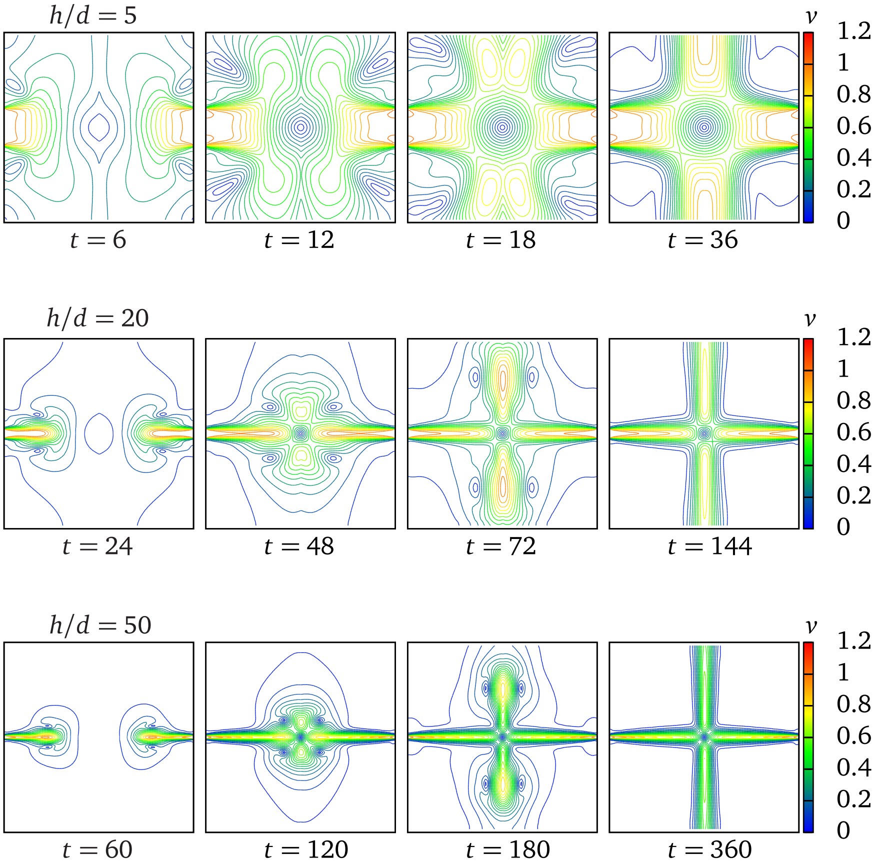

Figure 4.24: Starting jets with Re = 100 and an aspect ratio ranging from $h/d = 5$ to $h/d = 50$.

component of the velocity becomes negative near the edges of the domain. This ensure mass conservation inside the domain, since there is an additional amount of incoming fluid near the nozzles (the dragged fluid by the injected liquid). The plot $v_y(y)$ (Figure 4.25(d)) shows that the outgoing velocity does not have a maximum value of $|v_y| = 1$ at $x = 0$, since the outgoing jets are slightly wider than the impinging jets. This is reasonable since the closed line integral of the velocity profile at the boundaries must be zero to ensure mass conservation in the domain, and if the outgoing jets are wider than the opposed jets, the velocity must be lower. Figure 4.25(e) shows that pressure reaches a maximum value in the stagnation point, and vanishes at the boundaries. We must note in the plot of $p(y)$ (Figure 4.25(f)) that some values of the pressure near the nozzles are negative. In fact, the pressure is not negative since the pressure we are plotting is the relative dimensionless pres-

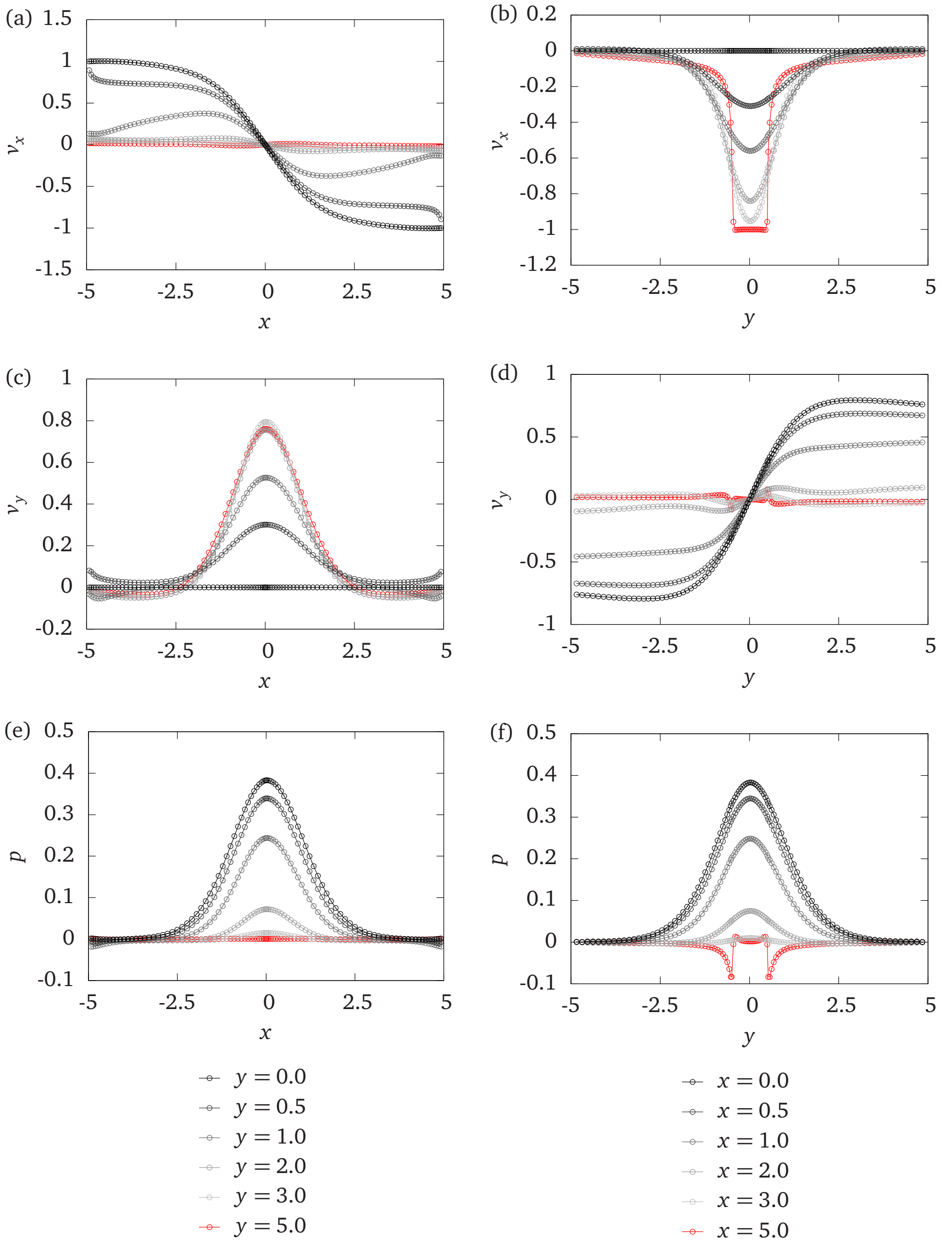

Figure 4.25: *Left:* velocity profiles and pressure for different values of y. *Right:* velocity profiles and pressure for different values of x. The solution is stable, with an aspect ratio of $h/d = 10$ and $\mathrm{Re} = 50$.

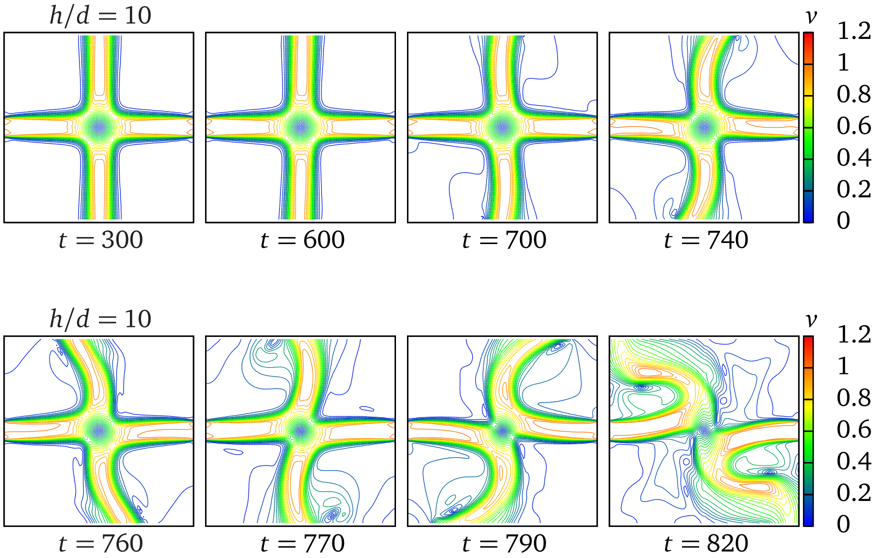

Figure 4.26: Transition to instability with periodic oscillations ($\mathrm{Re} = 500$).

sure, $p' = (p - p_0)/(\rho u^2)$ (see Section B.1.1), where $p_0 = 10^5$ Pa is the atmospheric pressure applied at the outlet boundaries.

4.2.2.3 Transition to instability

Up to now we have presented the pressure and velocity profiles for the steady solution. If this steady solution is unstable, the symmetry will be broken when some perturbation is applied to the system. As a result, we shall see that at a certain time t_d, the solution destabilizes becoming chaotic. In some cases, the transition between the steady and chaotic solutions present an oscillation pattern with a fixed frequency. Otherwise, the solution becomes chaotic without any oscillations nor periodic patterns.

In Figure 4.26, a series of snapshots of the velocity contours for $\mathrm{Re} = 500$ and $h/d = 10$ at different times are shown. At $t = 300$, we start from the symmetrical solution. At $t > 300$, the solution starts to oscillate with an increasing amplitude. After some periods of oscillation, at $t \approx 770$ the amplitude is too high and the oscillation pattern breaks. Note that at $\mathrm{Re} = 500$ and $h/d = 10$, the solution is quasi-antisymmetric.

In Figure 4.27, a series of snapshots of the velocity contours for $\mathrm{Re} = 500$ and $h/d = 50$ are presented. At $t = 220$ we start with the unstable symmetric solution. In this case, no oscillation patterns occurs. The solution is initially symmetric ($t = 220$) and becomes antisymmetric ($t = 260$ until $t = 440$). At $t > 450$, it loses its

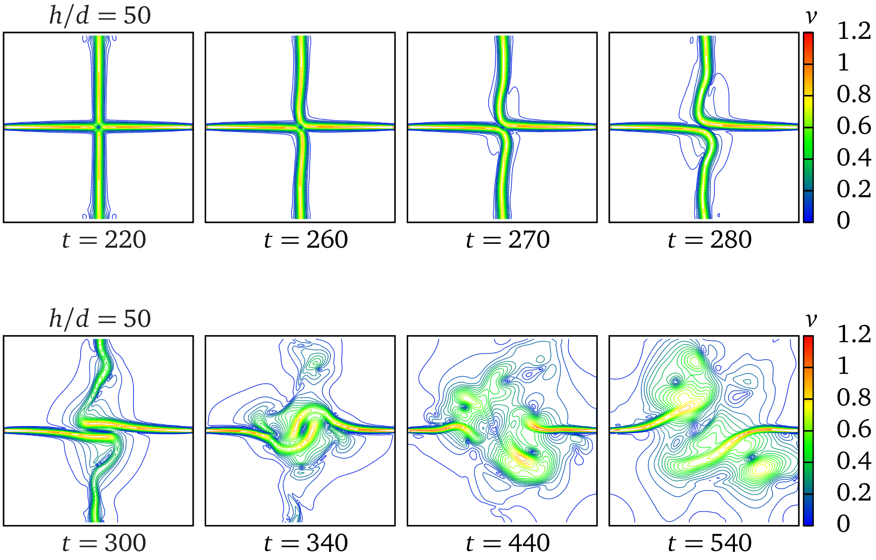

Figure 4.27: Transition to instability without periodic oscillations (Re = 500).

symmetry completely becoming chaotic.

In order to study this transition between steady and chaotic behavior, it is convenient to measure the frequency ω of the oscillation patterns with the aim to get a guiding parameter which can describe the transition to instability. With the objective to quantify the guiding parameter, we have measured the vertical component of the velocity at a fixed point ($x = -0.5$, $y = 4.85$) for the case of $h = 10d$ as a function of time for different Reynolds numbers. In Figure 4.28 the variation of the vertical component of the velocity v_y as a function of time is presented. The plot in Figure 4.28(a) has been computed with Re $= 150$, while in Figure 4.28(b) with Re $= 500$. In both cases the solution passes through the four different flow regimes, marked as (i), (ii), (iii), and (iv) regions. At $0 < t \lesssim 100$ the jets evolve until at $t \approx 100$ the solution becomes steady. At $t = t_d$ ($t_d \approx 380$ for Re $= 150$ and $t_d \approx 300$ for Re $= 500$), the solution destabilizes and the amplitude of the instability increases until at $t = t_c$ ($t_c \approx 850$ for Re $= 150$ and $t_c \approx 700$ for Re $= 500$) the constant frequency oscillation pattern disappears. The destabilization time t_d is higher in the case of Re $= 150$ than in the case of Re $= 500$, although the oscillation frequency ω is slightly lower.

The measurement of t_d have been done visually, from the plots obtained, and no numerical criteria have been employed.

In Figure 4.29, the destabilization time t_d is plotted as a function of Re (Figure 4.29(a)) and h/d (Figure 4.29(b)). For nozzle separations equal to 10 diameters, the destabilization time decreases with increasing Re until it reaches a minimum value

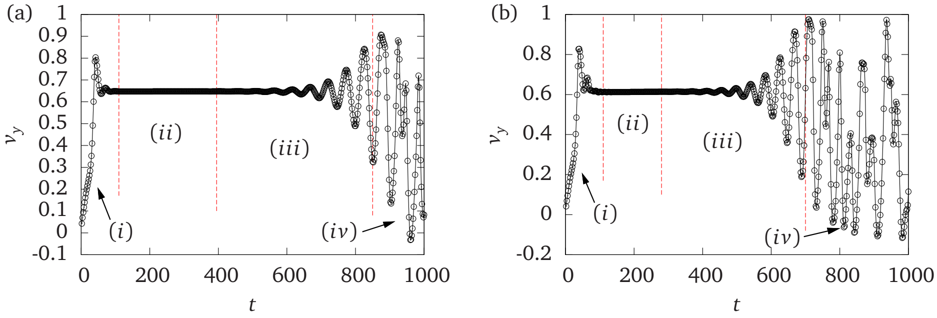

Figure 4.28: Vertical velocity component as a function of time for $h/d = 10$, measured at the point ($x = -0.5$, $y = 4.85$). (a) Re = 150. (b) Re=500. (i): Starting jets. (ii): Symmetric unstable solution. (iii): Oscillation pattern. (iv): Chaotic behavior.

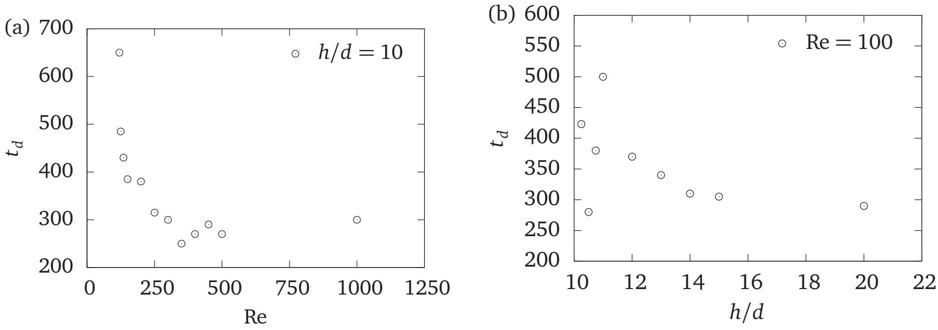

Figure 4.29: (a) Destabilization time as a function of Re, for $h/d = 10$. (b) Destabilization time as a function of h/d for Re=100.

at Re $\approx$ 400. Increasing Re further, the destabilization time maintains constant, between $200 < t_d < 300$. For a fixed value of Re = 100, the destabilization time decreases with increasing aspect ratios in a general perspective, although at low aspect ratios there is a high scattering of the measured values.

With the aim to reproduce the bifurcation in Figure 4.21(b), we have plotted the oscillation frequency ω as a function of the Reynolds number and the aspect ratio. In Figure 4.30(a), we can observe that for $h/d = 10$ and Re < 125, the steady solution is stable and no oscillation pattern occurs. At Re = 125, the jets suffer deflection at large times. For Re > 125, the oscillation frequency of the deflecting jets increases with the Reynolds number. In Figure 4.30(b), we can observe that for nozzle separations $h \leq 9d$ the symmetric solution is stable. At $h/d = 10$, the solution destabilizes, with a fixed frequency of deflection. As we increase the aspect ratio for

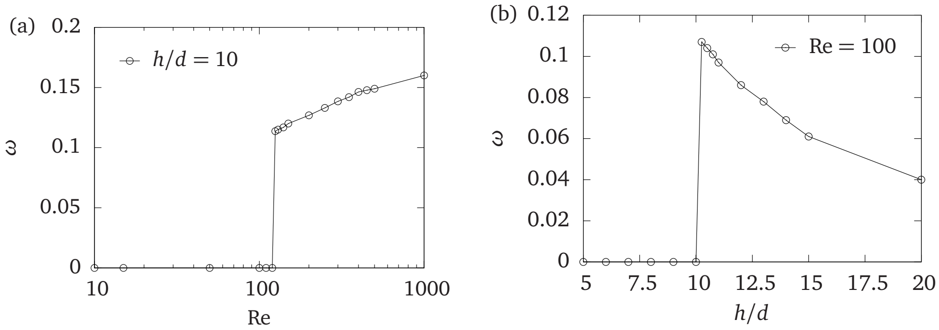

Figure 4.30: (a) Bifurcation diagram for $h/d = 10$ with Re as a continuation parameter. Oscillation frequency ω is plotted as a function of Re. (b) Bifurcation diagram for Re=100 with h/d as a continuation parameter. Oscillation frequency ω is plotted as a function of h/d.

a fixed Reynolds number, the frequency decreases until at $h = 20d$ the oscillation patterns disappears. For $h/d > 20$, the transition from the steady solution to the chaotic solution has no longer periodic patterns, and behaves in a similar fashion than that of presented in Figure 4.27.

4.2.2.4 Inhibition of outflowing waves by turbulent mechanisms

Maintaining a fixed separation between nozzles of $h = 10d$ and increasing the Reynolds number, a new type of instability appears at Re = 1000. This instability has the form of outflowing waves that are formed in the outgoing jets. As a result, the width of the outgoing (vertical) jets oscillates periodically. In the regions where the width of the outgoing jets is lower, the velocity is higher. This ensures the mass conservation, since the incoming mass from the nozzles ($v = 1$, $d = 1$) has to be compensated by the amount of mass carried out by the outgoing jets. This amount of mass can be computed as the integral of the velocity profile through the jet width at a certain value of y, and the closed line-integral of the total velocity profiles at the boundaries must vanish. In this situation, the time evolution of the flow field is as follows: at earlier times, the opposed jets evolve as described in Section 4.2.2.1. Then, the solution does not stabilize reaching steady profiles similar to those presented in Figure 4.25, instead, the solution presents outflowing waves but maintaining the symmetry. At $t > t_d$, the deflecting jets instability described in Section 4.2.2.3 appears and superposes to the outflowing waves instability.

In Figure 4.31(a), velocity contours of the laminar flow field solution at Re = 2000 and $h/d = 10$ are presented. This case corresponds to the symmetric solution before the deflecting jets instability occurs. It can be observed in the outgoing ver-

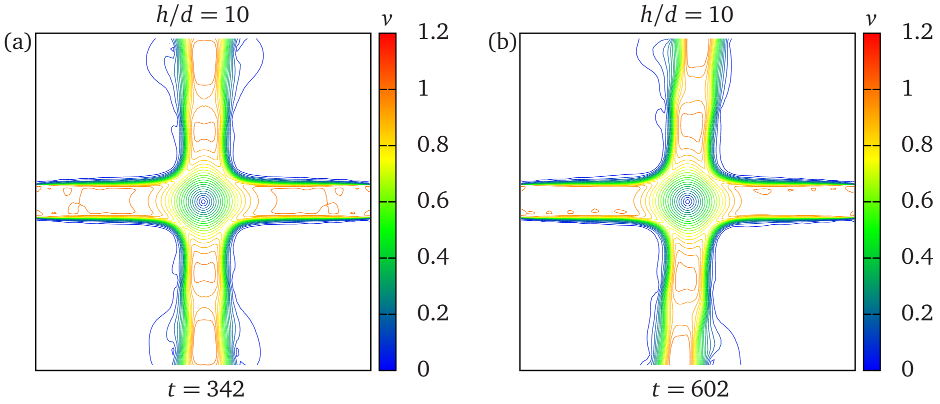

Figure 4.31: Velocity contours of laminar opposed jets (Re $= 2000$). (a) Outflowing waves instability. (b) Outflowing waves instability superposed to deflecting jets oscillation.

tical jets, that the width of the jets slightly change in a periodic way as we increase y. The regions in which the width is lower, the velocity is higher. In Figure 4.31(b), a superposition of the outflowing waves instability and the deflecting jets instability is shown. In this situation, the amplitude of the deflection increases and the vertical jets turn from side to side oscillating with a fixed frequency. Additionally, the width of the outgoing jets (and also the local velocity, by mass conservation) varies in a periodic way. With the aim to consider the effects of turbulence on the flow, numerical simulations using the Chen and Kim turbulence model (see Section B.1.2) have been carried out. For a fixed nozzle separation of $h = 10d$, the Reynolds number have been increased from Re $= 1000$ to Re $= 2000$. In the laminar case, we observed the outflowing waves and the deflecting jet. However, with the turbulent model, the outflowing waves instability is not present anymore and the deflecting jets instability is the only one which has been observed.

To illustrate the effects of the outflowing waves, the y-component of the velocity has been measured at a fixed point ($x = -0.5$, $y = 4.85$) as a function of time. In Figures 4.32(a), 4.32(c) and 4.32(e), v_y is plotted as a function of time for the laminar case. For Re $= 1000$, the solution reach a quasi-steady value, with slight oscillations. As we increase Re, the amplitude of the outflowing waves instability becomes higher. For Re $= 1500$ and Re $= 2000$, the solution does not reach a steady value due to the oscillations of the jet width. Between $t \approx 400$ and $t \approx 600$, one can observe the effects of the deflecting jet instability with increasing amplitude. At $t \approx 600$, the symmetry becomes broken and the solution starts to behave chaotically. However, the situation in the turbulent case is drastically different. The solution does reach a steady state for $1000 \leq \text{Re} \leq 2000$, as can be seen in Figures 4.32(b), 4.32(d) and

4.32(f). The deflecting jets instability is still appearing at $t \approx 400$, and for $t \approx 600$, the solution becomes chaotic. For $1000 \leq \text{Re} \leq 2000$, the solution stabilizes when the flow is turbulent, without the appearance of the outflowing waves instability. This is in contrast to the case of laminar flow model, in which the solution does not reach stabilization for the same values of Re and h/d. Thus, we conclude that there are some turbulent mechanisms that inhibit the outflowing waves instability.

4.3 Numerical simulations of bubbly opposed-jet flow

The numerical simulations have been carried out at ICMCB (Bordeaux, France), using an Intel® Xeon® X5450 CPU 3.00 GHz with 32 GB RAM. The computational times ranged from 2 hours up to 10 hours.

4.3.1 Numerical procedure

The governing equations and solver algorithms used for the numerical simulations are described in Appendix B.2.

4.3.1.1 Boundary and initial conditions

The balance equations have been solved using cartesian coordinates (x, y), being x the direction of injection. The computational domain consists of a two-dimensional rectangular shape with dimensions of $2h \times 9h$, where h is the separation between nozzles(in units of L_0), in order to avoid the effect of the walls. However, only the central region with dimensions $h \times h$ is interesting for us. The nozzles have a diameter $d = L_0$.

The bubble injection have been modeled by setting $|v_i| = 1$ (units of v_0) at the nozzle for both phases $(i = 1, 2)$, with the same amount of incoming liquid than gas, corresponding to $f_i = 0.5$ $(i = 1, 2)$ at the nozzles. The turbulence intensity at the inlets have been set to 5%.

Initially the domain is full of quiescent liquid, and at $t = 0$ the two-phase flow enters inside the domain, creating therefore the bubbly jets.

4.3.1.2 Computational grid and time steps

The computational domain consists of a rectangular-shaped grid with 110×110 non-uniform cells. The grid has been divided in 3 regions in the x- direction and in 5 regions in the y- direction, with the following cell distribution:

- x- direction:

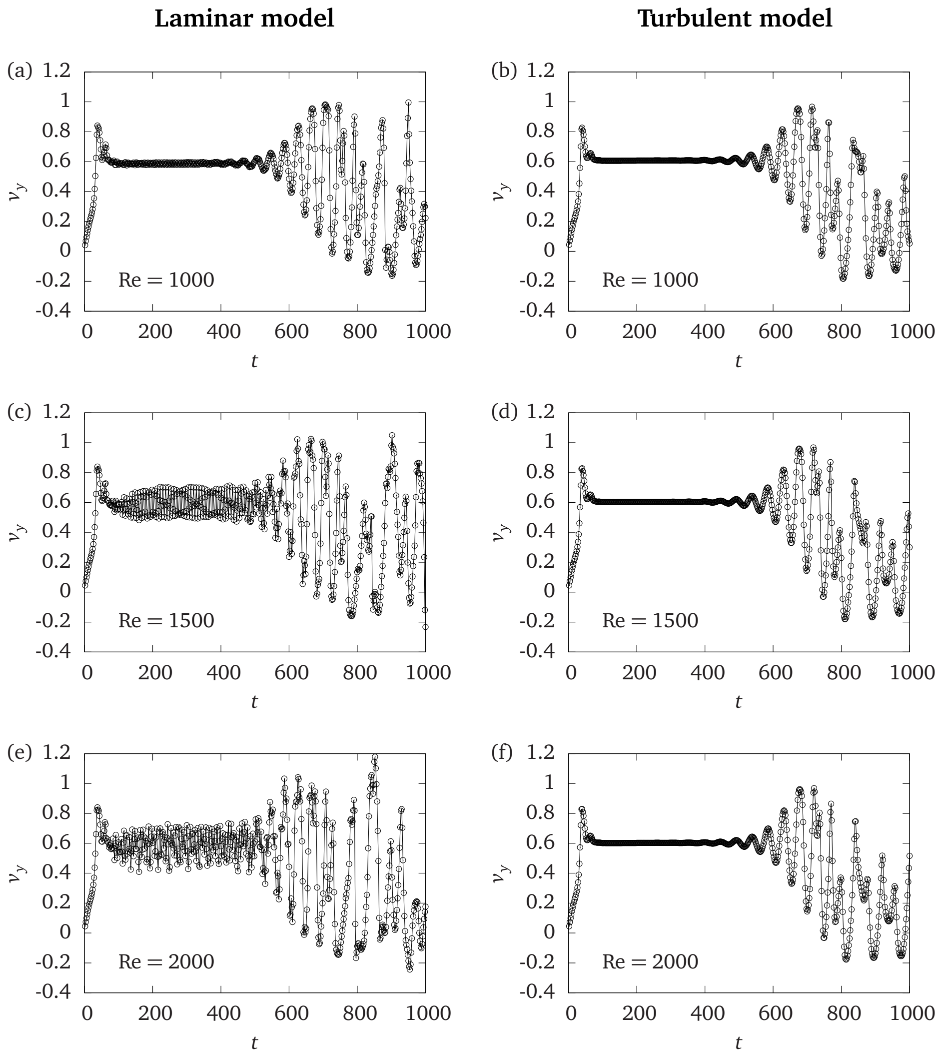

Figure 4.32: Vertical component of the velocity as a function of time, measured at the point ($x = -0.5$, $y = 4.85$). *Left:* Laminar model. *Right:* Turbulent model.

  - For $-h < x < -h/2$, 20 cells distributed along a non-symmetric power law with exponent -1.2.
  - For $-h/2 < x < h/2$, 70 cells distributed along a symmetric power law with exponent $+1.2$.
  - For $h/2 < x < h$, 20 cells distributed along a non-symmetric power law with exponent $+1.2$.

- y- direction:
  - For $-4h < y < -h$, 20 cells distributed along a non-symmetric power law with exponent -1.2.
  - For $-h < y < -d/2$, 30 cells distributed along a non-symmetric power law with exponent -1.2.
  - For $-d/2 < y < d/2$, 10 cells distributed along a symmetric power law with exponent $+1.2$.
  - For $d/2 < y < h$, 30 cells distributed along a non-symmetric power law with exponent $+1.2$.
  - For $h < y < 4h$, 20 cells distributed along a non-symmetric power law with exponent $+1.2$.

The time steps have been set so that each time step corresponds to 0.02 time units. Runs have been carried out from $t = 0$ to $t = 50$ time units, corresponding to 2500 time steps. However, for the case of $h/d = 50$, the runs have been carried out from $t = 0$ to $t = 100$ corresponding to 5000 time steps. The number of iterations have been set to 30 for each time step.

4.3.2 Results and discussion

Simulations have been carried out considering the gravity effects for two values of the Froude number:

- $\frac{1}{\mathrm{Fr}^{*2}} = 0$, which corresponds to a zero gravity case.
- $\frac{1}{\mathrm{Fr}^{*2}} = 1$, which corresponds to a gravity level different from 0.

From now on, we will call this cases “0g” and “1g” respectively, however one should keep in mind that the 1g case only correspond to $g = 9.81$ m/s^2 for certain values of L_0, g_0, and $\Delta\rho/\rho$.

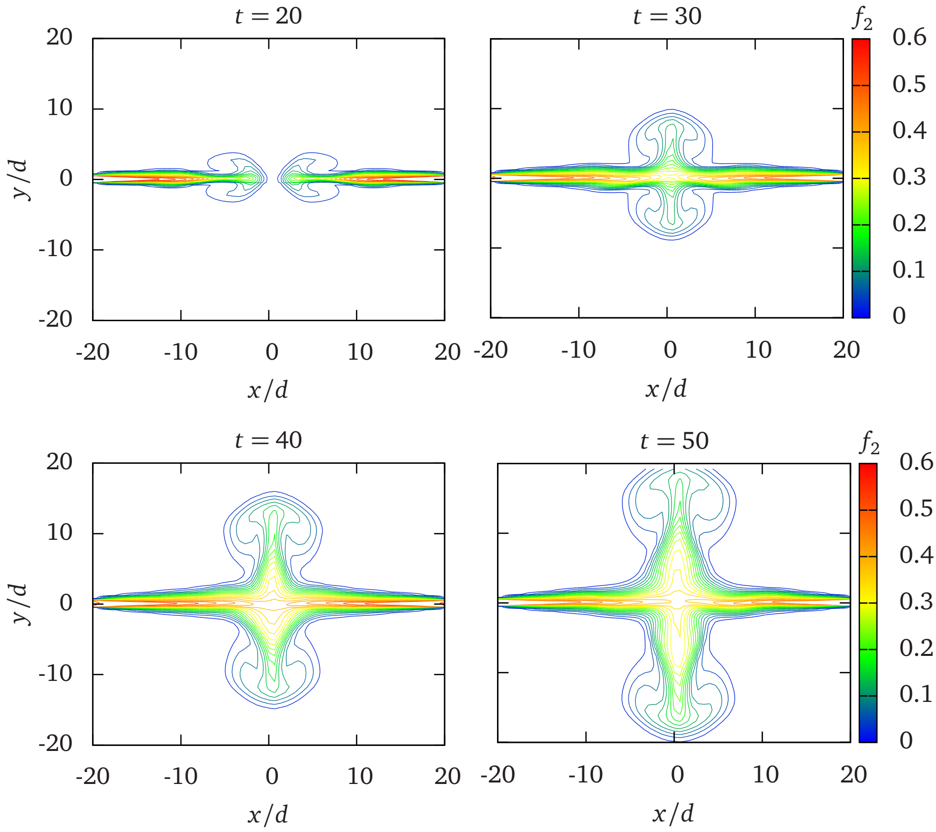

Figure 4.33: Time evolution of gas volume fraction for $h/d = 40$, Re $= 1000$, for the zero gravity case.

4.3.2.1 Symmetric starting jets

In Figures 4.33 and 4.34, the evolution of the gas volume fraction in time is presented for the developing jets, for the zero gravity case and non-zero gravity case respectively.

The jets develop in a symmetrical way with respect to the y-axis, for both microgravity and non-zero gravity cases. The evolution of the gas volume fraction starts with the creation of a vortex dipole (one for each jet) just at the nozzle outlet, so the jet head adopts a mushroom-like shape.

At $t \approx 25$, the developing jets collide with the opposing frontal jet. In the zero gravity case, two outgoing vertical jets are created, and the interaction between jets results in a flow that preserves the symmetry respect to the x-axis and y-axis. In the non-zero gravity case, however, a bubbly plume is created after the initial jets collision and rises in the direction of the gravity force due to buoyancy. For the range

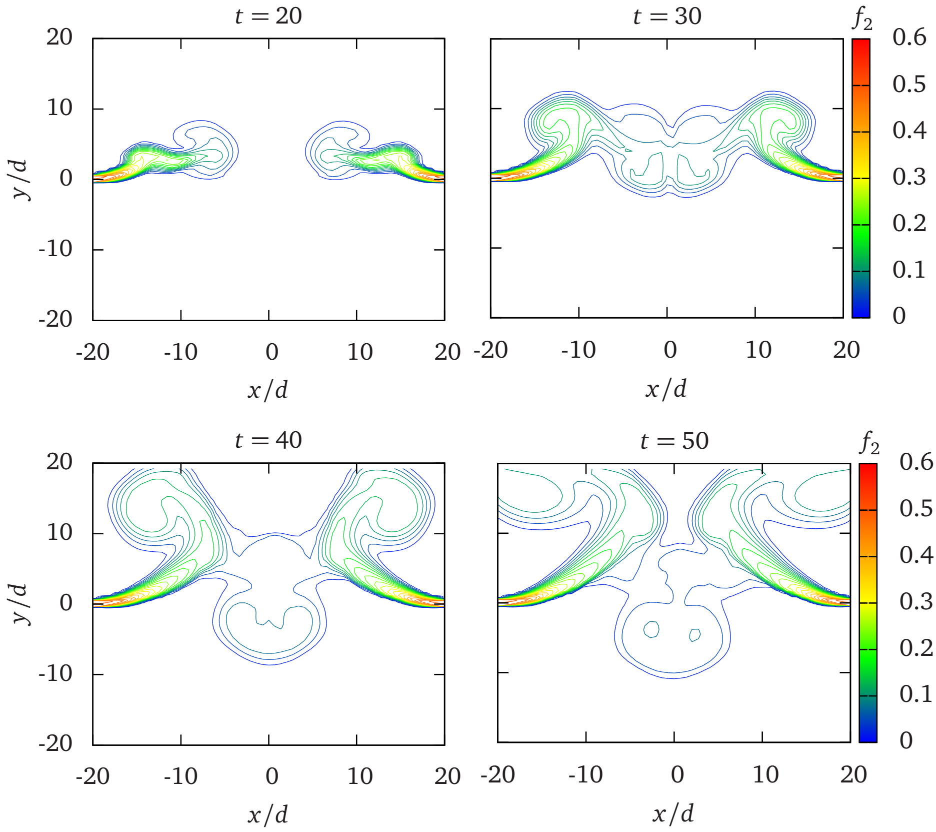

Figure 4.34: Time evolution of gas volume fraction for $h/d = 40$, $\mathrm{Re} = 1000$, for the non-zero gravity case.

of parameters considered in this plots, the bubbly plume flow in non-zero gravity still preserves symmetry with respect to the y direction.

Figures 4.33 and 4.34 show that the initial evolution of the jets is symmetric with respect to the y-axis in both microgravity and non-zero gravity cases. However, for higher values of the time, the flow can become asymmetric (due to the apparition of a deflecting jet instability) depending on the range of parameters considered.

So, the bubbly jets present a symmetric (with respect to the y direction) initial evolution. After the collision, the flow can remain symmetric or antisymmetric depending on the parameter ranges. For example, in the case of non-zero gravity and $h/d = 10$, at $t = t_c$ the deflecting jets instability takes place, resulting in a non-symmetric flow. In the case $h/d = 20$, this instability appears at $t \approx 2t_c$. However, for the case of $h/d = 50$, the deflecting jets instability does not appear due to the fact that the jets are highly separated that the interaction between them is negligi-

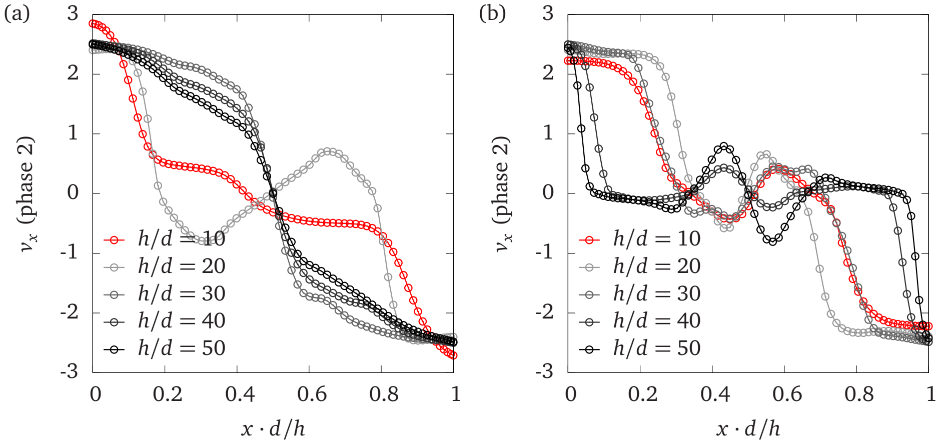

Figure 4.35: Velocity profiles in the injection direction for $t = 50$, Re $= 1000$. (a) zero gravity case. (b) non-zero gravity case.

ble. In the latter case, the bubbly plumes rise in a region near the nozzle and still far from the central zone, so the opposing jets do not interact with each other and they behave like single bubbly jets.

4.3.2.2 Velocity profiles

In Figure 4.35, the x-component of the velocity for phase 2 (gas phase) is plotted in the injection direction. The x-axis is normalized to 1 for all cases from $h/d = 10$ to $h/d = 50$.

In principle, one should expect the x-component of the velocity to be monotonically decreasing along the x-axis. However one can observe in Figure 4.35 that in some regions v_x increases with increasing x. This is due to the creation of vortexs in the following way (different kind of vortex are created in microgravity and in non-zero gravity, so the explanation is divided in two different points):

- In the zero gravity case, a clear increase in v_x while increasing x can be observed in the central region for $h/d = 20$. This is due to the fact that, in this particular case, a deflecting jet instability take place, creating a central vortex (see Figure 4.36-Left). The jet coming from the left is slightly deviated upwards while the jet coming from the right is slightly deviated downwards. This situation results in the generation of a vortex in the central region that rotates clockwise. The presence of this vortex is the responsible to have this increase in v_x with increasing x.

- In the non-zero gravity case, the situation is slightly different. As seen earlier, the initial developing jets adopt a mushroom-like shape before they collide.

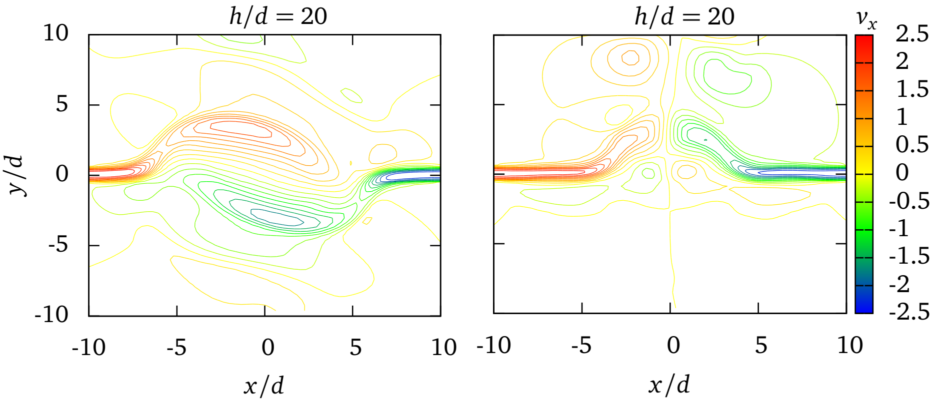

Figure 4.36: Contours of the x-component of the velocity for $h/d = 20$, $t = 50$ and $\mathrm{Re} = 1000$. *Left:* zero gravity case. *Right:* non-zero gravity case.

Just before the collision, the two vortex at the bottom approach each other. Since the vortex coming from the left rotates clockwise and the one coming from the right rotates counter-clockwise, a new jet going downwards vertically is generated after the collision. The presence of this jet is the responsible of the increase in v_x (see Figure 4.36-Right).

Hence, the increase in v_x with increasing x can be explained in two ways: in microgravity, a central single vortex can be generated. With non-zero gravity, to interacting vortex (a vortex dipole) can generate a vertically outgoing jet. This vortexs perturb the velocity field in the way that they can produce an increase in v_x.

4.3.2.3 Gas-phase volume fraction in the non-zero gravity case

In Figure 4.37, the contours of the gas phase volume fraction f_2 are presented for different aspect ratios. Each time correspond to a value of aspect ratio, so the case $t = 10$ corresponds to $h/d = 10$, $t = 20$ corresponds to $h/d = 20$, and so on. The time for the plots has been selected in such a way that the jets evolved twice the collision time. To clarify, let's see an example: In the case $h/d = 10$, the jets collide at the central zone at $t_{\mathrm{col}} = 5$, since $x = vt$, the initial velocity is $|\vec{v}| = 1$ and each jet has to reach a distance of $x = 5d$ ($d = 1$ by definition) to arrive at the central zone. Then, the time chosen for an aspect ratio of $h/d = 10$ is $t = 2t_{\mathrm{col}} = 10$. The same with $h/d = 20$, the time is $t = 2t_{\mathrm{col}} = 20$, and so on.

From Figure 4.37 one can observe that for a fixed Reynolds number, as we increase the distance between jets, the interaction between them becomes negligible as expected, and at high distances the jets behave like single jets.

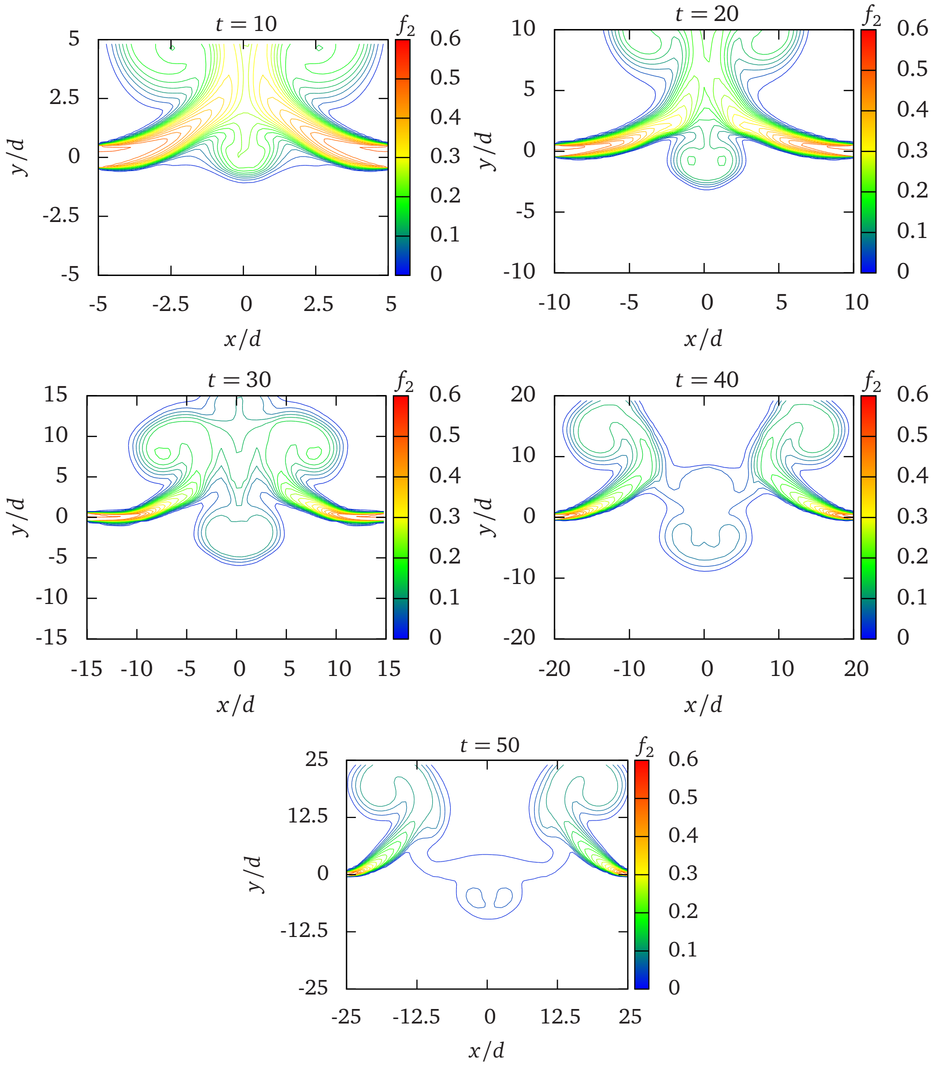

Figure 4.37: Gas phase volume fraction distribution.

4.4 Conclusions

In this chapter, the structure of opposed bubbly jets have been studied in normal gravity and in microgravity conditions.

Numerical simulations on single-phase impinging jets, and impinging bubbly jets have been carried out.

On one hand, the main conclusions of the experimental results of impinging bubbly jets are summarized in the following points:

- A substantial velocity decrease have been observed at the central zone of the opposed-jet configuration due to the strong interaction between the two impinging jets.
- In normal gravity, a large number of coalescence events occur at very short distances from the nozzle, so the vast majority of the coalescences are produced by bubbles coming from the same jet. In microgravity, bubbles can reach the central zone and the coalescences have been found to occur near the nozzles and in the collision zone between the two jets. The coalescence probability is reduced considerably when increasing the momentum flux.
- Bubble mean sizes decrease as the momentum flux is increased, with the size distribution presenting a large tail due to coalescence events.
- No significant changes in the structure of bubbly jets have been observed using distilled water and using ethanol as the carrier liquid.
- At the parameter range studied, bubbles size distribution is not significantly affected by the gravity force. However, bubble velocities at jet centerline are slightly higher near the nozzle in microgravity conditions than in normal gravity. A higher number of coalescences is observed in microgravity with respect to the normal gravity case, for the same amount of observation time.

On the other hand, the most relevant results obtained from the numerical simulations are described below:

- The structure of unbounded impinging jets adopts a cross-like shape. For separation between jets of $s \geq 9d$, this shape starts to oscillate with growing amplitude, evolving to the "defleting jets" instability.
- For a fixed aspect ratio, the destabilization time decreases as the Reynolds number is increased. In a similar fashion, for a fixed Reynolds number, the destabilization time decreases as the aspect ratio is increased.

- A new kind of instability have been found to appear at Re > 1000 for $s = 10d$ in the laminar model. This instability has the form of outflowing waves present in the vertical outgoing jets. This instability can be inhibited by turbulent mechanisms, as confirmed by the turbulent model.

- In microgravity, opposed bubbly jets start to develop adopting a mushroom-like shape, until they collide at the central region, a cross-like shape is attained. After the collision, bubbles spread vertically and two vertical outgoing jets are created. In the non-zero gravity case, however, the bubbly jets collide and a bubbly plume is created.

- Qualitative agreement between the numerical simulation of bubbly jets and the experimental results have been obtained, in terms of the velocity field at the jet centerline and the global structure of the colliding jets.

CHAPTER 5

Bubble coalescence with a free surface

In the present chapter, we present experimental results on the behavior of air bubbles rising and coalescing with a free surface [SnGC10b]. All the experimental results presented herein, are obtained at normal gravity conditions. However, the same experiments will be performed at higher gravity levels (between 1 g_0 and 20 g_0, where $g_0 = 9.81$ m/s^2) in a near future at the LDC in ESTEC (The Netherlands).

In Section 5.1, the terminal velocity, the drag force and the deformed shape of the bubbles are studied in the steady rise zone. In Section 5.2, the time variation of the bubble shape due to the collision of the bubble with the free surface is described. In addition, bubble position and velocity during the bouncing process are analyzed, describing the behavior of the bounce height and the time between the first collision and the final coalescence.

5.1 Bubble rising

When a bubble detaches from a nozzle, it is accelerated by the buoyancy force until it reaches a terminal velocity when the drag and buoyancy forces compensate each other. Afterwards, the bubble rises steadily a few centimeters until it is at a certain distance from the free surface, which starts to deform due to the presence of the approaching bubble. This deformation increases as the bubble gets closer to the free surface and is caused by the amount of fluid displaced by the rising bubble. In the short period of time between when the deformation starts and the bubble impacts into the free surface, no significant variation in the bubble velocity is observed. If the bubble diameter is below a critical threshold ($d_c = 0.47$ mm in the present case), it coalesces immediately. In contrast, if the bubble is larger than a critical size,

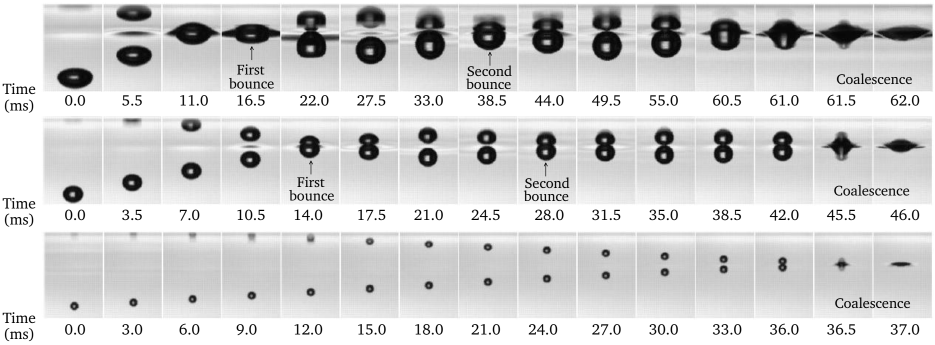

Figure 5.1: Snapshots of rising bubbles and the interaction with the free surface. From top to bottom: bubble equivalent diameters are $d_e = 1.62$, 1.06 and 0.43 mm.

it impacts with the free surface and bounces a few times before coalescence takes place.

The experimental setup for the study of bubble rising, bouncing and coalescing with a free surface is described in Section 2.3.

Two different stages are examined separately. The first one corresponds to the steady rise of the bubbles, in which the measured parameters do not change in time. The second stage corresponds to the time between when the bubble approaches closely the free surface and when coalescence occurs. In this second stage parameters like surface area, aspect ratio or velocity do change in time, and a dynamic analysis is needed.

In Figure 5.1, time sequences of bouncing bubbles are shown. The first, second and third rows correspond to bubbles with equivalent diameters $d_e = 1.62$ mm, 1.06 mm and 0.43 mm, respectively. As can be observed, the smallest bubble does not bounce but coalesces immediately just after touching the free surface. The other two bubbles bounce twice before coalescence occurs. In order to be able to show the bouncing process for the three bubbles in the presented sequences, the time separation between frames is not the same for all bubbles, and indeed is not constant for a single bubble. In the first row, consecutive frames are separated by 11/2000 s, except the four last snapshots that are separated by 1/2000 s. In the second row, consecutive frames are separated by 7/2000 s, except the two last snapshots that are separated by 1/2000 s. Finally, in the third row, consecutive frames are separated by 6/2000 s, except the three last snapshots that are separated by 1/2000 s.

Bubbles with diameters higher than 2 mm rise following an helical path, not an straight line, hence the collision with the free surface is no longer axisymmetric. For this reason, the results presented herein have a diameter range between 0.2 mm and 2 mm.

The position, shape and velocity of the bubbles were computed by processing the images obtained by the video camera. The local velocity v of the bubble at a certain position (x_i, y_i) was calculated as:

$$v = \frac{\sqrt{(x_i - x_{i-1})^2 + (y_i - y_{i-1})^2}}{\Delta t}, \tag{5.1}$$

where (x_{i-1}, y_{i-1}) is the position of the bubble in the previous frame, and $\Delta t = 0.5$ ms is the time interval between consecutive frames.

The spatial resolution of the acquired images is 30 pixels per millimeter. However, the captures of the bubble surface were not perfectly clear. The distinction between bubble interior and the surrounding liquid can be made with a precision of 2–3 pixels, which leads to an error in the measure of the bubble diameter of ±0.03 mm. No zig-zag or helical translation of the bubbles moving through the liquid was observed from the recorded movies in the studied range of sizes (diameters below 2 mm). This fact justifies the approximation that the whole process of bouncing and coalescence takes place in the y coordinate, the direction of gravity. In addition, the camera provides only a two-dimensional projection of the bubble shape. However, the surface area of the bubble could be determined thanks to its axisymmetry.

We approximate the bubble shapes as axisymmetric oblate spheroids, with a volume $V = \pi d_x^2 d_y/6$, where d_x is the horizontal diameter and d_y is the vertical diameter, with $d_x \geq d_y$ in the steady rise of the bubbles. Since bubbles are not spherical, an equivalent diameter d_e is defined for each bubble as $d_e = \left(d_y d_x^2\right)^{1/3}$, which corresponds to the diameter of a perfectly spherical bubble containing the same volume V of gas. The aspect ratio ϵ is defined as $\epsilon = d_x/d_y$, and the bubble surface area A is given by

$$A = \frac{\pi}{2}\left[d_x^2 + \frac{d_y^2}{2e}\ln\left(\frac{1+e}{1-e}\right)\right], \tag{5.2}$$

which corresponds to the surface area of an axisymmetric spheroid, where $e = \sqrt{1 - d_y^2/d_x^2} = \sqrt{1-\epsilon^{-2}}$. For a spherical bubble, $d_x = d_y = d_e$, $\epsilon = 1$, $e = 0$ and we recover the solution of the surface area of a sphere, $A = \pi d_e^2$.

5.1.1 Drag coefficient

Terminal rise velocity has been measured in bubbles with equivalent diameters ranging between 0.20 and 1.82 mm. In Fig. 5.2 the variation of the terminal velocity as a function of bubble equivalent diameter is shown. The behavior is nearly linear with a slight decrease in the slope from equivalent diameters about $d_e \approx 1.4$ mm due to an increase in the drag force, caused by the high deformation of bubbles ($\epsilon > 1.5$ for $d_e > 1.4$ mm) from a spherical shape.

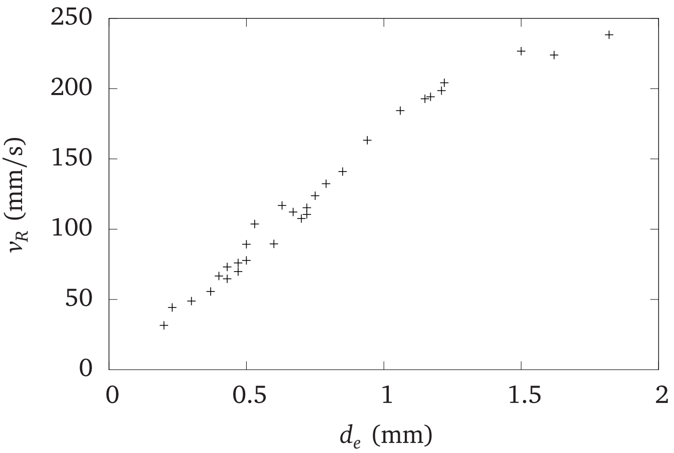

Figure 5.2: Bubble terminal rise velocity as a function of bubble equivalent diameter.

If we assume that the movement remains confined in the y axis (direction of gravity), the force balance becomes

$$\frac{d}{dt}\left[\left(m_B + m_{add}\right) v_y\right] = \frac{\pi}{6} d_x^2 d_y \left(\rho - \rho_a\right) g - \frac{1}{2} \rho v_R^2 C_D \frac{\pi d_x^2}{4}, \tag{5.3}$$

where m_B is the bubble mass, m_{add} is the added mass, v_y is the bubble vertical velocity, $\rho = 789$ kg/m^3 is the fluid (ethanol) density, $\rho_a = 1.2$ kg/m^3 is the air density and $g = 9.81$ m/s^2 is the acceleration due to gravity. In the steady stage, the drag coefficient C_D can be obtained directly from the measured terminal velocities using the balance between the drag and buoyancy forces [LDG05],

$$\frac{1}{8} \rho v_R^2 C_D \pi d_x^2 = \frac{\pi}{6} d_x^2 d_y \left(\rho - \rho_a\right) g, \tag{5.4}$$

which leads a drag coefficient C_D given by

$$C_D = \frac{4}{3} \frac{\left(\rho - \rho_a\right) g d_y}{\rho v_R^2}. \tag{5.5}$$

In order to make a comparison of the C_D obtained experimentally with the available theoretical models, we first note that there are three limiting cases where the drag coefficient can be theoretically obtained [Lot08]:

- $\mathrm{Re} \ll 1$, $\mathrm{We} \ll 1$: linearized inertia and small deformation.
- $\mathrm{Re} \gg 1$, $\mathrm{We} \ll 1$: thin boundary layer, attached wake and small deformation.

- $\mathrm{Re} \gg 1, \mathrm{We} \gg 1$: spherical-cap bubble with separated wake.

The Reynolds number is here defined as $\mathrm{Re} = d_e v_R/\nu$, where $\nu = 1.52 \cdot 10^{-6}$ m^2/s is the kinematic viscosity of ethanol at 20°C. We define the non-dimensional Weber number as $\mathrm{We} = \rho d_e v_R^2/\gamma$, where $\gamma = 0.0224$ N/m is the air-ethanol surface tension. In the present study Re ranges between 5 and 300 and We ranges between 0.01 and 4. Although some of our experimental data correspond to $\mathrm{We} > 1$, we have not observed spherical-cap bubbles in any experimental run. Thus, we consider the second case as the closest one to our parameter range and we will focus on it.

Using potential flow theory, Batchelor [Bat67] predicted a relation between the drag coefficient and the Reynolds number for spherical bubbles in the form:

$$C_D = \frac{48}{\mathrm{Re}}. \tag{5.6}$$

It is assumed in this expression that the boundary layer does not separate from the bubble surface, and the internal motion of the gas has no effect on the liquid motion. Moore [Moo65] obtained a more sophisticated relation for an oblate spheroid, taking into account the dissipation of energy on the boundary layer and in the wake:

$$C_D = \frac{48}{\mathrm{Re}} G(\epsilon) \left(1 - \frac{2.21 H(\epsilon)}{\sqrt{\mathrm{Re}}}\right), \tag{5.7}$$

where $G(\epsilon)$ is given by [Moo65, dVLL02]:

$$G(\epsilon) = \frac{\epsilon^{4/3}}{3} \left(\epsilon^2 - 1\right)^{3/2} \frac{\left[\sqrt{\epsilon^2 - 1} - \left(2 - \epsilon^2\right) \sec^{-1} \epsilon\right]}{\left(\epsilon^2 \sec^{-1} \epsilon - \sqrt{\epsilon^2 - 1}\right)^2}, \tag{5.8}$$

and can be approximated, for $\epsilon < 2$ (which is the case in our experiments), as [Lot08]:

$$G(\epsilon) \approx 0.1287 + 0.4256\epsilon + 0.4466\epsilon^2. \tag{5.9}$$

Although $H(\epsilon)$ must be obtained numerically, a convenient approximation for $\epsilon < 2$ is [Lot08]:

$$H(\epsilon) \approx 0.8886 + 0.5693\epsilon - 0.4563\epsilon^2. \tag{5.10}$$

For a spherical bubble, $\epsilon \to 1$, $G(\epsilon) \to 1$, $H(\epsilon) \to 1$ and one can approximate the drag coefficient by

$$C_D = \frac{48}{\mathrm{Re}} \left(1 - \frac{2.21}{\sqrt{\mathrm{Re}}}\right). \tag{5.11}$$

The values of the drag coefficient obtained from the experimental terminal velocity and Equation (5.5) are plotted in Figure 5.3 as a function of the Reynolds number. Theoretical values are also represented in solid lines computed using Equations (5.9)

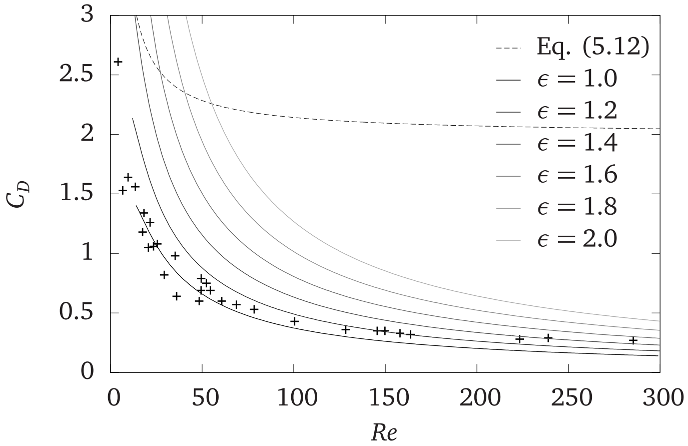

Figure 5.3: Drag coefficient as a function of Reynolds number for different aspect ratios. Dots correspond to experimental results. Dashed line correspond to the prediction for a spherical-cap bubble.

and (5.10) in Equation (5.7). Good agreement between the experimental results and the theoretical prediction is obtained at low Reynolds numbers for spherical bubbles. However, at Re > 150 a small discrepancy can be appreciated, with the experimental values being slightly higher than the theoretical prediction for a spherical bubble. This fact can be explained by the non-sphericity of the bubbles at Re > 150. Since $\epsilon \geq 1$ for rising bubbles, $G(\epsilon) \geq 1$ and $H(\epsilon) < 1$. Thus, considering the effects of surface deformation, the contribution of Equations (5.9) and (5.10) in Equation (5.7) produces an increase in the drag coefficient. The black solid curve in Figure 5.3 corresponds to the prediction for spherical bubbles. As the Reynolds number increases, the aspect ratio of the bubble increases, and the solid curves corresponding to higher aspect ratios become more appropriate to fit the experimental values. However, for the cases $\epsilon = 1.8$ and $\epsilon = 2$, the drag coefficient at high Reynolds numbers is still overestimated. This indicates that the Moore relation can no longer be used at such high deformations of the bubble surface.

The theoretical relation for the drag coefficient in the case We $\gg 1$ and Re $\gg 1$ is given by

$$C_D = \frac{8}{3} + \frac{14.24}{\text{Re}} \tag{5.12}$$

which is plotted in Figure 5.3. A clear discrepancy with experimental data is observed, which confirms that our experiments correspond to the second case (We $\ll 1$ and Re $\gg 1$).

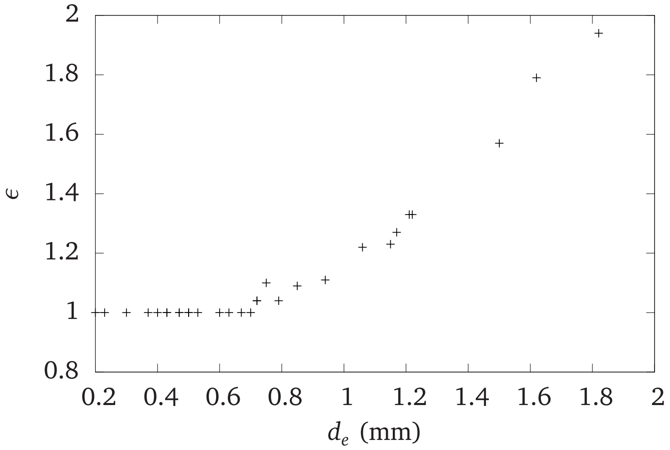

Figure 5.4: Aspect ratio as a function of the bubble equivalent diameter obtained from experimental measurements.

5.1.2 Bubble shape deformation

The shape deformation of bubbles in their steady rise has been measured experimentally. In order to obtain a quantitative measurement of the deformation, the aspect ratio $\epsilon = d_x/d_y$ is considered. The variation of ϵ with the bubble equivalent diameter d_e is shown in Figure 5.4, where it can be observed that all bubbles with $d_e \leq 0.70$ mm can be considered spherical at the present image resolution. For $d_e > 0.70$ mm the aspect ratio increases linearly with d_e at the range studied.

To characterize the effects of the aspect ratio taking into account the bubble size, the non-dimensional Weber number ($\mathrm{We} = \rho d_e v_R^2/\gamma$) becomes appropriate. Moore [Moo65] employed potential flow solution over an oblate spheroid to obtain the following implicit relation between the aspect ratio and the Weber number for clean bubbles:

$$\mathrm{We} = 4\epsilon^{-4/3}\left(\epsilon^3 + \epsilon - 2\right)\frac{\left(\sqrt{\epsilon^2 - 1} - \epsilon^2 \sec^{-1}\epsilon\right)^2}{\left(\epsilon^2 - 1\right)^3} \tag{5.13}$$

For moderate deformations ($\epsilon < 2$) this relationship can be approximated as [Lot08]:

$$\epsilon \approx 1 + \frac{9}{64}\mathrm{We} - 0.0089\,\mathrm{We}^2 + 0.0287\,\mathrm{We}^3. \tag{5.14}$$

For contaminated bubbles, Loth [Lot08] obtained the expression:

$$\frac{1}{\epsilon} = 1 - 0.75\tanh\left(0.11\,\mathrm{We}\right). \tag{5.15}$$

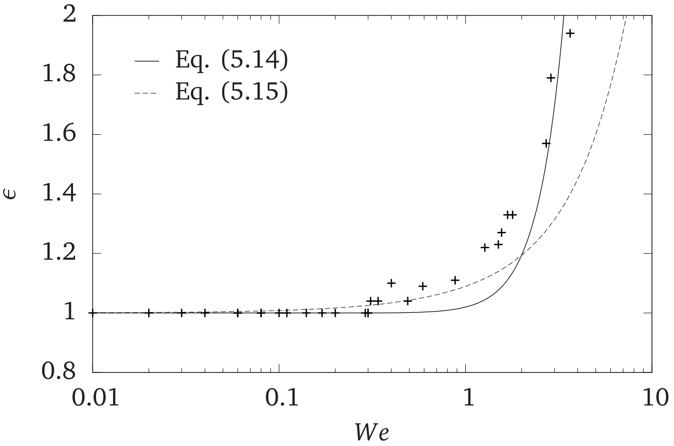

Figure 5.5: Aspect ratio as a function of the Weber number. Points correspond to experimental measurements and lines to theoretical predictions.

In this context, clean bubbles are referred to bubbles with a slip flow along the bubble surface, which is driven by internal circulation. In contrast, the surface of a contaminated bubble has reduced mobility and can be considered as a surface of a rigid body (no-slip condition).

The variation of the aspect ratio with the Weber number is shown in Figure 5.5. Good general agreement between experimental results and the theoretical prediction given by Equation (5.14) is obtained for $\mathrm{We} > 2$. On the other hand, the prediction of Equation (5.15) fits reasonably only for $\mathrm{We} < 2$. This can be due to the fact that for smaller bubbles the terminal velocity is lower, producing a small internal circulation inside the bubble, which does not affect the surface mobility significantly. However, for larger bubbles the internal circulation becomes important and the slip flow in the bubble surface cannot be neglected, thus the deformation of large bubbles behaves similarly to that of a clean bubble.

5.2 Bubble bouncing

5.2.1 Bubble shape dynamics

During the bouncing process, the shape of the bubbles varies in time. Consequently, the drag force and the added mass force become different from the values obtained in the steady rise. In order to see how bubble shape evolves in the bouncing process, the horizontal and vertical diameters of the bubble (d_x and d_y, respectively) have been measured every 1.5 ms. When the center of the bubble was at a distance from the free surface lower than $d_e/2$, we were not able to measure d_y because part of the

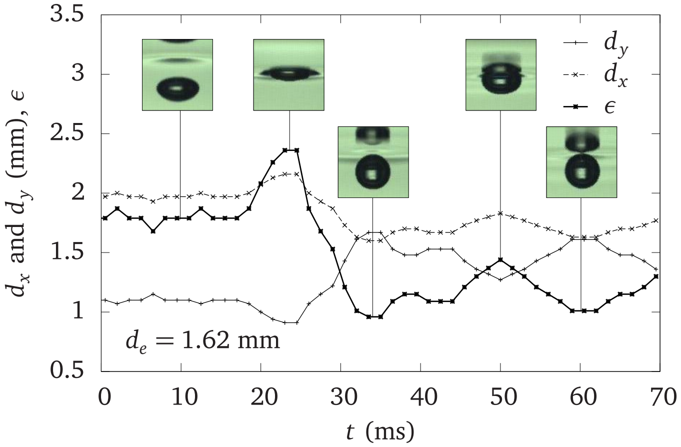

Figure 5.6: Time evolution of the horizontal and vertical diameters and the aspect ratio.

bubble remained hidden behind the free surface. In this case, we imposed a constant volume and we obtained the vertical diameter using the relation $d_y = 6V/(\pi d_x^2)$. From this measurement, the aspect ratio ϵ and the total surface area A (given by Equation (5.2)) have been obtained.

The time evolution of the vertical and horizontal diameters and the aspect ratio of a bubble with $d_e = 1.62$ mm are plotted in Figure 5.6. Cases with $\epsilon < 1$ correspond to bubbles with $d_y > d_x$, in which the bubble shape can be approximated to a prolate spheroid. The aspect ratio remains nearly constant in the steady rise, with approximately $\epsilon = 1.8$, and it gets its largest value when the bubble impacts the free surface with an approach velocity very close to the terminal velocity. At this precise moment ($t = 24$ ms), the bubble is highly deformed from its spherical shape and $\epsilon = 2.4$. After the collision, the bubble becomes nearly spherical with some oscillations of the surface. At the moment where the bubble collides with the free surface in the second bounce ($t = 50$ ms), the bubble is deformed and the aspect ratio reaches a local maximum. However, the deformation of the bubble in the second bounce is lower than that in the first bounce, and even lower than the steady deformation of the bubble in the rise stage.

As described above, the collision between the bubble and the free surface generates oscillations on the bubble surface. The amplitude and frequency of the bubble oscillations could be affected by the presence of the free surface, which can be regarded, at first approximation, as a solid moving wall. The movement can be considered similar to that of a damped oscillator. Our experimental setup was not designed to study bubble oscillations, which deserve a more detailed study. However, we measured the frequency of bubble oscillations for large bubbles, and no influence by the

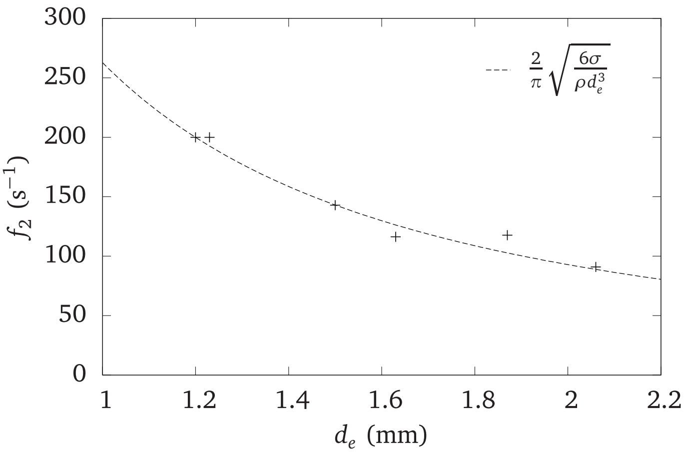

Figure 5.7: Frequency of the second mode oscillations as a function of bubble equivalent diameter. Dots correspond to experimental measurements and line to theoretical prediction.

nearby presence of the free surface was observed. We were only able to measure the frequency of oscillations for large bubbles, since smaller bubbles have larger frequencies and the amplitude of the oscillations is so small that the experimental error is large enough to mask the real values.

Since the first oscillation mode corresponds to a volume oscillation, and the experimental resolution is too low to measure it, the frequency of the second mode of bubble shape oscillations were measured. Lamb [Lam32] gave the general relation for the frequency of the nth mode of an oscillating bubble in an unbounded fluid:

$$f_n = \frac{1}{\pi}\sqrt{\frac{2(n+1)(n-1)(n+2)\gamma}{\rho d_e^3}}. \tag{5.16}$$

With this expression we can compute the relation between the frequency of the second mode and the bubble equivalent diameter, which reads

$$f_2 = \frac{1}{\pi}\sqrt{\frac{24\gamma}{\rho d_e^3}} = \frac{2}{\pi}\sqrt{\frac{6\gamma}{\rho d_e^3}}. \tag{5.17}$$

In Figure 5.7 the variation of f_2 with d_e is shown. The experimental results are in excellent agreement with the theoretical prediction of Equation (5.17), which does not consider the presence of the free surface. Thus, we can conclude that the presence of the free surface does not affect significantly the frequency of the second mode of bubble oscillations.

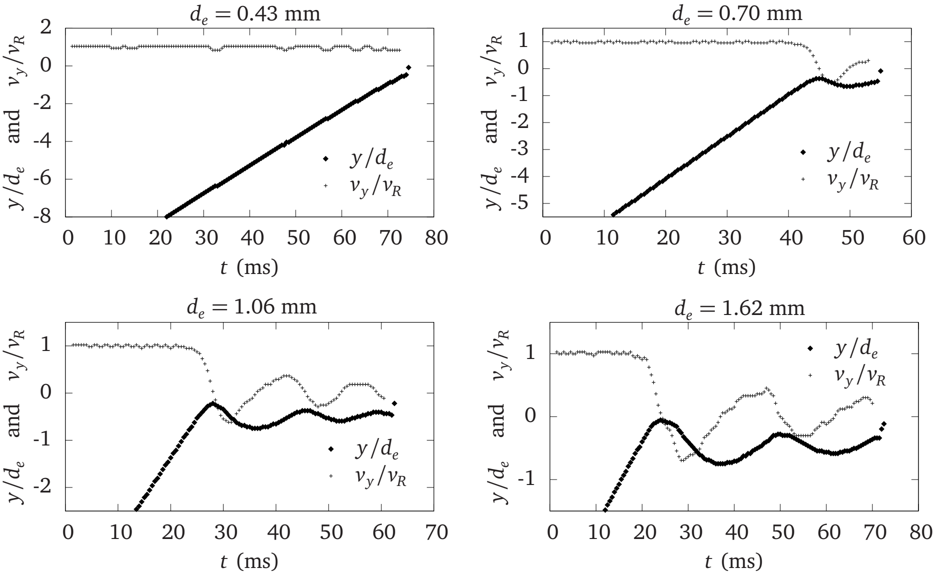

Figure 5.8: Time variation of the normalized position y/d_e and velocity v_y/v_R for four different bubbles.

5.2.2 Bubble center dynamics

The position of different sized bubbles has been measured every 0.5 ms. Instantaneous velocities are calculated using Equation (5.1). The variation of the normalized positions and velocities with time is presented in Figure 5.8 for four sample bubbles with $d_e = 0.43$, 0.70, 1.06 and 1.62 mm. Values of the terminal rise velocities used in the normalization are those shown in Figure 5.2.

Bubbles with an equivalent diameter $d_e < 0.47$ mm rise steadily until they arrive at the free surface. Once the top of the bubble touches the free surface, the bubble coalesces rapidly. Considering that no appreciable deformation of the free surface has been observed for this range of bubble size, it is reasonable to consider the free surface as a flat surface. Moreover, no significant changes in velocity were observed for bubbles with $d_e < 0.47$ mm as they approach the free surface. Thus, the impact velocity can be approximated as the terminal velocity of the bubble. In contrast, bubbles with $d_e \geq 0.47$ mm rise steadily until they arrive at a certain distance (of the same order of d_e) below the free surface, which starts to deform. After the collision with the free surface, bubbles can bounce repeatedly before they coalesce. For the studied range of bubble size, we have observed up to four bounces for larger bubbles ($d_e \approx 2.00$ mm). However, for $d_e \approx 0.70$ mm one single bounce is the usual behavior.

In Figure 5.8, one can observe the bouncing process in four bubbles with different

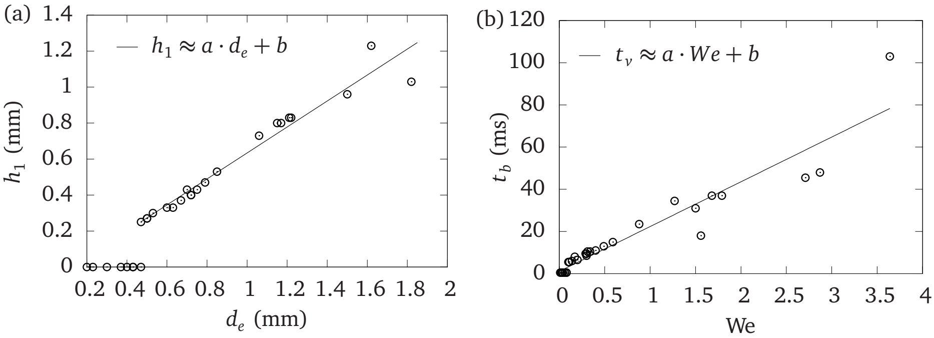

Figure 5.9: (a) First bounce height as a function of bubble equivalent diameter. Linear fit: $a = 0.72 \pm 0.03$; $b = -0.08 \pm 0.04$. (b) Bouncing time as a function of Weber number. Linear fit: $a = 20.7 \pm 1.7$; $b = 2.2 \pm 2.5$.

d_e (time $t = 0$ does not particularly correspond to the time when bubble attains its terminal velocity, but to any non-specific time when the bubble is already in this velocity). There are two main facts to note. First is that the amplitude of the bounce gets higher as the bubble size increases. Second concerns the number of bounces and the bouncing time t_b between the first collision (the first maximum in the bubble position) and coalescence. It can be noted that as bubble size increases, the time t_b also increases.

Figure 5.9(a) shows the height of the first bounce h_1 (first minimum of the position in Figure 5.8) as a function of the bubble equivalent diameter. The behavior is clearly linear in the range studied, although discrepancies from this linearity at higher equivalent diameters are expected due to the effects of gravity force. In the case of large bubble size, gravity force is able to decrease drastically the bubble velocity after the bounce in such a way that large bubbles are not expected to reach bouncing heights larger than d_e. From an energetic point of view, the initial energy of a bubble increases with its size. Assuming that some percentage of this energy is lost in the bounce, the bubble at the lowest point of the bounce will have potential energy and a small amount of surface energy. This potential energy is proportional to the bounce height h_1, so increasing d_e causes an increase in h_1.

In Figure 5.9(b), the values of the bouncing time t_b are plotted as a function of the Weber number. In the studied range, t_b increases linearly with We, and consequently with the square root of the approach velocity. Many authors [SWF05, Dui98, RJM06] have reported that the approach velocity plays a crucial role in the coalescence process. In the present case, the increase of t_b with Weber may be explained by the fact that at low Weber numbers (small approach velocity), the liquid film between the bubble and the free surface is thinnest at the bubble top and gradually becomes thicker toward the periphery. On the other hand, if Weber is increased (higher approach velocity), the liquid film is thicker at the top, creating a dimple. The formation of this dimple is responsible for preventing the bulk of the liquid above the bubble escaping from the liquid film, and therefore inhibiting coalescence. The approach velocity of the bubble will decrease substantially at every bounce, until it has a certain value at which no dimple will be formed, and the bubble will finally coalesce with the free surface.

5.3 Conclusions

The rise, bouncing and coalescence processes of millimetric gas bubbles impacting at a free surface have been studied experimentally.

Single air bubbles were released from a syringe into a methacrylate tank filled with ethanol. The position and shape of the bubbles were measured from the images recorded by means of a high-speed camera.

The main conclusions of this chapter can be summarized in the following points:

- Bubbles with equivalent diameters $d_e < 0.47$ mm rise until they touch the free surface and coalesce with it immediately. In contrast, bubbles with equivalent diameters $d_e > 0.47$ mm bounce repeatedly before the coalescence with the free surface occurs.
- The measured drag coefficient and shape variations of the bubbles showed a good agreement with the available theoretical predictions.
- Time variation of the bubble position and velocity in the bouncing process have been measured, as well as the change of the aspect ratio in the bounce. The movement of the bubble center is found to be similar to that of a damped oscillator.
- Obtained values of the bouncing time increase linearly with the Weber number, and so does the height of the bounce with the bubble equivalent diameter.
- The frequency of the oscillations of the bubble surface caused by the collision of the bubble with the free surface, is not significantly affected by the presence of the free surface.

CHAPTER 6

Conclusions and further work

A brief summary of the main results obtained in this thesis, as well as a description of some of the problems we want to study in the future are presented in this chapter.

Section 6.1.1 gives a general overview of the main conclusions which can be derived from this research. In Section 6.1.2, a summary of the most relevant results for each topic is presented. In Section 6.2, the most important topics or problems we would like to address in the near future are described. Finally, in Section 6.3, some recommendations for further investigations are given.

6.1 Conclusions

6.1.1 General overview

The main objective of this work was to gain more fundamental knowledge on two-phase flow dynamics, by obtaining experimental data in normal gravity and in microgravity conditions. In this research, several experiments and computational simulations have been carried out in an attempt to clarify some of the fundamental aspects of the complex flow created by the two-phase jets. In particular, the study of the structure of single two-phase jets and the behavior of bubbles in the collision region of two impinging jets has been investigated. The interaction of a rising bubble with a free surface has also been studied.

6.1.2 Summary of contributions

6.1.2.1 Two-phase jets

The main contributions on two-phase single jets (air bubbly jets in liquid, and liquid droplet jets in air) are summarized in the following points:

- In a single bubbly jet emerging horizontally from a nozzle in normal gravity conditions, two distinct regions can be observed. A turbulent zone with a conical shape where inertial effects are dominant, and a bubbly plume zone where buoyancy is compensated with the drag force and no coalescences are observed. The separation between the turbulent and bubbly plume regions can be approximated by a straight line, an approximation which is no longer valid in the opposed-jet configuration. The angle forming this straight line with the injection direction decreases as the momentum flux is increased.
- The maximum distance reached by the bubbles in bubbly jets under normal gravity conditions increases as the momentum flux is increased, with a sudden increase at $J \approx 10\ \mathrm{g\,cm/s^2}$ which reflects the transition between the dripping regime and the jetting regime. Concerning the bubble trajectories, a high deceleration is observed near the nozzles for the normal gravity case, while in microgravity, the deceleration is much smoother.
- Injection of liquid through a capillary tube with an increasing flow rate revealed that the transition from dripping regime to jetting regime is independent of the gravity level: when in normal gravity conditions an experimental setup is operating at the dripping regime, a big growing droplet with a nearly spherical shape would be attached to the nozzle in microgravity. On the other hand, when on ground the jetting regime is attained, in absence of gravity the jetting regime will be also found.
- For liquid jets, the transition between the dripping and jetting regime is mainly dominated by the relationship between the inertial and surface forces. In the jetting regime, at the liquid flow rate range investigated, the average breakup length increases as the Weber number is increased. In microgravity this increase can be approximated by a linear relationship.
- The mean size of the droplets resulting from the jet atomization decrease as the liquid flow rate is increased. No significant differences in droplet sizes are observed between the normal gravity case and the microgravity case.

6.1.2.2 Impinging jets

The most relevant contributions on impinging jets are summarized below:

- Bubble velocity field in the opposed-jet arrangement is compared with that of a single jet. Near the injectors, the structure of the velocity field is similar to that of a single jet. However, in the collision zone, the velocity field is highly perturbed by the opposing jet. Comparing to the velocity field of a single jet, a decrease in the velocity in the direction of injection is observed in the central zone of the opposed-jet configuration. The velocity in the vertical direction is highly increased in the central zone, due to the formation of a growing disc with the stagnation point in its center.
- An analysis on the bubble size distribution at different flow rates indicate that the bubble mean size decrease as the momentum flux is increased, both in normal gravity and in microgravity conditions.
- In zero gravity, coalescence events occur mainly near the nozzle and in the collision zone. However, in normal gravity, the coalescences are much more distributed in space. A higher number of coalescences have been observed in microgravity than in the normal gravity case. A possible explanation for this is that in microgravity the probability of collision between two (or more) bubbles is much higher than in normal gravity, since in reduced gravity the bubbles passively follow the liquid flow, with no effects of buoyancy forces. As a result, the relative velocity between bubbles is lower, and numerous bubbles remain quiescent at certain zones of the impinging jets, increasing the probability of collision.
- Numerical simulations revealed that the structure of unbounded impinging single-phase jets adopts the form a cross-like shape, evolving to the deflection instability for separation between jets of $s \geq 9d$, where d is the nozzle diameter. A new kind of instability has been found to appear at $\mathrm{Re} \geq 1000$ for $s = 10d$ in the laminar model. This instability has the form of outflowing waves in the outgoing vertical jets and can be inhibited by turbulent mechanisms.
- Good qualitative agreement between numerical simulations of opposed bubbly jets and the experimental results have been obtained, in terms of the structure of the impinging jets, both in normal gravity and in a reduced gravity environment.

6.1.2.3 Bubble coalescence with a free surface

The main conclusions on the bouncing process of a bubble upon impact with a free surface are presented in the following points:

- There is an abrupt transition between the bouncing/non-bouncing process of a bubble when impacting a free surface: increasing smoothly the bubble diameter does not result in a continuous behavior of the bouncing, if a bubble is below a critical size, it will coalesce directly as soon as it touches the interface. On the other hand, if the bubble size is above a critical size, a bouncing process with non-zero bouncing amplitude will take place prior to coalescence. The nature of this abrupt transition is still not understood (additional experiments are planned to be performed in the near future, and are presented in Section 6.2), but the transition has been found to occur at a critical equivalent diameter of $d_e = 0.47$ mm in ethanol.

- In the bouncing regime, the bouncing time increases linearly with the Weber number, and the height of the first bounce increases linearly with the bubble diameter. This gives an idea of the energy lost in the first bounce for different bubble sizes.

6.2 Future work

We will work in several interesting problems which have already been started during the completion of this thesis. Some of them are in a rather advanced situation, and others will still require dedicating more efforts. A summary of the main work that we have planned to perform in the near future can be divided in the following points:

- This thesis is a compendium of experimental data for certain situations, but sets of higher data consistency are needed: in order to study the effects of a certain parameter, the other parameters present in the problem should be fixed. However, due to experimental unexpected requirements or incidents, this was not always possible. For this reason, the experiments will be carried out using the same liquid and gas flow rates for the normal gravity and microgravity conditions, the same separations, the same impact angle between jets, in the same liquids.
- Concerning the bubble bouncing problem, the recurrent questions are: What are the effects of bubble size and impact velocity on the bouncing/coalescence process? In normal gravity, for a given bubble diameter, the value of the rise velocity is fixed. Nevertheless, by changing the gravity level, a bubble with a fixed size can be forced to reach the free surface at different rise velocities, a value of a rise velocity for each gravity level. In this way, the effect of impact velocity can be investigated for different bubble sizes, and consequently, bubbles with different sizes can be forced to impact the free surface at a fixed velocity. Thus, the effect of bubble size can be studied deeply. However, the creation of a free flat surface in microgravity is highly difficult to achieve. In order to be able to study the effects of bubbles size and velocity on the bouncing problem in a simpler way, the experiment will be performed at the Large Diameter Centrifuge in which gravity levels from 1 g_0 to 20 g_0 can be reached. In

addition, experiments will be carried in fluids with different surface tensions, viscosities and densities.

- Experiments and numerical simulations on impinging droplet jets are planned to be performed in the near future. First of all we will use distilled water as the liquid to study, in order to compare the obtained results with that of a single jet. Nevertheless, experiments using different liquids with different physical properties (surface tension, viscosity and density) will be performed.

6.3 Recommendations for further investigations

One of the major problems we had when designing the bubbly jet impingement experiment, was to divide in equal parts the flow rate from one pipe into two pipes, for both for the gas line, and the liquid line. Since the bubbly jets are highly sensitive to flow rates, if the gas and liquid flow rates do not have the same exact value, the jets are not symmetric. Moreover, the symmetric state is not “stable”: if the jets are not symmetric due to different flow rates coming from the pipes for each injector, this “asymmetry” tends to increase with time. The solution we adopted was to use 4 valves (2 for the liquid line, and 2 for the gas line) with variable aperture. We had to manually adjust the aperture of each valve in order to create symmetric jets, for each set of flow rates we used. This solution is not perfect, but worked fine in the range of flow rates that were studied. Another solution is to use two liquid pumps and two pressurized gas tanks, however this solution may not be possible due to power consumption requirements, and space or weight restrictions. Thus, thinking about various methods to equally divide the flow between two sub-lines is recommended.

When designing the impinging jets experiment, we were not aware of the negative g-levels that are reached at the first milliseconds after capsule release. We designed a system to remove the residual bubbles from the top of the tank (by building the top with an angle that drove the bubbles into the residual tank in normal gravity), but, the value of this angle was too low. Hence, the bubbles had some milli- or centi-seconds of travel from when they reached the top until they were at the outlet orifice. This little amount of time was high enough to make the bubbles go into the region of interest, when the negative values of the g-level were reached. For this reason, we had big bubbles that perturbed the whole flow field. Thus, thinking about how to remove big bubbles from the top of the tank is highly recommended.

Since the most relevant data obtained in all the experiments described in this research are the high-speed movies, I recommend using the highest homogeneous background as possible, which can be obtained by high illumination and effective diffusion of the light. One of the problems to keep in mind with the high-speed camera is that in most of the experiments with bubbly jets, a region of 100×100 mm^2 needed to be recorded, however the mean bubble diameter was of the order of 1 mm, thus a single bubble spans over 5 or 6 pixels, which is a very low resolution. This low resolution could be improved by reducing the separation between the impinging jets, or with the use of different lenses placed at different regions of the impinging jets.

Finally, another difficulty we had to face was in the creation of small bubbles in the experiment of bubble coalescence with a free surface. The difficulty was not in how to create a bubble at a desired size, but how to detach the bubble from the nozzle tip. As the bubble grows, it remains attached to the tip of the syringe until a critical diameter (when the buoyancy force equals to the attachment force) is reached. At this moment, the bubble detaches from the nozzle and rises (following a straight path, or an helical path) to the free surface due to gravity. However, bubbles smaller than this critical diameter were needed, so a detachment method needed to be implemented. The solution we adopted was to create the bubble at a desired size, and detach it from the nozzle using a co-flow of liquid, assuring that the bubble rose in the region in which the camera was recording. This is an important point to account for, and the reader may want to think about that if some similar experiments have been planned.

APPENDIX $\mathcal{A}$

Analytical solutions for incompressible jet flows

A.1 Velocity field for the steady non-linear case

In order to obtain the steady velocity distribution for a non-linear single-phase jet, we follow the procedure detailed in Schlichting [Sch79], which is based on the assumption that the kinematic viscosity ν is constant over the whole of the jet. The pressure gradient $\partial p/\partial \ell$ in the ℓ-direction can be neglected, because the constant pressure in the surrounding fluid impresses itself on the jet. Owing to the assumption of a constant pressure, the momentum flux in the ℓ-direction is constant,

$$J = \rho \int_0^\infty v_\ell^2 r dr d\phi = 2\pi\rho \int_0^\infty r v_\ell^2 dr = \text{constant}. \tag{A.1}$$

In the adopted system of coordinates (see Figure A.1), the equation of motion can be written as

$$v_\ell \frac{\partial v_\ell}{\partial \ell} + v_r \frac{\partial v_\ell}{\partial r} = \nu \frac{1}{r}\frac{\partial}{\partial r}\left(r \frac{\partial v_\ell}{\partial r}\right), \tag{A.2}$$

$$\frac{\partial v_\ell}{\partial \ell} + \frac{\partial v_r}{\partial r} + \frac{v_r}{r} = 0, \tag{A.3}$$

with the following boundary conditions:

- $r = 0: \quad v_r = 0, \quad \partial v_\ell/\partial r = 0,$

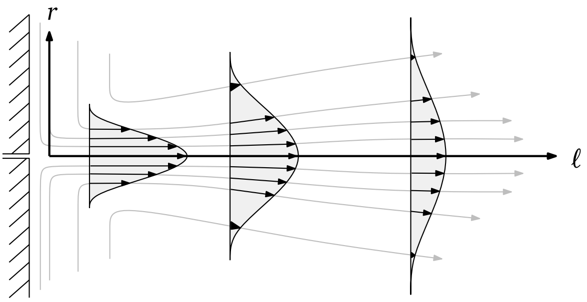

Figure A.1: The axisymmetric jet flow with the system of coordinates.

- $r = \infty$: $v_\ell = 0$.

Since the problem as a whole possesses no characteristic linear dimension, we shall assume that the velocity profiles $v_\ell(\ell, r)$ are similar. Additionally, we will also assume that the velocity v_ℓ is a function of r/q, where q is the width of the jet. Assuming that the width of the jet is proportional to ℓ^n, we can write the stream function ψ in the form

$$\psi \sim \ell^p F\left(\frac{r}{q}\right) = \ell^p F\left(\frac{r}{\ell^n}\right). \tag{A.4}$$

With the aim to determine the exponents p and n, we will use two conditions: first, the fact that the momentum flux must be independent of ℓ (from Equation A.1), and secondly, the inertia and frictional terms in Equation A.2 must be of the same order of magnitude. With this,

$$v_\ell \sim \ell^{p-2n}, \quad \frac{\partial v_\ell}{\partial \ell} \sim \ell^{p-2n-1}, \quad \frac{\partial v_\ell}{\partial r} \sim \ell^{p-3n}, \quad \frac{1}{r}\frac{\partial}{\partial r}\left(r\frac{\partial v_\ell}{\partial r}\right) \sim \ell^{p-4n}. \tag{A.5}$$

Thus the equations for p and n can be written

$$2p - 4n + 2n = 0, \quad 2p - 4n - 1 = p - 4n. \tag{A.6}$$

From these, we obtain that $p = n = 1$, and we can write the stream function as

$$\psi = \nu \ell F(\eta), \quad \text{with} \quad \eta = \frac{r}{\ell}, \tag{A.7}$$

from which the velocity components can be obtained

$$v_\ell = \frac{\nu}{\ell}\frac{F'}{\eta}, \quad v_r = \frac{\nu}{\ell}\left(F' - \frac{F}{\eta}\right). \tag{A.8}$$

Using the above expressions into Equation A.2, we obtain the following equation for

F

$$\frac{FF'}{\eta^2} - \frac{F'^2}{\eta} - \frac{FF''}{\eta} = \frac{d}{d\eta}\left(F'' - \frac{F'}{\eta}\right). \tag{A.9}$$

Equation A.9 can be integrated once, resulting in

$$FF' = F' - \eta F''. \tag{A.10}$$

For $r = 0$, the boundary conditions are $v_\ell =$ constant and $v_r = 0$. Hence, $F' = 0$ and $F = 0$ for $\eta = 0$. Since v_ℓ is an even function of η, F'/η is even, F' odd and F even. Since $F(0) = 0$, the constant term in the expansion of F in powers of η is zero, which determines one constant of integration. The second constant of integration (denoted here by γ) can be evaluated as follows: If $F(\eta)$ is a solution of Equation A.10, then $F(\gamma\eta) = F(\xi)$ is also a solution. A particular solution of the differential equation

$$F\frac{dF}{d\xi} = \frac{dF}{d\xi} - \xi\frac{d^2F}{d\xi^2} \tag{A.11}$$

which satisfies the boundary condition $\xi = 0 : \quad F = 0, \quad F' = 0$, is given by

$$F = \frac{\xi^2}{1 + \frac{1}{4}\xi^2}. \tag{A.12}$$

With this, we obtain from Equation A.8

$$v_\ell = \frac{v}{\ell}\gamma^2\frac{1}{\xi}\frac{dF}{d\xi} = \frac{v}{\ell}\frac{2\gamma^2}{\left(1 + \frac{1}{4}\xi^2\right)^2}, \tag{A.13}$$

$$v_r = \frac{v}{\ell}\gamma\left(\frac{dF}{d\xi} - \frac{F}{\xi}\right) = \frac{v}{\ell}\gamma\frac{\xi - \frac{1}{4}\xi^3}{\left(1 + \frac{1}{4}\xi^2\right)^2}. \tag{A.14}$$

We have $\xi = \gamma r \ell$, and the constant of integration γ can now be determined from the given value of momentum. From Equation A.1, we obtain

$$J = 2\pi\rho\int_0^\infty r v_\ell^2 dr = \frac{16}{3}\pi\rho\gamma^2 v^2. \tag{A.15}$$

Finally, with the above results, one can obtain the velocity profiles

$$v_\ell = \frac{3}{8\pi\nu}\frac{J}{\rho}\frac{1}{\left(1+\frac{1}{4}\xi^2\right)^2}\frac{1}{\ell}, \tag{A.16}$$

$$v_r = \frac{1}{4}\sqrt{\frac{3J}{\pi\rho}}\frac{\xi-\frac{1}{4}\xi^3}{\left(1+\frac{1}{4}\xi^2\right)^2}\frac{1}{\ell}, \tag{A.17}$$

$$\xi = \frac{1}{4\nu}\sqrt{\frac{3J}{\pi\rho}}\frac{r}{\ell}. \tag{A.18}$$

The solution above is valid both for the laminar case and the turbulent case, provided one uses the turbulent kinematic viscosity ν_T instead of the usual kinematic viscosity ν.

APPENDIX B

Governing equations and algorithms used in the numerical simulations

B.1 Single-phase opposed-jet flow

B.1.1 Laminar flows

In the case of isothermal and incompressible flows, the fluid motion is governed by the balance of momentum and mass. For laminar flows, the balance equations can be written as

$$\frac{\partial \vec{v}}{\partial t} + \left(\vec{v} \cdot \vec{\nabla}\right) \vec{v} = -\frac{1}{\rho} \vec{\nabla} p + \mu \nabla^2 \vec{v} + \vec{f}, \tag{B.1}$$

$$\vec{\nabla} \cdot \vec{v} = 0, \tag{B.2}$$

where $\vec{v}$ is the velocity field, p is the pressure field, $\vec{f}$ is an external force, ρ is the fluid density and μ is the fluid viscosity.

It is convenient to express the governing equations in dimensionless form. The dimensionless parameters are introduced: $\vec{x}' = \vec{x}/d$, $\vec{x}' = \vec{v}/u$, $t' = tu/d$, $p' = p/\rho u^2$, $\vec{f}' = \vec{f} d/\rho u^2$, where d, u and ρ are the scaling parameters. Introducing the Reynolds number, $\mathrm{Re} = \rho d u/\mu$, the balance equations can be written in dimensionless form as

$$\frac{\partial \vec{v}'}{\partial t'} + \left(\vec{v}' \cdot \vec{\nabla}'\right) \vec{v}' = -\vec{\nabla}' p' + \frac{1}{\mathrm{Re}} \nabla'^2 \vec{v}' + \vec{f}', \tag{B.3}$$

$$\vec{\nabla}' \cdot \vec{v}' = 0. \tag{B.4}$$

From now on, we will assume that we work in dimensionless variables so we will drop the primes.

In the present study, we restrict ourselves to the two-dimensional case without external force, $\vec{f} = 0$, thus the balance equations can be written as

$$\frac{\partial v_x}{\partial t} + v_x \frac{\partial v_x}{\partial x} + v_y \frac{\partial v_x}{\partial y} = -\frac{\partial p}{\partial x} + \frac{1}{\mathrm{Re}} \left(\frac{\partial^2 v_x}{\partial x^2} + \frac{\partial^2 v_x}{\partial y^2} \right), \tag{B.5}$$

$$\frac{\partial v_y}{\partial t} + v_x \frac{\partial v_y}{\partial x} + v_y \frac{\partial v_y}{\partial y} = -\frac{\partial p}{\partial y} + \frac{1}{\mathrm{Re}} \left(\frac{\partial^2 v_y}{\partial x^2} + \frac{\partial^2 v_y}{\partial y^2} \right), \tag{B.6}$$

$$\frac{\partial v_x}{\partial x} + \frac{\partial v_y}{\partial y} = 0.. \tag{B.7}$$

where a cartesian coordinate system has been used.

B.1.2 Turbulent flows

The balance equations for the turbulent flows are the same as the ones for the laminar flows (Equations B.1 and B.2), with an additional term proportional to the eddy viscosity μ_T. Changing μ from Equation B.1 to $\mu_L + \mu_T$, one obtains the turbulent balance equations

$$\frac{\partial \vec{v}}{\partial t} + \left(\vec{v} \cdot \vec{\nabla} \right) \vec{v} = -\frac{1}{\rho} \vec{\nabla} p + \left(\mu_L + \mu_T \right) \nabla^2 \vec{v} + \vec{f}, \tag{B.8}$$

$$\vec{\nabla} \cdot \vec{v} = 0, \tag{B.9}$$

where the subscripts L and T stand for “laminar” and “turbulent” respectively.

The eddy viscosity μ_T can be determined from physical and dimensional arguments as

$$\mu_T = C_\mu \frac{\rho k^2}{\varepsilon}, \tag{B.10}$$

where $C_\mu = 0.09$ is a constant of the model, k is the turbulent kinetic energy and ε is the turbulent dissipation. Now, the closure equations for k and ε are needed.

The turbulence model used in this study is a variant of the $k - \varepsilon$ model, the so-called “Chen and Kim model” [CK87, KW04], which becomes appropriate for this kind of flows and in which an additional production timescale is introduced (the last term of Equation B.13). Within the Chen and Kim model, the equation for the turbulent kinetic energy k can be written as

$$\frac{\partial \left(\rho k \right)}{\partial t} + \vec{\nabla} \cdot \left(\rho k \vec{v} \right) = \vec{\nabla} \left[\left(\mu_L + \frac{\mu_T}{\sigma_k} \right) \vec{\nabla} k \right] - \rho \varepsilon + 2 \mu_T S_{ij} S_{ij}, \tag{B.11}$$

where $\sigma_k = 0.75$ is a constant and S_{ij} is the rate-of-strain tensor

$$S_{ij} = \frac{1}{2}\left(\frac{\partial v_j}{\partial x_i} + \frac{\partial v_i}{\partial x_j}\right). \tag{B.12}$$

The equation for the turbulent dissipation ε can be written as

$$\begin{aligned}\frac{\partial(\rho\varepsilon)}{\partial t} + \vec{\nabla}\cdot(\rho\varepsilon\vec{v}) = \vec{\nabla}\left[\left(\mu_L + \frac{\mu_T}{\sigma_\varepsilon}\right)\vec{\nabla}\varepsilon\right] - \\ - C_{1\varepsilon}\frac{\varepsilon}{k}2\mu_T S_{ij}S_{ij} + C_{2\varepsilon}\rho\frac{\varepsilon^2}{k} + \frac{\mu_T^2}{\rho k}\left(S_{ij}S_{ij}\right)^2,\end{aligned} \tag{B.13}$$

where $\sigma_\varepsilon = 1.15$, $C_{1\varepsilon} = 1.15$ and $C_{2\varepsilon} = 1.9$ are constants of the model. The last term on the right-hand side of Equation B.13 contains the production timescale and marks the difference between the Chen and Kim model and the standard $k-\varepsilon$ model.

B.2 Bubbly opposed-jet flow

B.2.1 General equations

The conservation equations for single-phase flows can be written in the general form

$$\frac{\partial(\rho\phi)}{\partial t} + \vec{\nabla}\cdot\left[\rho\vec{v}\phi - \Gamma_\phi\vec{\nabla}\phi\right] = S_\phi, \tag{B.14}$$

where ϕ is any variable (scalar or vector), ρ is the fluid density, $\vec{v}$ is the velocity, Γ_ϕ is the diffusion coefficient of ϕ and S_ϕ is a source of ϕ.

Setting $\phi = 1$, $\Gamma_\phi = 0$ and $S_\phi = 0$, one obtains the continuity equation,

$$\frac{\partial\rho}{\partial t} + \vec{\nabla}\cdot(\rho\vec{v}) = 0. \tag{B.15}$$

Setting $\phi = \vec{v}$, $\Gamma_\phi = \rho\left(\nu_L + \nu_T\right)$ and $S_\phi = -\vec{\nabla}p$, one obtains the momentum equations,

$$\frac{\partial(\rho\vec{v})}{\partial t} + \vec{\nabla}\cdot\left[\rho\vec{v}\vec{v} - \rho\left(\nu_L + \nu_T\right)\vec{\nabla}\vec{v}\right] = -\vec{\nabla}p. \tag{B.16}$$

where $\vec{x}\vec{y}$ is the dyadic product between vectors $\vec{x}$ and $\vec{y}$, ν_L and ν_T are are the laminar and turbulent viscosities respectively.

Dealing with multiphase flows, one needs to compute, at least, the velocity components and the volume fraction for each phase. In order to do this, the method used in this study is the so-called IPSA[1], which solves the equations for each phase

---

[1] Inter-Phase Slip Algorithm

using Eulerian-Eulerian techniques in a fixed grid. The IPSA procedure is based on an iterative method, operating on finite-difference equations connecting the values of variables pertaining to points arrayed on a cartesian grid. The method can solve steady and transient processes, and the fluids may be compressible or incompressible. In addition, buoyancy, phase-change and chemical-reaction effects can be handled using the IPSA method.

In order to take into account the multiple phases, a generalized form of Equation B.14 can be written

$$\frac{\partial\left(f_i\rho_i\phi_i\right)}{\partial t}+\vec{\nabla}\cdot\left(f_i\rho_i\vec{v}_i\phi_i-f_i\Gamma_{\phi_i}\vec{\nabla}\phi_i-\phi_i\Gamma_{f_i}\vec{\nabla}f_i\right)=S_i+S_{ip} \tag{B.17}$$

where i is the index of the phase (for two-phase flows, $i=1,2$), f_i is the volume fraction of phase i, Γ_{ϕ_i} is the within-phase diffusion coefficient, Γ_{f_i} is the phase diffusion coefficient, S_i are the within-phase volumetric sources and S_{ip} are the inter-phase volumetric sources. As the phases completely fill the available space, the volume fractions must sum to unity, $\sum_i f_i=1$.

The algorithm solves the momentum equations for each phase independently, and the links between phases are introduced via an inter-phase source. Pressure is common in both phases.

Setting $\phi_i=1$ $(i=1,2)$, and the diffusion and source terms equal to zero, one obtains the continuity equation for each phase.

Setting $\phi_i=\vec{v}_i$, $\Gamma_{\phi_i}=\rho_i\left(\nu_L+\nu_T\right)$, $S_i=-\vec{\nabla}p+\Delta\rho\vec{g}$ and $S_{ip}=\delta_s\gamma\kappa\vec{n}$ (where δ_s is the Dirac delta function centered at the interphase, and $kappa$ is the local curvature), one obtains the momentum equations, where $\Delta\rho=\left(\rho_1-\rho_2\right)$, $\vec{g}$ is the acceleration of gravity, and σ is the surface tension between the two phases. Hence, for each phase the momentum equations become

$$\rho\left[\frac{\partial\vec{v}}{\partial t}+\left(\vec{v}\cdot\vec{\nabla}\right)\vec{v}\right]=-\vec{\nabla}p+\mu\nabla^2\vec{v}+\Delta\rho\vec{g}+\gamma\kappa\vec{n}\delta_s. \tag{B.18}$$

In order to write the equations in dimensionless form, we introduce the following non-dimensional quantities: $\vec{x}'\equiv\vec{x}/L_0$, $\vec{v}'\equiv\vec{v}/v_0$, $\rho'\equiv\rho/\rho_0$, $\mu'\equiv\mu/\mu_0$, $\gamma'\equiv\gamma/\gamma_0$, $\vec{g}'\equiv\vec{g}/g_0$. Here, L_0, v_0, ρ_0 are arbitrary values taken as reference parameters. Then, the time can be written as $t=L_0/v_0t'$ and the pressure $p=\rho_0v_0^2p'$. Substitution of these parameters into Equation B.18, and rearranging terms, the dimensionless momentum equations become

$$\frac{\partial\vec{v}}{\partial t}+\left(\vec{v}\cdot\vec{\nabla}\right)\vec{v}=-\vec{\nabla}p+\frac{1}{\mathrm{Re}}\nabla^2\vec{v}+\frac{1}{\mathrm{Fr}^{*2}}+\frac{1}{\mathrm{We}}\kappa\vec{n}\delta_s \tag{B.19}$$

where the primes (′) have been dropped, and the following dimensionless numbers have been introduced,

$$\mathrm{Re} = \frac{\rho_0 v_0 L_0}{\mu_0}, \tag{B.20}$$

$$\mathrm{Fr}^* = \frac{v_0}{\sqrt{g^* L_0}} \qquad (\text{with } \vec{g}^* = \frac{\Delta\rho}{\rho}\vec{g}), \tag{B.21}$$

$$\mathrm{We} = \frac{\rho_0 v_0^2 L_0}{\gamma_0}. \tag{B.22}$$

which are the Reynolds, Froude, and Weber numbers respectively.

B.2.2 Turbulence model

The turbulence model used in this study is the same as in the single-phase case, the Chen and Kim model, described in Section B.1.2.

B.3 Main solver algorithm

The governing equations have been discretized and solved by means of the commercial software PHOENICS-2009, using the finite volume method in conjunction with the SIMPLEST algorithm (Spalding, [Spa80]), which is a variant of the SIMPLE algorithm. The main steps in both SIMPLE and SIMPLEST algorithm are:

1. Assume an initial pressure field distribution.
2. Solve the momentum equations using this pressure field, thus obtaining velocities which satisfy momentum but not necessarily continuity.
3. Construct continuity errors for each cell.
4. Solve the pressure-correction equation and adjust the pressure field correspondingly.
5. Adjust the velocity field by $v_{new} = v_{old} + (\partial v/\partial p)\delta p$. Hence, the new velocities satisfy continuity but not necessarily momentum balance.
6. Go back to step 2, and repeat with the new pressure field.
7. Repeat until continuity and momentum errors are acceptably small.

The SIMPLEST algorithm differs from SIMPLE in the way that the discretized momentum equations are manipulated, so that the SIMPLEST velocity correction formulas omit terms that are less significant than those omitted in SIMPLE algorithm. As a result, it produces convergence much smoothly than SIMPLE, and with less under-relaxation.

B.4 Differencing Scheme

Let ϕ_A, ϕ_B and ϕ_C be the values of a certain magnitude ϕ measured at the center of the cells A, B and C respectively. It is assumed that the flow is from A to C. The value of ϕ at the face between the cells B and C, is computed by

$$\phi_f = \phi_A + \frac{1}{2} B(r) \left(\phi_B - \phi_A \right), \tag{B.23}$$

where ϕ_f is the value of ϕ at the cell face, and r is defined as $r = (\phi_C - \phi_B)/(\phi_B - \phi_A)$. If $B(r) = 0$, we recover a linear upwind differencing scheme. If $B(r) = r$, we recover the linear central difference scheme. Throughout all this study, the non-linear CHARM differencing scheme has been used, which is based on a quadratic upwind scheme with

$$B(r) = \begin{cases} \frac{r(3r+1)}{(r+1)^2} & \text{for } r > 0, \\ 0 & \text{for } r \leq 0. \end{cases} \tag{B.24}$$

Within this non-linear differencing scheme, the numerical diffusion is reduced significantly.

Bibliography

[AGCR⁺10] S. Arias, R. González-Cinca, X. Ruiz, L. Ramírez-Piscina, and J. Casademunt. Characterization of the performance of a minibubble generator in conditions relevant to microgravity. *Colloids and Surfaces A: Physicochemical and Engineering Aspects*, 365:52–55, 2010. 67

[AMS02] S. V. Alekseenko, D. M. Markovich, and V. I. Semenov. Turbulent structure of a gas-liquid impinging jet. *Fluid Dynamics*, 37:684–694, 2002. 7

[ARC⁺09] S. Arias, X. Ruiz, J. Casademunt, L. Ramírez-Piscina, and R. González-Cinca. Experimental study of a microchannel bubble injector for microgravity applications. *Microgravity Science and Technology*, 21:107–111, 2009. 15, 62, 67

[AVP95] Ya. D. Afanasyev, S. I. Voropayev, and P. G. Potylitsin. Interaction of vortex dipoles: The theory and laboratory experiment. *Atmosferic and Oceanic Physics*, 30(5):665–672, 1995. 7, 80

[Bat67] G.K. Batchelor. *An Introduction to Fluid Dynamics*. Cambridge University Press, 1967. 103

[bCTC05] Edited by Clayton T. Crowe. *Multiphase Flow Handbook*. CRC Press, 2005. 1, 2, 5

[BD01] G. Bozzano and M. Dente. Shape and terminal velocity of single bubble motion: a novel approach. *Computers & Chemical Engineering*, 25(4-6):571 – 576, 2001. 8

[Bre05] Christopher E. Brennen. *Fundamentals of Multiphase Flows*. Cambridge University Press, 2005. 1, 2

[Bus04] J.W.M. Bush. Mit lecture notes on surface tension, lecture 5. Massachussets Institute of Technology, 2004. 39

[CC06] Rong-Horng Chen and Chiu-Ting Chen. Collision between immiscible drops with large surface tension difference: diesel oil and water. *Experiments in Fluids*, 41:453–461, 2006. 47

[CCJM04] C. P. Chou, J. Y. Chen, J. Janicka, and E. Mastorakos. Modeling of turbulent opposed-jet mixing flows with - model and second-order closure. *International Journal of Heat and Mass Transfer*, 47(5):1023 – 1035, 2004. 7

[CF95] C. Colin and J. Fabre. Gas-liquid pipe flow under microgravity conditions: Influence of tube diameter on flow patterns and pressure drops. *Advances in Space Research*, 16(7):137 – 142, 1995. Microgravity Sciences: Results and Analysis of Recent Spaceflights. 2

[CGW05] R. Clift, J. R. Grace, and M. E. Weber. *Bubbles, Drops, and Particles*. Dover Publications, 2005. 2, 5

[Che91] A.K. Chesters. The modeling of coalescence process in fluid-liquid dispersions: a review of current understanding. *Trans. I. Chem. E.*, 69(A4):259–270, 1991. 5, 61

[CK87] Y. S. Chen and S. W. Kim. Computation of turbulent flows using and extended $k-\varepsilon$ turbulence closure model. Technical Report NASA CR-179204, 1987. 124

[CL93] Michel Champion and Paul A. Libby. Reynolds stress description of opposed and impinging turbulent jets. part i: Closely spaced opposed jets. *Physics of Fluids A: Fluid Dynamics*, 5(1):203–216, 1993. 7

[CPG06] J. Carrera, R.N. Parthasarathy, and S.R. Gollahalli. Bubble formation from a free-standing tube in microgravity. *Chemical Engineering Science*, 61(21):7007 – 7018, 2006. xvii, 3, 14

[CRF08] Catherine Colin, Xavier Riou, and Jean Fabre. Bubble coalescence in gas-liquid flow at microgravity conditions. *Microgravity Science and Technology*, 20:243–246, 2008. 61

[CRRP$^+$08] J. Carrera, X. Ruiz, L. Ramírez-Piscina, J. Casademunt, and M. Dreyer. Generation of a monodisperse microbubble jet in microgravity. *AIAA Journal*, 46:2010–2019, 2008. xvii, 6, 13, 14, 15, 57, 58, 63

[DL08] Bing Dai and L. Gary Leal. The mechanism of surfactant effects on drop coalescence. *Physics of Fluids*, 20(4):040802, 2008. 9

[Dui98] P. C. Duineveld. Bouncing and coalescence of bubble pairs rising at high reynolds number in pure water or aqueous surfactant solutions. *Applied Scientific Research*, 58:409 – 439, 1998. 5, 9, 110

[dVBvW02] A. W. G. de Vries, A. Biesheuvel, and L. van Wijngaarden. Notes on the path and wake of a gas bubble rising in pure water. *International Journal of Multiphase Flow*, 28(11):1823 – 1835, 2002. 8

[dVLL02] J. de Vries, S. Luther, and D. Lohse. Induced bubble shape oscillations and their impact on the rise velocity. *The European Physical Journal B - Condensed Matter and Complex Systems*, 29:503–509, 2002. 8, 103

[ECCJ00] J. Eckestein, J.-Y. Chen, C.-P. Chou, and J. Janicka. Modeling of turbulent mixing in opposed jet configuration: one-dimensional monte carlo probability density function simulation. *Proceedings of the Combustion Institute*, 28:141–148, 2000. 7

[EP50] P. S. Epstein and M. S. Plesset. On the stability of gas bubbles in liquid-gas solutions. *Journal of Chemical Physics*, 18:1505–1509, 1950. 62

[EV08] Jens Eggers and Emmanuel Villermaux. Physics of liquid jets. *Reports on Progress in Physics*, 71(3):036601, 2008. 7

[FVN95] L. E. Freed and G. Vunjak-Novakovic. Cultivation of cell–polymer tissue constructs in simulated microgravity. *Biotechnology and Bioengineering*, 46(4):306–313, 1995. 5

[FVN97] Lisa Freed and Gordana Vunjak-Novakovic. Microgravity tissue engineering. *In Vitro Cellular & Developmental Biology - Animal*, 33:381–385, 1997. 5

[Gab07] Kamiel Gabriel. *Microgravity Two-phase Flow and Heat-transfer*. Space Technology Library, Springer, 2007. 2, 4

[GCPL05] T.-C. Gao, R.-H. Chen, J.-Y. Pu, and T.-H. Lin. Collision between an ethanol drop and a water drop. *Experiments in Fluids*, 38:731–738, 2005. 47

[Gho04] P. Ghosh. Coalescence of air bubbles at air-water interface. *Chemical Engineering Research and Design*, 82(7):849 – 854, 2004. 9

[GM66] Rollin Peter Grant and Stanley Middleman. Newtonian jet stability. *AIChE Journal*, 12(4):669 – 678, 1966. 42, 43

[HBC+10] Kathryn Hurlbert, Bob Bagdigian, Carol Carroll, Antony Jeevarajan, Mark Kliss, and Bhim Singh. Human health, life support and habitation systems roadmap (draft). *NASA Space Technology Roadmaps*, November 2010. 5

[HCT+09] Yu-Shik Hwang, Johann Cho, Feng Tay, Jerry Y.Y. Heng, Raimundo Ho, Sergei G. Kazarian, Daryl R. Williams, Aldo R. Boccaccini, Julia M. Polak, and Athanasios Mantalaris. The use of murine embryonic stem cells, alginate encapsulation, and rotary microgravity bioreactor in bone tissue engineering. *Biomaterials*, 30(4):499 – 507, 2009. 5

[HKM+10] Scott A. Hill, Christopher Kostyk, Brian Motil, William Notardonato, Steven Rickman, and Theodore Swanson. Thermal management systems roadmap (draft). *NASA Space Technology Roadmaps*, November 2010. 4

[IH06] Mamoru Ishii and Takashi Hibiki. *Thermo-fluid Dynamics of Two-Phase Flow*. Springer, 2006. 2

[ITS+97] M. Ingram, G. Techy, R. Saroufeem, O. Yazan, K. Narayan, T. Goodwin, and G. Spaulding. Three-dimensional growth patterns of various human tumor cell lines in simulated microgravity of a nasa bioreactor. *In Vitro Cellular & Developmental Biology - Animal*, 33:459–466, 1997. 5

[KAL+10] Kriss J. Kennedy, Leslie Alexander, Rob Landis, Diane Linne, Carole Mclemore, and Edgardo Santiago-Maldonado. Human exploration destination systems roadmap (draft). *NASA Space Technology Roadmaps*, November 2010. 5

[KCCF01] A. M. Kamp, A. K. Chesters, C. Colin, and J. Fabre. Bubble coalescence in turbulent flows: A mechanistic model for turbulence-induced coalescence applied to microgravity bubbly pipe flow. *International Journal of Multiphase Flow*, 27(8):1363 – 1396, 2001. 3, 5, 61, 62, 67

[KCM+01] Evert Klaseboer, Jean-Philippe Chevaillier, Annie Maté, Olivier Masbernat, and Christophe Gourdon. Model and experiments of a drop impinging on an immersed wall. *Physics of Fluids*, 13(1):45–57, 2001. 9

[KEEE08] Aysel Koç, Nuray Emin, A. Eser Elçin, and Y. Murat Elçin. In vitro osteogenic differentiation of rat mesenchymal stem cells in a microgravity bioreactor. *Journal of Bioactive and Compatible Polymers*, 23(3):244–261, 2008. 5

[KK93] V. Kumaran and Donald L. Koch. The rate of coalescence in a suspension of high reynolds number, low weber number bubbles. *Physics of Fluids A: Fluid Dynamics*, 5(5):1135–1140, 1993. 9

[KKM03] M. Krasowska, M. Krzan, and K. Malysa. Bubble collisions with hydrophobic and hydrophilic surfaces in a-terpineol solutions. *Physicochemical Problems of Mineral Processing*, 37:37–50, 2003. 9

[KKO94] Ieehwan Kim, Yasuhiro Kamotani, and Simon Ostrach. Modeling bubble and drop formation in flowing liquids in microgravity. *AIChE Journal*, 40(1):19–28, 1994. 3

[Kle03] Cl Kleinstreuer. *Two-Phase Flow: Theory and Applications*. Taylor & Francis, 2003. 2

[KLM03] M. Krzan, K. Lunkenheimer, and K. Malysa. Pulsation and bouncing of a bubble prior to rupture and/or film formation. *Langmuir*, 19(17):6585 – 6589, 2003. 9

[KR05] Gwon Hyun Ko and Hong Sun Ryou. Modeling of droplet collision-induced breakup process. *International Journal of Multiphase Flow*, 31(6):723 – 738, 2005. 47

[KS93] Brenda J. Klement and Brian S. Spooner. Utilization of microgravity bioreactors for differentiation of mammalian skeletal tissue. *Journal of Cellular Biochemistry*, 51(3):252–256, 1993. 5

[KW04] E. Korusoy and J. H. Whitelaw. Inviscid, laminar and turbulent opposed flows. *International Journal for Numerical Methods in Fluids*, 46(11):1069 – 1098, 2004. 124

[Lam32] H. Lamb. *Hydrodynamics. Sixth Edition*. Cambridge University Press, 1932. 50, 108

[LDG05] Dominique Legendre, Claude Daniel, and Pascal Guiraud. Experimental study of a drop bouncing on a wall in a liquid. *Physics of Fluids*, 17(9):097105, 2005. 9, 102

[LE97] Stig Ljunggren and Jan Christer Eriksson. The lifetime of a colloid-sized gas bubble in water and the cause of the hydrophobic attraction. *Colloids and Surfaces A: Physicochemical and Engineering Aspects*, 129-130:151 – 155, 1997. Prof. B. W. Ninham. 62

[Lef89] A.H. Lefebvre. *Atomization and sprays*. Hemisphere Publishing Corporation, 1989. 39, 50

[LEG87] C.-H. Lee, L.E. Erickson, and L.A. Glasgow. Bubble breakup and coalescence in turbulent gas-liquid dispersion. *Chem. Eng. Commun.*, 59:65–84, 1987. 61

[LGH$^+$10] Valerie J. Lyons, Guillermo A. Gonzalez, Michael G. Houts, Christopher J. Iannello, John H. Scott, and Subbarao Surampudi. Space power and energy storage roadmap (draft). *NASA Space Technology Roadmaps*, November 2010. 4

[LMC93] Marian L. Lewis, Debra M. Moriarity, and P. Samuel Campbell. Use of microgravity bioreactors for development of an in vitro rat salivary gland cell culture model. *Journal of Cellular Biochemistry*, 51(3):265–273, 1993. 5

[LMM02] F. Lehr, M. Millies, and D. Mewes. Bubble size distributions and flow fields in bubble columns. *AIChE Journal*, 48(11):2426–2443, 2002. 61

[Lot08] E. Loth. Quasi-steady shape and drag of deformable bubbles and drops. *International Journal of Multiphase Flow*, 34(6):523 – 546, 2008. 8, 102, 103, 105

[LR98] S. P. Lin and R. D. Reitz. Drop and spray formation from a liquid jet. *Annual Review of Fluid Mechanics*, 30(1):85–105, 1998. 7

[LS96] H. Luo and H.F. Svendsen. Theoretical model for drop and bubble breakup in turbulent dispersions. *AIChE Journal*, 42(5):1225–1233, 1996. 61

[LS99] D. C. Lowe and Rezkallah K. S. Flow regime identification in microgravity two-phase flows using void fraction signals. *International Journal of Multiphase Flow*, 25(3):433 – 457, 1999. 2

[LSL$^+$08] Weifeng Li, Zhigang Sun, Haifeng Liu, Fuchen Wang, and Zunhong Yu. Experimental and numerical study on stagnation point offset of turbulent opposed jets. *Chemical Engineering Journal*, 138(1-3):283 – 294, 2008. 7, 75

[LZDG06] Dominique Legendre, Roberto Zenit, Claude Daniel, and Pascal Guiraud. A note on the modelling of the bouncing of spherical drops or solid spheres on a wall in viscous fluid. *Chemical Engineering Science*, 61(11):3543 – 3549, 2006. 9

[Mar03] P. Di Marco. Review of reduced gravity boiling heat transfer: European research. *J. Jpn. Soc. Microgravity Appl.*, 20(4):252 – 263, 2003. 3

[MCF98] J. McQuillen, C. Colin, and J. Fabre. Ground-based gas-liquid flow research in microgravity conditions: State of knowledge. *Space Forum*, 3:165 – 203, 1998. 2, 5

[MFK⁺10] Paul K. McConnaughey, Mark G. Femminineo, Syri J. Koelfgen, Roger A. Lepsch, Richard M. Ryan, and Steven A. Taylor. Launch propulsion systems roadmap (draft). *NASA Space Technology Roadmaps*, November 2010. 4

[MGM⁺03] P. Di Marco, W. Grassi, G. Memoli, T. Takamasa, A. Tomiyama, and S. Hosokawa. Influence of electric field on single gas-bubble growth and detachment in microgravity. *International Journal of Multiphase Flow*, 29(4):559 – 578, 2003. 3

[MJG93] Jessup J. M., Goodwin T. J., and Spaulding G. Prospects for use of microgravity-based bioreactors to study three-dimensional host-tumor interactions in human neoplasia. *J. Chem. Biochem*, 51:290–300, 1993. 5

[MJP⁺10] Mike Meyer, Les Johnson, Bryan Palaszewski, Dan Goebel, Harold White, and David Coote. In-space propulsion technology roadmap (draft). *NASA Space Technology Roadmaps*, November 2010. 4

[MKK05] K. Malysa, M. Krasowska, and M. Krzan. Influence of surface active substances on bubble motion and collision with various interfaces. *Advances in Colloid and Interface Science*, 114-115:205 – 225, 2005. Dedicated to the Memory of Dr Hans Joachim Schulze. 9

[MM01] John McQuillen and Brian Motil. Reduced gravity gas and liquid flows: simple data for complex problems. 2001. 6

[Moo65] D. W. Moore. The velocity of rise of distorted gas bubbles in a liquid of small viscosity. *Journal of Fluid Mechanics*, 23(04):749–766, 1965. 5, 8, 103, 105

[NZR08a] Iran E. Lima Neto, David Z. Zhu, and Nallamuthu Rajaratnam. Bubbly jets in stagnant water. *International Journal of Multiphase Flow*, 34:1130–1141, 2008. 6, 62, 67

[NZR08b] Iran E. Lima Neto, David Z. Zhu, and Nallamuthu Rajaratnam. Horizontal injection of gas–liquid mixtures in a water tank. *Journal of Hydraulic Engineering*, 134(12):1722–1731, 2008. 6, 26, 53, 57, 62, 67

[Orm97] Melissa Orme. Experiments on droplet collisions, bounce, coalescence and disruption. *Progress in Energy and Combustion Science*, 23(1):65 – 79, 1997. 5, 47

[OS06] Barnaby Osborne and Theodore Steinberg. An experimental investigation into liquid jetting modes and break-up mechanisms conducted in a new reduced gravity facility. *Microgravity Science and Technology*, 18:57–61, 2006. 7

[PB90] M.J. Prince and H.W. Blanch. Coalescence and breakup in air-sparged bubble columns. *AIChE Journal*, 36(10):1485–1499, 1990. 5, 61

[PFR06] M. Passandideh-Fard and E. Roohi. Coalescence collision of two droplets: Bubble entrapment and the effects of important parameters. *14th Annual (International) Iranian Mechanical Engineering Conference (ISME 2006)*, 2006. 47

[Pla73] Joseph Antoine Ferdinand Plateau. *Statique Expérimentale Et Théorique Des Liquides Soumis Aux Seules Forces Moléculaires*. Nabu Press (2010), 1873. 38

[PMBZ01] Ryszard Pohorecki, Wladyslaw Moniuk, Pawel Bielski, and Artur Zdrójkowski. Modelling of the coalescence-redispersion processes in bubble columns. *Chemical Engineering Science*, 56(21-22):6157 – 6164, 2001. 60, 61

[PSSM06] R. P. Pawlowski, A. G. Salinger, J. N. Shadid, and T. J. Mountziaris. Bifurcation and stability analysis of laminar isothermal counterflowing jets. *Journal of Fluid Mechanics*, 551(-1):117–139, 2006. 75

[Ram00] Doraiswami Ramkrishna. *Population Balances: Theory and Applications to Particulate Systems in Engineering*. Academic Press, 2000. 59

[Ray78] Lord Rayleigh. On the instability of jets. *Proceedings of the London Mathematical Society*, s1-10(1):4–13, 1878. 7, 38

[RJM06] Cláudio P. Ribeiro, Jr., and Dieter Mewes. On the effect of liquid temperature upon bubble coalescence. *Chemical Engineering Science*, 61(17):5704 – 5716, 2006. 9, 110

[Rod01] D. Rodrigue. Drag coefficient - reynolds number transition for gas bubbles rising steadily in viscous fluids. *The Canadian Journal of Chemical Engineering*, 79:119 – 123, 2001. 8

[SB05] R. Shankar Subramanian and R. Balasubramaniam. *The Motion of Bubbles and Drops in Reduced Gravity*. Cambridge University Press, 2005. 2

[Sch79] H. Schlichting. *Boundary Layer Theory. Seventh Edition*. McGraw-Hill Classic Textbook Reissue, New York, 1979. 6, 23, 58, 119

[SnGC10a] F. Suñol and R. González-Cinca. Opposed bubbly jets at different impact angles: Jet structure and bubble properties. *International Journal of Multiphase Flow*, 36(8):682 – 689, 2010. 54

[SnGC10b] F. Suñol and R. González-Cinca. Rise, bouncing and coalescence of bubbles impacting at a free surface. *Colloids and Surfaces A: Physicochemical and Engineering Aspects*, 365(1-3):36 – 42, 2010. 99

[SnGC11] F. Suñol and R. González-Cinca. Bubbly jet impingement in different liquids. *Microgravity Science and Technology*, 23:151–158, 2011. 65

[SnMPGC09] F. Suñol, O. Maldonado, R. Pino, and R. González-Cinca. Design of an experiment for the study of bubble jet interactions in microgravity. *Microgravity Science and Technology*, 21:95–99, 2009. 53, 54

[Spa80] D. B. Spalding. A mathematical modeling of fluid dynamics, heat transfer and mass transfer processes. Technical Report HTS/8011, Imperial College (London), 1980. 127

[SSSW08] Toshiyuki Sanada, Keiji Sugihara, Minori Shirota, and Masao Watanabe. Motion and drag of a single bubble in super-purified water. *Fluid Dynamics Research*, 40(7-8):534 – 545, 2008. Selected articles from the 1st International Colloquium on Dynamics, Physics and Chemistry of Bubbles and Gas-Liquid Boundaries - ICBB 2007. 8

[Str01] Johannes Straub. Boiling heat transfer and bubble dynamics in microgravity. volume 35 of *Advances in Heat Transfer*, pages 57 – 172. Elsevier, 2001. 3

[SWF05] Toshiyuki Sanada, Masao Watanabe, and Tohru Fukano. Effects of viscosity on coalescence of a bubble upon impact with a free surface. *Chemical Engineering Science*, 60(19):5372 – 5384, 2005. 8, 9, 110

[SZD06] Javad Saien, S. Alireza Ebrahimzadeh Zonouzian, and Asghar Molaei Dehkordi. Investigation of a two impinging-jets contacting device for liquid-liquid extraction processes. *Chemical Engineering Science*, 61(12):3942 – 3950, 2006. 7

[Tal07] M. A. R. Talaia. Terminal velocity of a bubble rise in a liquid column. *Proceedings of World Academy of Science, Engineering and Technology*, 22:264 – 268, 2007. 8

[TETO05] S. T. Thoroddsen, T. G. Etoh, K. Takehara, and N. Ootsuka. On the coalescence speed of bubbles. *Physics of Fluids*, 17(7):071703, 2005. 9

[TK97] Heng-Kwong Tsao and Donald L. Koch. Observations of high reynolds number bubbles interacting with a rigid wall. *Physics of Fluids*, 9(1):44–56, 1997. 9

[TKM95] H. Teng, C. M. Kinoshita, and S. M. Masutani. Prediction of droplet size from the breakup of cylindrical liquid jets. *International Journal of Multiphase Flow*, 21(1):129 – 136, 1995. 35, 36

[TSSA06] Koichi Tsujimoto, Toshihiko Shakouchi, Shuji Sasazaki, and Toshitake Ando. Direct numerical simulation of jet mixing control using combined jets. *JSME International Journal Series B Fluids and Thermal Engineering*, 49(4):966–973, 2006. 7, 56

[TUH04] H. Tsukiji, A. Umemura, and M. Hisida. Micro-gravity research on the atomization mechanism of near-critical mixing surface jet. *Proceedings of the Conference on Aerospace Propulsion*, 44:97–101, 2004. 7

[UD10] J. Uddin and S. P. Decent. Instability of non-newtonian liquid jets curved by gravity. *Mathematics in Industry*, 15(Part 2):597–602, 2010. 7

[UW02] Akira Umemura and Yuichiro Wakashima. Atomization regimes of a round liquid jet with near-critical mixing surface at high pressure. *Proceedings of the Combustion Institute*, 29(1):633 – 640, 2002. 7

[VA92] S. I. Voropayev and Ya. D. Afanasyev. Two-dimensional vortex-dipole interactions in a stratified fluid. *Journal of Fluid Mechanics*, 236(-1):665–689, 1992. 7, 80

[VAKF03] S. I. Voropayev, Y. D. Afanasyev, V. N. Korabel, and I. A. Filippov. On the frontal collision of two round jets in water. *Physics of Fluids*, 15(11):3429–3433, 2003. 7, 80

[Var95] J. Varely. Submerged gas-liquid jets: bubble size prediction. *Chemical Engineering Science*, 50:901–905, 1995. 6, 61, 62, 67

[WG02] Mingming Wu and Morteza Gharib. Experimental studies on the shape and path of small air bubbles rising in clean water. *Physics of Fluids*, 14(7):L49–L52, 2002. 8

[WHY+91] Philip Wood, Andrew Hrymak, Ronald Yeo, David Johnson, and Ashok Tyagi. Experimental and computational studies of the fluid mechanics in an opposed jet mixing head. *Physics of Fluids A: Fluid Dynamics*, 3(5):1362–1368, 1991. 7

[WO03] K. Willis and M. Orme. Binary droplet collisions in a vacuum environment: an experimental investigation of the role of viscosity. *Experiments in Fluids*, 34:28–41, 2003. 47

[YBCL07] Yosang Yoon, Fabio Baldessari, Hector D. Ceniceros, and L. Gary Leal. Coalescence of two equal-sized deformable drops in an axisymmetric flow. *Physics of Fluids*, 19(10):102102, 2007. 9

[YDS+99] B. Yoffe, G. J. Darlington, H. E. Soriano, B. Krishnan, D. Risin, N. R. Pellis, and V. I. Khaoustov. Cultures of human liver cells in simulated microgravity environment. *Advances in Space Research*, 24(6):829 – 836, 1999. Life Sciences: Microgravity Research II. 5

[YKB04] C.C.L. Yuan, M. Krstic, and T.R. Bewley. Active control of jet mixing. *Control Theory and Applications, IEE Proceedings* -, 151(6):763 – 772, 2004. 7

[ZKDM07] J. Zawala, M. Krasowska, T. Dabros, and K. Malysa. Influence of bubble kinetic energy on its bouncing during collisions with various interfaces. *The Canadian Journal of Chemical Engineering*, 85:669 – 678, 2007. 9

[ZL09] Roberto Zenit and Dominique Legendre. The coefficient of restitution for air bubbles colliding against solid walls in viscous liquids. *Physics of Fluids*, 21(8):083306, 2009. 9

[ZMH05] Hui Zhang, Issam Mudawar, and Mohammad M. Hasan. Flow boiling chf in microgravity. *International Journal of Heat and Mass Transfer*, 48(15):3107 – 3118, 2005. 3